DEPOSITION OF PARTICULATE FROM COAL-DERIVED SYNGAS ON GAS TURBINE BLADES NEAR FILM COOLING HOLES

by

Weiguo Ai

A dissertation submitted to the faculty of

Brigham Young University

in partial fulfillment of the requirements for the degree of

Doctor of Philosophy

Department of Chemical Engineering

Brigham Young University

December 2009

BRIGHAM YOUNG UNIVERSITY

GRADUATE COMMITTEE APPROVAL

of a dissertation submitted by

Weiguo Ai

This dissertation has been read by each member of the following graduate committee and by majority vote has been found to be satisfactory.

Date	Thomas H. Fletcher, Chair
Date	Jeffrey P. Bons
Date	Larry L. Baxter
Date	Kenneth A. Solen
Date	Randy S. Lewis

BRIGHAM YOUNG UNIVERSITY

As chair of the candidate's graduate committee, I have read the dissertation of Weiguo Ai in its final form and have found that (1) its format, citations, and bibliographical style are consistent and acceptable and fulfill university and department style requirements; (2) its illustrative materials including figures, tables, and charts are in place; and (3) the final manuscript is satisfactory to the graduate committee and is ready for submission to the university library.

Date

Thomas H. Fletcher
Chair, Graduate Committee

Accepted for the Department

Richard L. Rowley
Department Chair

Accepted for the College

Alan R. Parkinson
Dean, Ira A. Fulton College of Engineering
and Technology

ABSTRACT

DEPOSITION OF PARTICULATE FROM COAL-DERIVED SYNGAS ON GAS TURBINE BLADES NEAR FILM COOLING HOLES

Weiguo Ai

Department of Chemical Engineering

Doctor of Philosophy

Synfuel from gasification of coal, biomass, and/or petroleum coke is an alternative to natural gas in land-based industrial gas turbines. However, carryover fine particulate in the syngas may lead to a considerable amount of deposition on turbine blades, which reduces component life and system performance.

Deposition experiments on film-cooled turbine components were performed in an accelerated test facility to examine the nature of flyash deposits near film cooling holes. Experimental results indicate that deposition capture efficiency decreased with increased blowing ratio. Shaped holes exhibited more span-wise coverage than cylindrical holes and effectively reduced deposition. The TBC layer increased surface temperature, resulting in increased deposition. Coupons with close hole spacing exhibited a more uniform low temperature region downstream and less deposition. Capture efficiencies for small particles were lower than for large particles, especially at low blowing ratios. The

trench increased cooling effectiveness downstream, but did not reduce overall collection efficiency of particulates because the trench also acted as a particulate collector.

In the numerical computations using a CFD code (FLUENT), the standard k-ω turbulence model and RANS were employed to compute flow field and heat transfer. A Lagrangian particle method was utilized to predict the ash particulate transport. User-defined subroutines were developed to describe and predict particle deposition rates on the turbine blade surface. Small particles have a greater tendency to stick to the surface. As the surface temperature rose above the transition temperature, large particles dominated the excessive deposition due to the high delivery rate. Backside impingement of coolant improved the overall cooling effectiveness.

Experiments and CFD modeling results suggest that clean coolant dominated the initial deposition process by blowing off the particles and preventing particles from impacting on the surface. Initial deposits formed between coolant channels. Subsequent deposition occurred on top of initial deposits, due to increasing deposit surface temperature, which led to the formation of distinct ridges between coolant paths.

ACKNOWLEDGMENTS

I would take advantage of this opportunity to give my thanks to all the people who help me in completing this work. Firstly, I would like to extend my sincere gratitude to my thesis advisor, Thomas H. Fletcher, for pushing me to exceed my expectation and make me perform at the highest level possible. I would also like to thank Jeffery M. Bons and other members of my committee: Larry Baxter, Ken Solen and Randy Lewis, for their knowledge and expertise. Many thanks are given to Hong Lu and Andrew Mackrory for providing the help selflessly in measuring temperature, and all the undergraduate students for their hard work and great effort on this project: Robert Laycock, Spencer Harding, Nathan Murray, and Devin Rappleye. Special thanks go to Ken Forster, Kevin Cole, machinist of Precision Machine Lab, and Cory Arnell from Wilcox Associates, Inc., whose expertise and willingness to help greatly benefited the project. Financial support was provided by DOE/NETL and SCIES at Clemson University.

My wife Qian Pan deserves a place here for her constant love, support and dedication to taking care of our family during the challenging time. Her patience and understanding is truly unique and priceless. Special thanks to my daughter, Sinuo for the joy and power she gave to me. They are a blessing in my life and I am truly grateful.

TABLE OF CONTENTS

LIST OF TABLES

LIST OF FIGURES

NOMENCLATURE

Symbol	
A	Surface area [m^2]
CCD	charge-coupled device
CFD	computational fluid dynamics
C_D	drag coefficient
C_p	particle specific heat [kJ/ (kg·K)]
CMM	coordinate measurement machine
C_u	Cunningham correction factor
d	hole diameter
d_p	particle diameter
D	sample coupon diameter
DVC	dense vertically cracked
E	Young modulus [Pa]
F	force [N]
F_s	Saffman lift force [N]
F_{po}	sticking force [N]
h	convective heat transfer coefficient [W/m^2 K]
HVOF	high velocity oxygen fuel
IGCC	integrated gasification combined cycle
I_λ	radiation intensity at specific wavelength [$J/m^2 \cdot s$]
k	kinetic energy per unit mass [J/kg]
k	thermal conductivity [W/m.K]
k_r	local velocity gradient
k_s	constant=$3\pi/4$
K_c	composite Young's modulus
k_t	thermal conductivity [W/m·K]
ppmw	parts per million by weight
m	mass [kg]
$\mathcal{M}$	Mach number
M	blowing ratio = $\rho_c U_c / \rho_\infty U_\infty$
M1	cylindrical holes, metal coupon
M2	shaped holes, metal coupon
M3	s/d=3.375, metal coupon
M4	s/d=4.5, metal coupon
M5	metal coupon with cylindrical holes and a trench
M6	metal coupon with cylindrical holes and no trench
P_i	pixel count for color i
q	heat flux (W/m2),
TBC	cylindrical holes, TBC coupon

R	coupon radius
Re	Reynolds number
Ra	centerline-averaged roughness value [μm]
RGB	red/green/blue
Rt	vertical distance of highest peak and lowest valley [μm]
Rz	mean of vertical distance of peak and valley [μm]
RANS	Reynolds-averaged Navier-Stokes
s	hole spacing [mm]
S_i	the sensitivity constant converting incident light intensity to pixel count
slpm	standard liters per minute
t	camera exposure time [ms]
T	temperature [K]
TADF	turbine accelerated deposition facility
TBC	thermal barrier coating [K]
T_s	wall surface temperature [K]
T_{inf}	wall surface temperature at adiabatic condition [K]
Tu	turbulence intensity [%]
u	velocity [m/s]
UDF	user defined function
$u_{\tau c}$	critical wall shear velocity [m/s]
v_c	capture velocity [m/s]
W_A	a constant which depends upon the material properties
X	spanwise coordinate from left edge of coupon [mm]
Y	streamwise coordinate from film hole center [mm]
ε_b	sample emissivity
θ	inclined angle [degree]
α	impingement angle [degree]
η	centerline streamwise film cooling effectiveness
λ	wavelength [μm]
ε	turbulent dissipation rate [m^2/s^3]
ω	specific dissipation rate [s^{-1}]
ρ	density [kg/m^3]
η	overall film cooling effectiveness
ν	Poisson's ratio of surface material
β_λ	system spectral response
τ_γ	spectral transmittance of any additional optics
τ_w	the wall shear stress

Subscripts

aw	adiabatic wall
avg	average value
b	blackbody
c	property value of coolant for film cooling
ce	streamwise centerline

∞	property value at mainstream air conditions
i	refers to the ith element
j	refers to the jth element
o	initial
p	property value of particle
s	target surface
w	wall

1. Introduction

In land-based gas turbines, dust or airborne pollutants are heated up by high temperature gas and continue through to form deposition, erosion and corrosion on turbine components. With the high costs of the high-quality fuels such as natural gas, many operators of gas turbines are also turning their attention to the use of low-grade fuels. The most common alternate fuels are coal, biomass and oil residue-petcoke. These fuels are gasified to produce syngas, which is mainly composed of hydrogen and carbon monoxide. Such syngas is always contaminated with varying levels of impurities. Despite being filtered stringently, syngas introduced to a gas turbine is not completely clean. Syngas with entrained particulate burns in the combustion chamber, and the reaction products are introduced into the gas turbine.

The continuous demand for increased efficiency in gas turbine engines requires engine components to be designed for higher combustor exit temperatures. Thermal Barrier Coatings (TBC) have low thermal conductivity and allow elevated inlet gas turbine temperatures. The TBC may crack and or spall, exposing metal to the high-temperature gas directly. Current advanced gas turbine engines operate at turbine rotor inlet temperatures of 1200-1450 °C, which is hot enough to melt or severely weaken critical areas of the engine downstream of the combustor. Any entrained particles are heated to high temperatures in the gas turbine combustor and then impinge on turbine surfaces with inertial force. At the high mass flow rates in a typical large power utility, the impingement of even trace amounts of particulate can accumulate to significant quantities after a year of operation. Ash particulate deposition has several negative impacts on the gas turbine components. Deposition can clog vital coolant passages and alter blade contours, and can also accelerate material corrosion by bringing significant concentrations of corrosive elements in direct contact with the turbine component. Both erosion and deposition are known to increase levels of surface roughness, which may produce a corresponding increase of up to 50% in heat transfer and up to 300% in skin friction (Bons et al., 2001), thus aggravating the thermal load. Ghenaiet et al. (2005) reported a 6-10% loss in adiabatic efficiency for 6 hours of sand ingestion in an axial fan. Kim et al. (1993) documented the disastrous results of film cooling holes being plugged by massive amounts of simulated volcanic ash. This degradation reduces component life and increases the risk of run-time failure by changing the balance of high-speed rotating component. Furthermore, deposition deteriorates the performance and efficiency of the gas turbine and decreases the overall output and service time of the whole system.

Surface degradation is a function of the specific turbine-operating environment. Two of the important determining factors are (1) the particle temperature (assumed to be near the gas temperature), and (2) the turbine surface temperature. The particle temperature determines the physical state of the particles (e.g. solid, molten or vapor). The physical state in turn influences whether the particles rebound from the surface or tend to deposit. The temperature threshold range for deposition is between 980 °C and 1150 °C (Krishnan et al., 2003). The turbine inlet temperature of H-class gas turbine engines is higher than this threshold value. Wenglarz (1992) reported a temperature threshold of about 1100 °C where a large fraction of the particulate is molten and therefore sticks to the turbine surfaces more readily. Wenglarz's experiment showed that the blade life may be cut in half if the blade metal temperature prediction is off by only 30 °C.

Cooling is used to maintain the turbine blade surface temperature well below the inlet gas temperature for most modern gas turbines. In general, cooling schemes consist of internal cooling and external film cooling. Convective cooling of the internal surface of the engine parts is the simplest method of reducing wall temperatures. Impingement cooling is another method of obtaining high heat transfer rates on the internal side of the engine parts. Coolant in the form of high-momentum jets hits the internal surface perpendicularly and increases heat transfer coefficients. Another effective way to lower wall temperature is the generation of a coolant film on the hot surface, which considerably reduces the heat transfer between the hot gas and turbine blades. To produce cooling films, the coolant is blown through inclined slots or through differing numbers of inclined holes. The combination of internal convective cooling and external film cooling is the most effective as well as the safest way to prevent engine components from failure through excessive heat loads.

Few studies have been conducted on deposit formations in gas turbines with cooling schemes. Research is needed on the combined effects of particle deposition on gas turbine blades and film cooling (with associated internal cooling). The primary factors affecting the extent of deposition on turbine blades include gas temperature, turbine surface temperature, particle chemical composition and physical properties, fuel type, film hole configuration, blowing ratio, density ratio, and momentum ratio. The research documented here investigates the following aspects of particulate deposition: film hole configuration, blowing ratio, hole spacing, trench effects, and the effect of thermal barrier coating. Experiments were performed to study deposit patterning under differing test conditions. Associated CFD modeling was also performed, which quantifies the local heat transfer coefficient and cooling effectiveness near the hole exit.

This document presents a literature review is in Chapter 2 of, followed by an outline of the objectives in Chapter 3. The methodology and approach to accomplishing the objectives are presented in the Chapter 4. The results and discussion are shown in the Chapter 5. The numerical simulation model is presented in Chapter 6. Conclusions and recommendations for future work appear at the end of the thesis.

2. Literature Review

This research involves gas turbine film cooling technology and fuel ash particle deposition in the region mear the film cooling holes on gas turbine blades. Therefore, the following literature review is divided into two sections: (1) particle deposition and (2) film cooling technology.

2.1 Ash Particle Deposition

Many laboratory testing and field evaluations have been performed to study turbine hot section deterioration from airborne contaminants and fuel impurities. A better understanding of the factors affecting deposition on turbine surfaces allows for a more accurate estimate of the impact on the efficiency and survivability of turbine blades.

2.1.1 Gas Temperature and Turbine Surface Temperature

As gas turbine engine technology has evolved from F-class to G-class , and now to H-class, turbine inlet temperatures have increased from 1300°C to 1500°C and thermal efficiency has increased from 55% to nearly 60% for H-class turbines (Suao and Aoki, 2000). With the proposed large-scale introduction of low-grade fuels such as coal and biomass in H-type turbines, past turbine operating experience has shown that deposition will increase dramatically at higher temperatures, which will increase corrosion of hot section vanes and blades, which will decrease efficiency and increase maintenance requirements.

Previous turbine tests with coal-derived fuels by Wenglarz and Fox (1990a) showed a dramatic increase in deposition rate as the gas temperature is raised above ~1100°C. In a similar study, Crosby et al. (2007) noted a dramatic rise in micron-sized coal particulate deposition for gas temperatures above 960°C using an accelerated deposition facility. These threshold temperatures correspond to the particulate softening or sintering temperature, above which some particles impacting on the surface begin to melt and result in adhesion with the surface upon impact.

Since first-stage turbine components operate at the highest temperatures, deposition usually takes place on the first-stage vanes or stators. The deposition behavior of two kinds of volcanic materials was investigated by Kim et al. (1993) on the two hot sections of a test system. They reported that the temperature of the surface onto which the particles impact must be above a certain threshold temperature if deposition is to occur. Increasing the vane metal temperature increased the amount of deposits significantly. Surface temperature is one of the major factors determining whether a particular dust blend is deposited on blade surfaces.

Wenglarz et al. (1990a) studied the effect of ash from coal-water slurries on the component degradation of combustion turbines. Their results indicated that deposition at a surface temperature of 1100 °C was about 2.5 times greater than at 900 °C. Once an initial thin deposit was formed, deposition rate was accelerated on subsequent deposits. Furthermore, higher gas temperatures in these coal-water slurry tests resulted in an extremely aggressive and unusual type of attack on a corrosion resistant coating

(Wenglarz and Fox, 1990a). Tests with a commercially washed and treated residual oil turbine fuel (Whitlow et al., 1982) showed 30 times higher deposition rates on specimens exposed to temperatures of 1260 °C compared to 1038 °C. Heavy deposits were also formed at a gas temperature of 1260 °C in a 100-hour test of a coal-derived liquid fuel that produced 2 to 3 ppmw (particles per million by weight) particulate loading in the gas stream (Mulik et al., 1985).

2.1.2 Physical Characteristics of Deposit

Deposit location is strongly influenced by particle size, shape, and density. Finer, lighter particles tend to follow the flow more readily, while coarser, heavier particles do not follow the flow quite as well. Larger particles also have a higher thermal mass and do not melt as easily as smaller particles. At the high velocities and temperatures in a gas turbine, inertial impaction dominates other deposition mechanisms. A large fraction of particles larger than a few microns is delivered to the metal surface, resulting in high captured fractions and rapidly built-up deposits. Meanwhile, smaller particles are delivered at lower rates and dominated by mechanisms such as eddy impaction, turbulent diffusion, and thermophoresis. Kim et al. (1993) showed that the locations where deposition occurred appeared to be dependent on the acceleration field within the vanes near the deposit location. The regions of rapid flow deceleration near the surface were the first places for deposits to form. Particles that were unable to follow the flow path will tend to be concentrated and deposited on the vane surfaces closer to the outer shroud.

Testing on a GE J85-13 jet engine by Syverud et al (2007) suggested that salt deposits were mainly found along the leading edge of the first four stages and on the pressure side of the stator vanes along the hub. The heaviest deposits were found along the first-stage annulus, at the leading edge of the second-edge stator vanes, and along the hub at the pressure side of the second and third-stage blades and vanes. Significantly fewer deposits were observed on the rotor blades compared to the stator vanes. Similar phenomena were observed by the work of Ragland et al. (1995). The test was performed in an Allision model 250-C20B gas turbine, which was coupled to an L-shaped, refractory-lined, downdraft combustor. The deposits were found to be heavier on the vanes than on the rotors. The deposits on the leading edge of the second and third stage vanes were heaviest. The contribution of particle size on deposits was studied by Crosby et al. (2007) in a laboratory-scale accelerated deposition facility. The tests were performed with no cooling air, and the interior passage of the cooling fixture was insulated with blanket insulation material. The capture efficiency defined as mass percentage of particles collected by samples in these tests increased more than 50% as particle size was increased from 3 μm to 16 μm.

2.1.3 Chemical Characteristics of Deposit

Deposit composition is mainly affected by fuel type and temperature. In general, the relative concentration of elements detected in the deposit is similar to those detected in the ash. Bons et al. (2007) showed that the main components in the ash from coal, biomass and petcoke were Si, Al, Ca , Fe , K and Na. Calcium and Magnesium concentrations in sawdust are at a higher level than in coal and petcoke. Straw ash composition is similar to coal and petcoke composition except that for a higher level of potassium. Petcoke contains high iron concentration. Coal ash and petcoke ash contain much higher concentrations of silica and alumina than sawdust.

Comparatively, biomass is usually enriched in potassium and calcium. In Ragland's study (1995) on a wood-fired gas turbine, calcium was the most prevalent inorganic compound and was present in the turbine deposits as calcium oxide and calcium hydroxide. Potassium was the second most prevalent inorganic compound and was identified in the form of potassium sulfate. The elemental analysis at the time of the first turbine overhaul showed that the deposit consisted primarily of potassium, calcium, magnesium, and sulfur. Deposits on the first-stage vanes were richer in alkali metals (potassium and sodium) and sulfur, whereas those in the downstream stages showed decreasing concentrations of both potassium and sodium and increasing proportions of calcium and magnesium. During the second turbine overhaul, the deposits on the upstream stages were richer in calcium compared to those in the downstream stages, and the relative amounts of potassium, sodium, and sulfur were higher in the deposits on stationary vanes compared to those on rotating blades. Bons and coworkers (2007) studied the impact of sawdust ash on turbine blade samples at 1183 °C. The deposits exhibited a high calcium concentration, which coincided with the concentration of Ca in the initial ash. Deposits also showed significant increases in the concentration of Si (relative to the ash) at the expense of calcium, potassium and magnesium.

In the study of Wenglarz et al. (1990b) on coal-water slurry combustion under gas turbine conditions, deposits showed very high sodium levels on some specimens compared to levels in the fuel ash. The deposit chemistries fell into two categories based on the Na level. At low-temperature (980°C), observed Na concentrations were 2.5 times higher in the deposit than in the fuel ash. Silicon and aluminum percentages in the deposits were substantially lower (usually a factor of 2 or more) than in the fuel ash. In addition, the deposition rates of ash were relatively low. At high temperatures (1100°C) the Na, Si, Al percentages in the deposits were comparable to the percentages in the fuel ash. The deposition rate of ash was higher at 1100°C than at 980°C.

2.1.4 Thermal Barrier Coating

Thermal barrier coatings (TBCs) consist of a ceramic insulating layer on the surface of a turbine blade. TBCs are a necessity in modern high-temprature gas turbines and have been studied for several decades. Continuous development and advancement in TBCs to improve their performance are required to enable further increases in turbine inlet temperature, reduction in air cooling requirements and improvements in component durability. Kumar et al. (2002) developed a numerical heat transfer model to predict convection and radiation to the blade with and without a TBC. The simulation showed that the TBC reduced metal surface temperature and decreased the heat flow rate from gas to coolant by 20%. These effects were more pronounced at higher gas inlet temperature.

Unfortunately, TBCs are susceptible to various life-limiting issues associated with their operating environment including erosion, corrosion and deposition. Much work has been performed by BYU workers to study deposition on coupons with a thermal barrier coating (TBC). Wammack et al. (2006) simulated an operational cycle of a real in-service gas turbine by running four experiments in a row on the same coupon. After every experiment, the coupon was removed from its fixture and was scanned by a profilometer. A convective heat transfer coefficient was determined from a scaled-up surface that was milled and placed in a wind tunnel. Their study showed that the surface roughness conditions have a significant effect on deposit growth. The TBC coupon surface was rougher and consisted of a relatively porous ceramic material, allowing deposits to more readily stick to the surface. Thermal cycling combined with particle deposition caused extensive TBC spallation. Deposit penetration into the TBC is a significant contributor to spallation. At the conditions investigated, the deposit produced a plateau in the measured heat transfer coefficient, being consistent with the surface roughness size and shape. The increased surface roughness resulted in elevated levels of convective heat transfer.

In the study of Crosby et al. (2007), three series of tests were conducted to study the effects of (1) particle size, (2) gas exit temperature, and (3) metal temperature on deposition on TBC coupons. Results indicated that particles penetrated into cracks in the TBC, causing spallation along the leading edge of the coupon. The spallation behavior increased with ash particle size. The same TBC flaking behavior was observed for the test series where gas temperature varied, but very little flaking was noticed at lower temperatures. The study also suggested that the introduction of internal coolant produces a thinner deposit layer, which was much more tenacious than that generated in the conditions without coolant.

2.1.5 Modeling Particle Deposition

Models of particle transport and deposition can be developed either by the Eulerian approach or the Langrangian approach. The Eulerian approach is based on the assumption that two continuous fields are present, and transport equations are solved simultaneously for both phases. A uniform particle concentration is usually assumed at the outer edge of the boundary layer. Therefore, this model is suitable for very small particles. The first major deposition models were developed by Friedlander et al. (1957) and Davies et al. (1966). In this model, particles were transported by turbulent diffusion from the bulk flow toward the surface within one particle stop distance, characterized by a particle relaxation time and wall-ward velocity. Particles were assumed to deviate from the local turbulent fluid motion, arriving at the surface by their inertia. Deposition was usually assumed to be entirely limited by this final transport, implying that the deposition rate should only depend upon the particle relaxation time when normalized to wall variables. Liu et al. (1974) proposed a new expression for particle diffusivity, containing an additional term to account for enhanced deposition by inertia. The local fluid velocity was used as the particle free-flight velocity at the stop distance, and the particle concentration there was estimated by assuming that the concentration profile was identical to the streamwise velocity profile. The model yielded reasonable agreement with deposition rate measurements for intermediate particle relaxation times, but poor agreement at high values.

In the Lagrangian approach, a number of particle trajectories are simulated by solving the equations of continuity, momentum, and energy for individual representative particles. Multiple forces on the particle are considered in the particle equation of motion, making this approach applicable to all particle sizes. The Lagrangian approach provides a more detailed and realistic model of particle transport because the instantaneous particle equation of motion is solved for each representative particle moving through the field of random fluid eddies. Moreover, this approach provides detailed information on particle collisions at the surface that are required for sticking studies. Kallio and Reeks (1989) presented a Lagrangian approach to model particles transported in turbulent duct flows. They solved the equation of motion for particles with normalized relaxation times ranging from 0.3 to 1000. Their results showed very good agreement with the experimental data of Liu and Agarwal (1974) over a wide range of particle sizes.

GreenField and Quarini (1997) considered the drag force as the principal force acting on particles. They presented the effect of turbulence on the particles by using the eddy lifetime model. The turbulence was modeled as a series of random eddies which had a lifetime and associated random fluctuating velocities.

2.2 Film Cooling

Film cooling is one of the major technologies that allow gas turbines to operate with extremely high temperatures and still maintain reasonable part lifetimes. Cooling air is bled through the holes of blades to form a protective layer of cooling between the hot gases and the blade wall surfaces. Extensive research into the many aspects of film cooling has been conducted in the past few years. Publications related to film cooling are numerous and mainly deal with topics such as fluid dynamics in film holes, hole shape, hole orientation, hole spacing, density ratio (coolant density divided by mainstream density), blowing ratio, momentum flux ratio, effects of mainstream turbulence intensity, and surface curvature and roughness (Bunker, 2005; Crosby et al., 2007).

In film cooling, the adiabatic film effectiveness and the heat transfer coefficient on the surface are two significant parameters used in evaluating local heat transfer. The film cooling effectiveness describes the cooling potential of the injected film without any heat flux into the wall. The heat transfer coefficient considers the influence of the coolant injection on the heat transfer process due to the modified fluid dynamics. Film cooling technology is complex. The parameters affecting heat transfer include blowing ratio, momentum flux ratio, velocity ratio, density ratio, slot height, and free stream Mach number. These parameters and their relative magnitudes and interactions determine the initial film effectiveness level at the injection point and also the rate of decay of cooling effectiveness downstream (Bunker, 2005).

2.2.1 Geometry

Film hole studies can be classified into one of four hole geometries as depicted in Figure 2.1. Geometry A is a classic shaped film hole that includes both fan-shaped and laidback configurations. Geometry B contains only lateral exit expansion, while geometry C contains only laidback expansion. Geometry D includes the compound angle and shaped expansion.

Hole geometry substantially affects the adiabatic effectiveness. Film-cooling holes with a diffuser shaped expansion at the exit portion of the holes are believed to improve the film-cooling performance on a gas turbine blade. The theory was presented by recent experimental studies. Goldstein et al. (1974) showed that overall improvements in adiabatic effectiveness were found for the flat-plate film cooling with laterally expanded holes. Makki and Jakubowsi (1986) presented the same improvement for forward-expanded holes. Haller and Camus (1983) performed aerodynamic loss measurements on a two-dimensional transonic cascade. Holes with a span-wise angle of 25 deg were found to offer significant improvements in film-cooling effectiveness without any additional loss penalty. Schmidt et al (1994) and Sen et al (1994) compared a cylindrical hole to a forward-expanded hole. Although the spatially averaged effectiveness for the cylindrical and forward-expanded jet was the same, a larger lateral spreading was found with the forward-expanded jet. The performance of holes with A, B, C geometries were investigated by Gritsch et al (1998) . Both expanded holes showed significantly higher adiabatic wall effectiveness and lower heat transfer coefficients than the cylindrical hole for the surface downstream of the ejection location, particularly at high blowing ratios. The laidback fan-shaped hole provided a higher laterally-averaged film-cooling effectiveness and lower laterally-averaged heat transfer coefficients than the fan-shaped hole. All hole designs resulted in improved thermal protection for the surface downstream of the hole location.

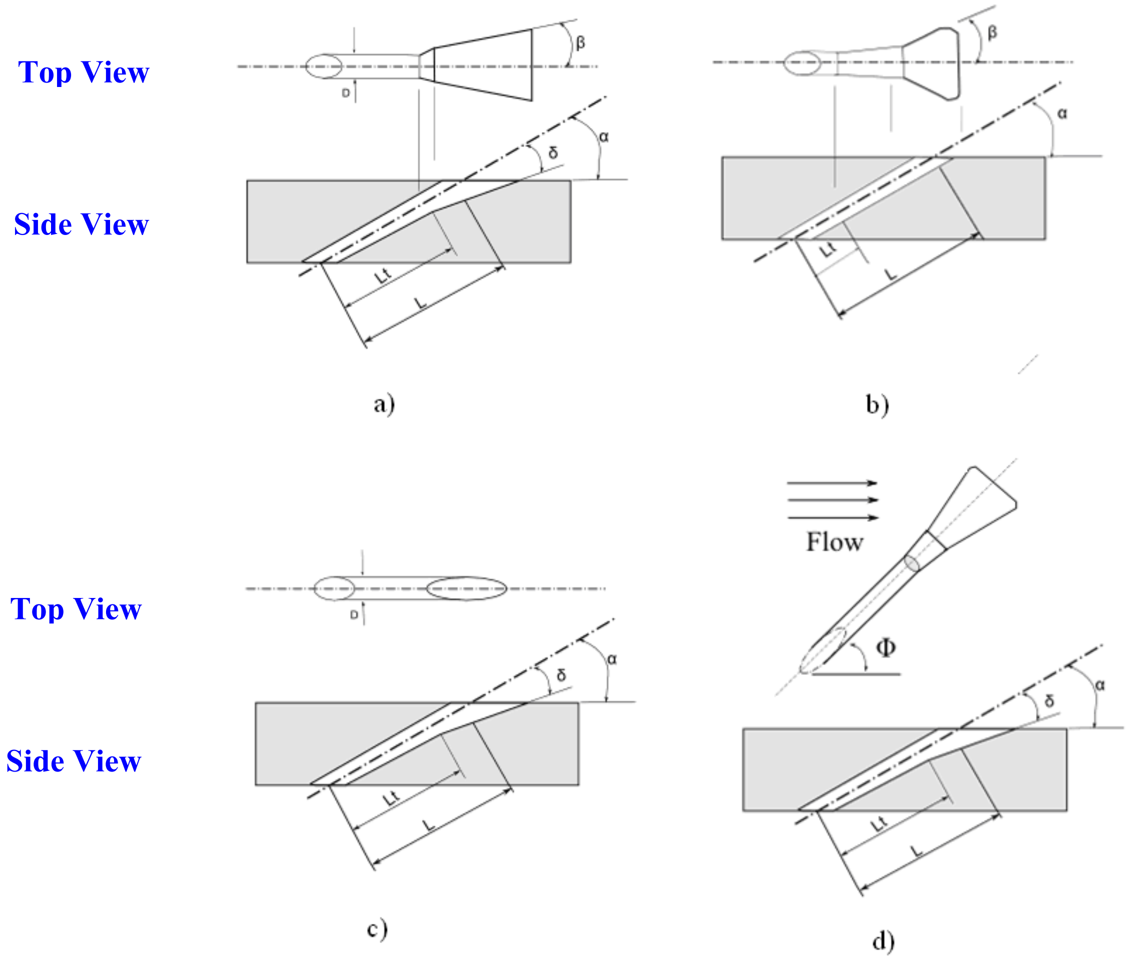

Figure 2.1 Defined geometries for four types of shaped film holes : a) fan-shaped and laidback expansion; b) lateral exit expansion; c) laidback expansion; and d) compound angle and shaped expansion

The determination of the heat transfer coefficient with film-cooling in the section close to the hole is essential for predicting the overall thermal load on the blade. Several studies have been conducted concerning the effect of hole geometry on heat transfer. Sen et al. (1994) and Schmidt et al. (1994) found that compound angle injection (Geometry D) enhanced the heat transfer rates substantially due to an increased jet-crossflow interaction. Therefore, the overall performance with the combined effects of reducing blade temperature and heat transfer was lower for compound angle holes. These findings were in agreement with the studies of Ekkad et al. (1997). Makki and Jakubowski (1986) studied the benefits of trapezoidal shaped holes as compared to standard cylindrical holes. They reported the heat transfer coefficient of the shaped holes to be up to 20% lower in the vicinity of the hole, particularly at low and medium blowing ratios.

2.2.2 Blowing Ratio

Blowing ratio M is defined as ratio of coolant mass flux to mainstream mass flux ($M = \rho_c u_c / \rho_\infty u_\infty$). The blowing ratio is one of the most significant parameters affecting film cooling effectiveness and heat transfer. Gritsch et al.(1997) examined blowing ratios from 0.25 to 1.75 and found that the fan-shaped type hole exhibited optimal effectiveness for blowing ratios of about 1-1.2. The shaped hole showed little sensitivity to blowing ratio changes from 0.5 to 2.

Zhu et al.(2004) tested dustpan-shaped holes, fan-shaped holes, and round holes using a large-scale low-speed loop wind tunnel. At x/d=1, the average heat transfer coefficient ratio increased rapidly with the blowing ratio. Further downstream, the average heat transfer coefficient ratio of dustpan-shaped holes increased faster with blowing ratio than that of round and fan-shaped holes.

2.2.3 Roughness

The effect of surface roughness (like that created by deposition) on film cooling effectiveness has been reported in numerous studies (Goldstein et al., 1985; Barlow and Kim, 1995; Schmidt et al., 1996; Rutledge et al., 2005). At low blowing ratios, roughness reduces the film effectiveness, while at high blowing ratios, roughness can actually improve film effectiveness by limiting jet lift-off from the surface. Surface roughness degrades performance at low blowing ratios through two mechanisms. First, rough surfaces produce thicker boundary layers and thus lower near-wall velocities compared to smooth surfaces. This produces a higher "effective" blowing ratio for the roughness-thickened boundary layer, which can lead to jet lift-off at lower values of M. Second, roughness generates significant near wall turbulence that dissipates coolant more rapidly. Cardwell et al. (2005) measured a 30% decrease in end-wall film cooling effectiveness due to a combination of these two roughness-induced effects using a vane cascade. Film cooling effectiveness alone does not capture the full effect of roughness on film cooling since roughness also enhances surface heat transfer. When the combined effects of film cooling effectiveness and heat transfer are properly accounted for, the result can be a 30-70% increase in surface heat flux with roughness (compared to a smooth surface) (Rutledge et al., 2005). Recent attention has also been given to the damaging effect of flowpath obstructions on film effectiveness, either from deposits (Demling and Bogard, 2006; Sundaram and Thole, 2006) or TBC residual (Bunker, 2000). Deposit obstructions located directly upstream of film holes resulted in a significant reduction in adiabatic effectiveness while a slight improvement in adiabatic effectiveness was noted if deposits were positioned downstream. Deposit blockage in the hole itself had a disastrous effect in all cases.

2.2.4 Hole Spacing

Many studies in the past decade have been conducted on effects of hole spacing on film cooling effectiveness and heat transfer.

Brown.et al. (1979) measured film-cooling effectiveness resulting from coolant injection through a single hole and rows of holes with three pitch-to-diameter ratios. Pitch is the distance between the centers of two adjacent cooling holes in the spanwise direction. Their results indicated that the optimum blowing ratio for maximum film cooling effectiveness at the investigated pitch-to-diameter ratio was about 0.5. The greatest cooling effectiveness was in the region close to the holes for the smallest pitch-to -diameter ratio. Mehendale et al. (1990) compared the effect of film hole spacing on film effectiveness and heat transfer coefficient downstream of the film holes to determine which film hole geometry provided the lower heat load. Their study showed that the best cooling effectiveness happened at a blowing ratio near 0.5. For large hole spacing, the optimum blowing ratio was slightly larger than 0.5, while the optimum for small hole spacing was lower than 0.5. In the leading edge region, coolant injection from film cooling holes with large hole spacing produced significantly lower heat transfer coefficients than the holes with small hole spacing, due to the physical spanwise distance between successive holes, resulting in less flow interaction and less cooling coverage.

Baldauf et al. (2002) studied the effect of hole spacing on cooling effectiveness with various blowing ratios. They reported that for shallow ejection angles, the laterally-averaged effectiveness with small hole spacing was well above the values achieved with large hole spacing. For narrow hole spacing, the maximum effectiveness peak downstream occurred at very short downstream distances due to interaction with adjacent jets. This maximum peak at low blowing ratio was distinct and decayed gradually in the stream-wise direction. At high blowing ratio, the peak remained over a large downstream distance. For a larger hole spacing, the optimum overall effectiveness occurred at a specific blowing ratio. Further increases in the blowing ratio causes a monotonic decrease in the effectiveness due to boundary layer lift-off. Adjacent jets did not influence the laterally averaged effectiveness values.

Waye et al. (2007) made the same conclusion that the small spacing generated a higher effectiveness than the large one. In the study of three hole patterns, Lin (2006) suggested that small pitch is better for spanwise cooling uniformity and is desirable for a pattern with more rows of holes available. Baldauf et al. (2001) also reported that the early contact of the vortices with the surface was obstructed for small pitch ratio, resulting in a low heat transfer area close to holes. The traces for large pitch ratio were not obstructed by adjacent jet interaction. Heat transfer increased gradually near the coolant fluid ejection.

Yuen et al. (2005) studied the heat transfer characteristics of rows of round cooling holes. Their measurement suggested that the spanwise uniformity and coverage in effectiveness were improved with the smaller pitch, particularly for the intermediate and far downstream regions. The heat transfer for a hole with a small pitch-diameter ratio was higher than that for a larger one.

2.2.5 Trench Configuration

In the study of cooling-hole geometry, shaped holes were found to provide dramatically-improved cooling effectiveness. However, the complex geometry of this configuration leads to increased machining costs. Bunker (2002) suggested a configuration with the cooling holes embedded in a slot, and studied two slots with different width to hole diameter ratios. Results were compared with data from the same cooling-hole configuration without the trench, indicating that a narrow width to diameter ratio was desirable. The configuration with cooling holes in the slot showed little or no sensitivity of film cooling effectiveness to blowing ratio over the range from M = 1.0 to 4. No film blow-off was observed at high blowing ratios, implying that the coolant injected from the cooling holes could impinge the front wall of the slot and spread out in the slot, resulting in contact with hot gas in a 2-D rather than a 3-D structure. The trench configuration was shown to provide elevated film cooling performance.

The geometry of the transverse slot greatly affects the cooling performance downstream of injection. Lu et al. (2005) used a transient infrared thermography technique to study four different slot configurations in addition to a baseline configuration with no trench. The slot-to-diameter ratio was 3.5 and the slot depth to hole diameter ratio was 0.4. The experiments showed that the configurations of a downstream slot and a sloped downstream slot outperformed the other geometries with regards to film cooling coverage and heat transfer.

Nine trench configurations were compared experimentally by Waye et al. (2007) to examine the effects of a transverse trench on the film cooling effectiveness of axial holes. They found that a rectangular wall right downstream of the trailing edge of the cooling holes can increase the cooling effectiveness immediately. The narrow full trench configuration provided the best adiabatic effectiveness performance whether the blowing ratio was low or high, due to the fact that coolant was contained in the trench and hence allowed minimal mainstream hot gas entrainment. The trench suppressed the coolant jet separation at increased blowing ratios. The wide trench configuration performed worse at low blowing ratios, but yielded better cooling than the baseline hole configuration at high blowing ratios.

Lu et al. (2007b) investigated three different cratered hole geometries by comparing film effectiveness and heat transfer coefficients of a baseline case, a trench case, and a shaped hole case. Their study indicated that the cratered holes demonstrated better film cooling performance than the baseline case, and outperformed the trench configuration at low blowing ratios, while the trench case performed better than the catered hole case at high blowing ratios. Overall, the cratered holes do not perform as well as the trench. A parametric study on the effects of trench width and depth in a 2-D trench slot was performed by Lu et al. (2007a) to obtain the optimum trench width and depth. The interaction of the coolant jets and the mainstream flow were studied quantitatively by examining changes in the heat transfer coefficient and film effectiveness. A deeper trench minimized mainstream gas interaction at the upstream edge of the trench and enhanced the lateral spreading of coolant, resulting in lower lift-off of coolant over the surface. The trench configuration with a width of 3d and depth of 0.75d performed best in these studies.

More recently, Dorrington and Bogard (2007) investigated many different shallow trench or crater configurations and determined that a depth of 0.75d was critical to dramatically improve film effectiveness performance. The other finding was that a sloped lip of the trench downstream of the edge of the coolant holes, spread over a distance equal to or more than the trench depth, significantly reduced performance. A narrow trench with close pitch exhibited better performance than a trench with large pitch due to the interaction between coolant jets within the trench. The study conducted by Lu and

Bunker (2008) on the shape of the trench edge downstream of film holes showed that edge angling had a minimal effect on the overall cooling effectiveness. The experiments by Somawardhana and Bogard (2007) on an airfoil showed that the transverse trench configuration performed better than the traditional cylindrical holes, even almost eliminating the degrading effects from surface roughness at high blowing ratios.

Computational simulations performed by Harrison et al. (2007) for a trench configuration were consistent with experimental measurements. They concluded that CFD simulations can be used to screen various film cooling configurations and indentify promising trench geometries. Renze et al. (2008) used the Large-Eddy Simulation (LES) method to determine the main flow characteristics of film cooling with a shallow cavity. The flow field was categorized into five zones on the basis of the interaction of coolant jets with a jet in cross flow. It was reported that a shallow cavity can lead to stronger mixing with the mainstream at a low blowing ratio.

There are other factors influencing cooling effectiveness, such as stream turbulence intensity and surface curvature. The study of Schmidt and Bogard (1996) indicated a significantly decreased adiabatic effectiveness for high turbulence levels at low to moderate momentum flux ratios, and an increase of effectiveness at large momentum flux ratio. Saumweber et al. (2002) reported that coolant stream from shaped holes at low turbulence levels did not show any inclination to detach, even at the highest blowing ratio. But the coolant stream with high turbulence intensity results in a stronger decay of cooling effectiveness. Drost et al. (1997) revealed a maximum effectiveness of 0.3 on the suction side, with slightly higher values for the double row, but only low effectiveness on the pressure side. Schwarz et al. (1991) found that cross-stream pressure gradients tended to move film cooling jets onto a convex surface and away from a concave surface.

2.2.6 Conjugate Heat Transfer

Conjugate heat transfer involves the study of both the convective heat transfer between solid and fluid and the coupled conductive heat transfer in the solid. In turbomachinery applications, the heat conduction inside the solid cannot be neglected. It is therefore necessary to consider the flow field together with temperature distributions within the metal. Bohn et al. (2003) studied the calculations of a film-cooled duct wall with the boundary condition of an adiabatic and a conjugate heat transfer condition for various configurations of film-holes. The conjugate heat transfer was found to influence the velocity field within the cooling film. The magnitude of the peak secondary flow velocities was much higher for the adiabatic case than with the conjugate heat transfer, which degraded the performance of the cooling.

Silieti et al. (2005) predicted film cooling effectiveness using three different turbulence models: the realizable k-ε model (RKE); the SST k-ω model; and the v2-f model. They predicted that film cooling effectiveness using the conjugate model is in better agreement with the experimental data compared to the adiabatic model. Andreini et al. (2005) carried out several calculations to infer the trends of adiabatic and conjugate heat transfer performance in terms of heat transfer coefficient, overall and adiabatic effectiveness. They concluded that the reduction of metal temperature upstream of each cooling hole increased as the blowing rate increased.

Na et al. (2007) performed computations to study the conjugate heat transfer for a flat plate with and without TBC. They found that the surface temperature increased slightly when the thermal conductivity was reduced to a certain value to mimic a thermal barrier coating.

2.2.7 Modeling Film Cooling

A systematic computational methodology was developed by Walters et al. (1996) to calculate the adiabatic effectiveness of film cooling. Four critical issues to the success of a computational prediction were proposed: (i) computational model; (ii) geometry representation and grid generation; (iii) discretization scheme; and (iv) turbulence modeling. Their computational results tended to show that the use of unstructured grids over-predicted centerline effectiveness values and under-predicted the lateral average value, but showed more consistent agreement with experimental data than with a structured grid simulation. Hoda et al. (2000) investigated the performance of several existing turbulence models on the prediction of film coolant jets in cross flow. Computational results were compared with measurements reported by Ajersch et al. (1995) to examine whether the models accurately predicted the dominant features of the flow field. The use of the k-ω model yielded an improved prediction of near-wall structures. Jia et al. (2005) performed a systematic evaluation of the current computational model to study the film cooling fluid injection from slots or holes into a cross flow. They concluded that the shear stress transport k-ω model provided a more faithful prediction of the mean and rms velocity distribution. The 30° jet provided the highest film-cooling effectiveness. Harrison and Bogard (2008) found that the standard k-ω (SKW) model best predicted laterally-averaged adiabatic effectiveness, and that the realizable k-ε model was best along the centerline. The Reynolds stress model yielded the best predicted heat transfer coefficients.

Numerical simulations have been made by many researchers to study the heat transfer with film cooling. Walters et al. (2000) applied a previously documented systematic computational methodology to a three-dimension film-cooling flow-field with a series of varying geometrical hole configurations. In this methodology, a novel vorticity-based approach was included in the analysis of the flow physics. A sub-region technique controlled the node placement within the domain. The combination of the standard k-ε model with wall functions, which is currently the standard approach in complex problems, was applied in the model. The results of simulating stream-wise injection with cylindrical holes indicated that the counter-rotating secondary flow structure downstream of the jet exit was the most significant mechanism affecting the film-cooling performance in stream-wise injection. Film-cooling performance for a stream-wise injection case may be significantly improved by controlling the strength of the counter-rotating vortex pair.

Five distinct film cooling configurations were modeled by Hyams et al.(2000) to study the physics of the film cooling process for shaped, streamwise-injected, and inclined jets. The results indicated that film hole shaping could significantly affect the distribution of the exit-plane variables, which determine downstream film cooling performance. The laterally-diffused film hole provided the best coverage and highest effectiveness. The forward-diffused film hole performed well along the centerline, but did not spread laterally. The cylindrical and inlet-shaped film holes performed poorly.

Furthermore, Brittingham et al. (2000) simulated film cooling with shaped holes. Conclusions were made that the superposition of effects for compound-angle cylindrical holes and streamwise shaped holes did not necessarily apply to the compound-angle shaped hole. The flow in the film hole prior to shaping was mostly unaffected by the compound angle. The vorticity field at the jet exit was due primarily to film hole boundary layers and the jet/crossflow shear layer. This field determined the existence, strength, direction of rotation, and location of secondary vertical structures, and was configuration dependent.

2.3 Previous Research Work at BYU

Jensen (2004; 2005) designed and developed the Turbine Acceleration Deposition Facility (TADF) at BYU which can produce deposits in a 4-hour test to simulate 10,000 hours of turbine operation. Characteristics of deposits from the TADF were compared with characteristics from deposits taken directly from industrial turbines. This comparison demonstrated that the physical structure and chemical characteristics of the deposit sample from the TADF was consistent with deposits from industrial turbines.

Wammack (2005; 2006) performed experiments in the TADF to study deposit evolution on three different turbine blade coupons. The scaled-up plastic models of the rough surfaces from the topological measurements were placed in a wind tunnel to find the effect of the deposits on the heat transfer characteristics of a coupon surface. The work of both Jensen and Wammack were conducted with uncooled coupons, so that the coupon surface was near the gas temperature.

Crosby and coworkers (2007) performed experiments in the TADF to investigate how deposits were affected by particle size, gas temperature and sample surface temperature. The sample surface temperature was achieved by controlling the flow rate of cooling impinging on the backside of samples to simulate internal vane cooling. Flyash samples of coal, sawdust, petroleum coke, and petroleum coke were all used in deposition experiments in the TADF without any impingement cooling (Bons et al., 2007).

2.4 Literature Summary

Extensive physical models and numerical simulation models have been developed for film cooling technology to study the effect of various parameters on film cooling heat transfer. These parameters include blowing ratio, shape of the hole, hole spacing, surface toughness, density ratio, TBC layer, conjugate heat transfer and trench configuration. Some literature is available regarding ash deposition in land-based gas turbines and engines. The primary factors affecting the extent of deposition on turbine blades include: gas temperature, turbine surface temperature, net particle loading, particulate chemical composition, turbine blade exposure time, and geometric boundaries imposed on the flow. Each of these factors is not necessarily independent of the other factors, and so every combination of these factors can potentially change the film-cooling performance and consequently influence ash deposition. Therefore, there are a large number of operating conditions that need to be considered. Previous particle models treated the particle transport assuming that no particles rebound. However, particle sticking is affected by the chemical and physical properties of the particle and the impacted surface, as well as by gas temperature and properties. Moreover, little experimental research has been conducted to study deposition under the condition of film cooling. Evidence from serviced turbine hardware suggests that film flows do influence deposition. Therefore, it is essential to study the effect of film cooling on ash deposition to evaluate the operation of in-service gas turbines.

3. Objectives and Approach

3.1 Objectives

The overall objective of this research is to study particulate deposition on gas turbine blade surfaces with film cooling. The effect of conjugate heat transfer on deposition will also be studied. The research is divided into two tasks, as described below:

Task 1. Ash Deposition Measurements with Film Cooling

Ash deposition measurements were performed in the TADF with film cooling, both with and without a TBC layer. All measurements were performed on coal flyash entrained in the exhaust gases from a natural gas flame, with a gas temperature of 1180 °C and a Mach number of 0.25. Experiments were performed to examine the effects of cooling-hole geometry, blowing ratio, thermal barrier coating, hole spacing, particle size, and a trench configuration.

Task 2. Numerical Simulations of Deposition

Numerical computations were performed to describe the flyash deposition experiments on gas turbine disk samples with internal impingement and film cooling. The CFD code used was FLUENT (2005). The model was used to perform conjugate heat transfer calculations to determine quantitatively the temperature distribution and heat-transfer coefficient in the regions close to the film-cooling holes. Comparisons were made between the predicted and measured surface temperature distribution and flyash capture efficiency.

3.2 Approach

To achieve the objectives mentioned above, the following specific tasks were accomplished:

1. The turbine accelerated deposition facility (TADF) was modified to allow for backside impingement of coolant on the sample and generation of a coolant film over the sample surface. This included addition of a coolant heating system to achieve the proper density ratio.
2. Coupon samples were designed and manufactured with cylindrical holes and shaped holes, hole spacings of 3.4d and 4.5d, and with a trench. TBC sample coupons were obtained from industrial collaborators.
3. A series of deposition tests was conducted to determine how the deposition was affected by specific hole geometry, blowing ratio, holes spacing, ash particle size, trench configuration and TBC coating.
4. The sample surface temperature was measured using two-color pyrometry, based on the RGB signals from a camera to investigate the effect of deposition on the surface temperature pattern and film cooling effectiveness.
5. The topography of deposits on the surface of post-test samples was analyzed using a surface contact profilometer and Coordinate Measuring Machine.

6. A 3-D numerical computational model was developed with the GAMBIT and FLUENT software packages to quantify the film cooling effectiveness and the heat transfer coefficient, based on the testing conditions.
7. The deposition model was evaluated by comparison with measured ash deposition capture efficiencies as a function of ash particle size and coupon surface temperature.

4. Description of Experiments

4.1 Turbine Accelerated Deposition Facility

Experiments were performed in the Turbine Accelerated Deposition Facility (TADF), shown schematically in Figure 4.1. This facility was first developed and characterized for airborne particulate by Jensen et al. (2005). The facility is described briefly here. A horizontal stream of air flows into the base of the TADF. The flow is straightened by an aluminum honeycomb and enters the combustion region. Within this region, four upward curving tubes introduce partially pre-mixed natural gas, which is immediately ignited. A small fraction of the high-pressure air is directed through a particle feed system, consisting of a syringe driven by a frequency-controlled motor which can be adjusted to yield the desired feed rate. Particulate from the syringe is entrained into the flow and enters at the base of the combustor. The particulate is then heated in the combustor and brought to thermal and velocity equilibrium in a 1 m long tube with a 2.54 cm inner diameter before impinging on a circular turbine blade specimen held at a desired impingement angle within one jet diameter above the tube exit. The combustor is capable of operating at an exit Mach number of 0.25 and an exit temperature 1183 °C.

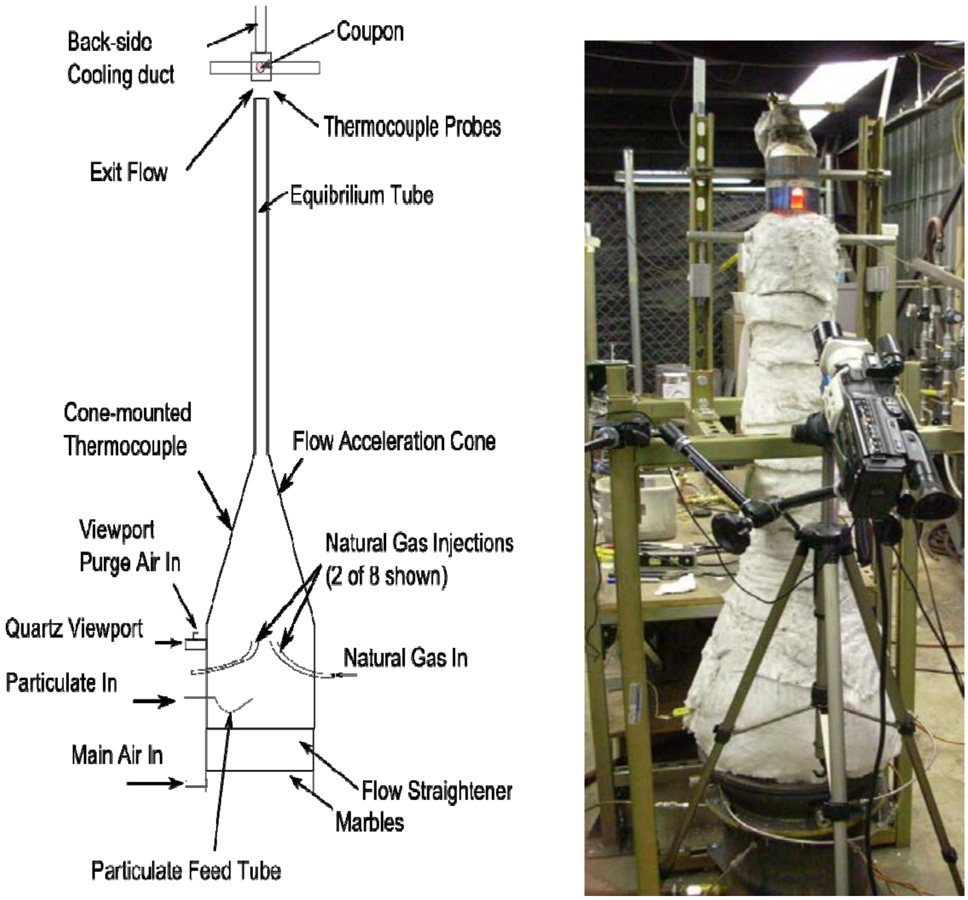

Figure 4.1 BYU turbine accelerated deposition facility schematic

To allow for both backside and film cooling of the coupon, the test specimen holder was redesigned as shown in Figure 4.2. The coolant chamber design simulates film cooling that is typically used in modern vanes and rotors. A cap was added to the top of the fixture so that coolant air exits only through the holes in the coupon. Also, the design allows for backside coolant temperature measurement using a thermocouple mounted 4 mm behind the coupon and in the center of the coolant air flow. The fixture was adjusted such that the particulate impinged upon the surface of the coupon at a specific angle. A cylindrical heat shield positioned around the test coupon limited radiative heat loss.

The mass flow of coolant was measured using a rotameter. The coolant air then passes through three cartridge heaters, each controlled by a variable voltage source, reaching the desired maximum coolant temperature of 430 °C. The air then passed by a quartz view port, which allowed optical temperature measurements to be taken at the backside of the coupon. A thermocouple measured the air temperature before entering the holes in the coupon.

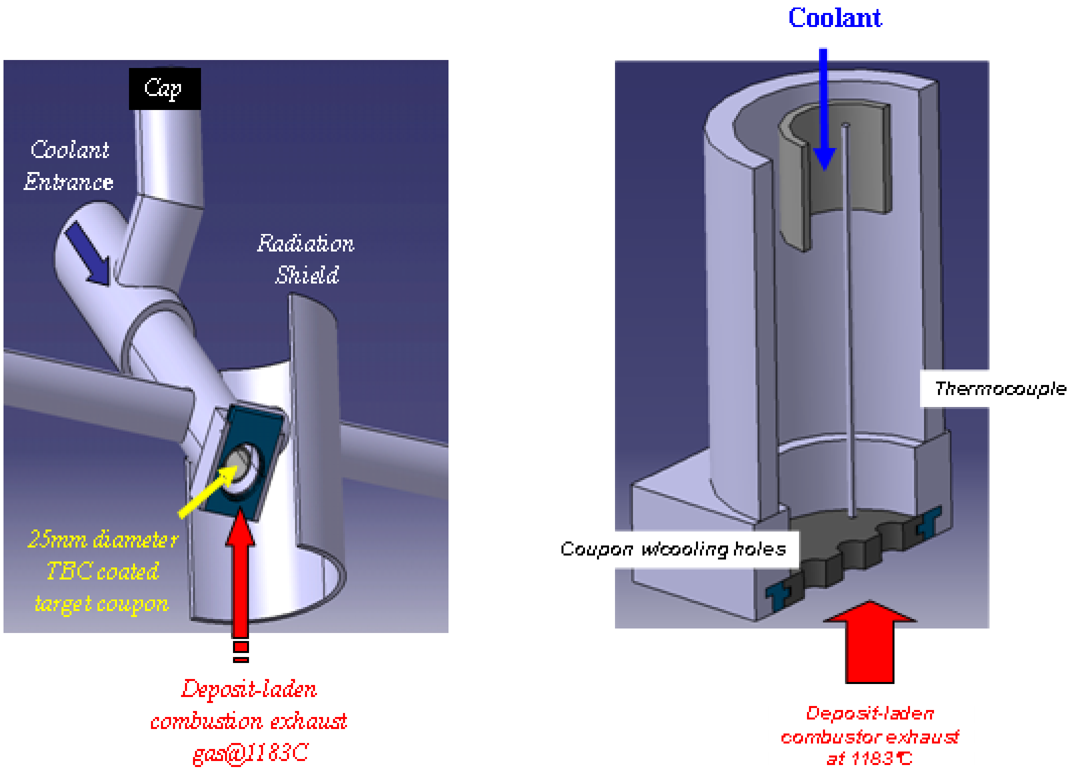

Figure 4.2 TADF test coupon holder redesign with backside film cooling

4.2 Particulate Feeding System

The amount of particulate injected into the combustor is a crucial parameter for accelerated deposition. The particle feeding system is shown in Figure 4.3. A function generator controls the speed at which a motor empties a syringe full of particulate into a glass bulb. A separate motor was connected to a brush and placed inside the bulb to help break up the particulate as it leaves the syringe. A vibrator prevents particulate from adhering to the inside of the bulb. To ensure the particulate flows to the combustor, air enters through the top of the bulb and exits out of the bottom while entraining the particulate to the combustor. It was assumed that the turbulent air flow makes particles free from agglomeration and distributes particles evenly before they enter the combustor.

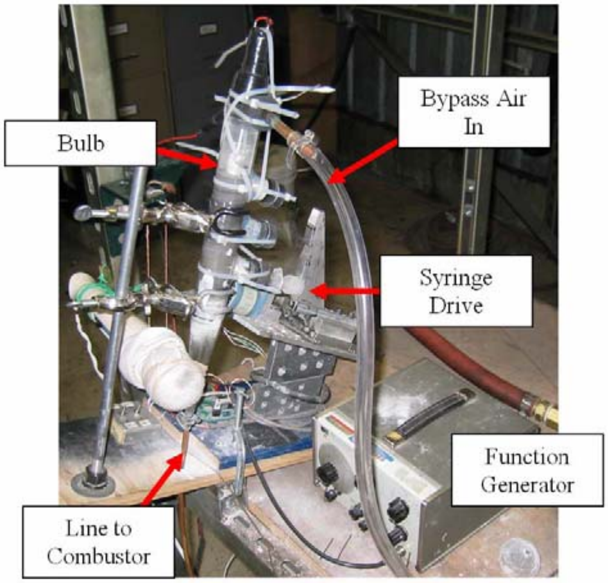

Figure 4.3 New particle feed system used in the TAD (2007)

4.3 Particulate Preparation

To simulate ash that could be entrained by the flow leading to the turbine, the particles must be small enough to pass through the various gas cleanup systems. Filtration systems in modern gas turbine power plants are designed to remove all particles with diameters greater than 10 μm. With inadequate or degraded filtration, these levels can be exceeded. The coal ash samples used in this study were the same as those described in Bons et al (2007). Subbituminous coal fly ash was obtained from an operating power plant, with a mass mean diameter of 13.4 μm as measured by a Coulter Counter. A smaller size fraction was used in the experiments described here, with a mass mean diameter of 4 μm. The two coal flyash particle size distributions are shown in Figure 4.4. A summary of ash characteristics is given in Table 4-1. The elemental composition of ash particle was obtained using ESEM and X-ray analysis.

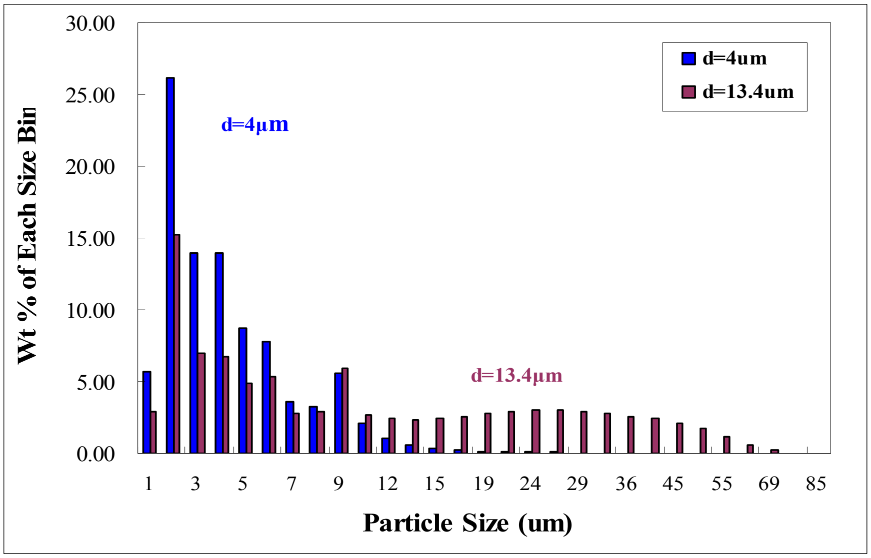

Figure 4.4 Ash particle size distribution

Table 4-1. Ash particle summary statistics: size, density, and average elemental composition. (2007)

Mass mean diameter	Bulk density	Apparent density	Element Weight (%)											
um	(g/cc)	(g/cc)	Na	Mg	Al	Si	P	S	K	Ca	Ti	V	Fe	Ni
13.4	0.99	1.98	6.9	3.6	18	47	1.6	1.8	2.6	8.7	1.6	0	6.4	0

4.4 Fabrication of Coupon with Film Cooling Holes

Sample coupons used in this project were metal disks made from typical turbine material. Figure 4.5 shows schematics of the two different hole-configurations, labeled cylindrical holes (**M1**) and shaped holes (**M2**). A row of three cylindrical holes used in this research provided circular injection with a 30 deg inclined angle θ relative to the free-stream. The inlet diameter (d) of each hole was 1.5 mm. The spacing between holes was 3 times the hole diameter. The middle hole exit was located in the center of the circular coupon, and the other two hole exits were located along a line of symmetry. The shaped holes had all the same geometric parameters as the cylindrical holes, except that the holes had a 10 deg forward diffusion and an additional 10 deg expansion in the lateral direction.

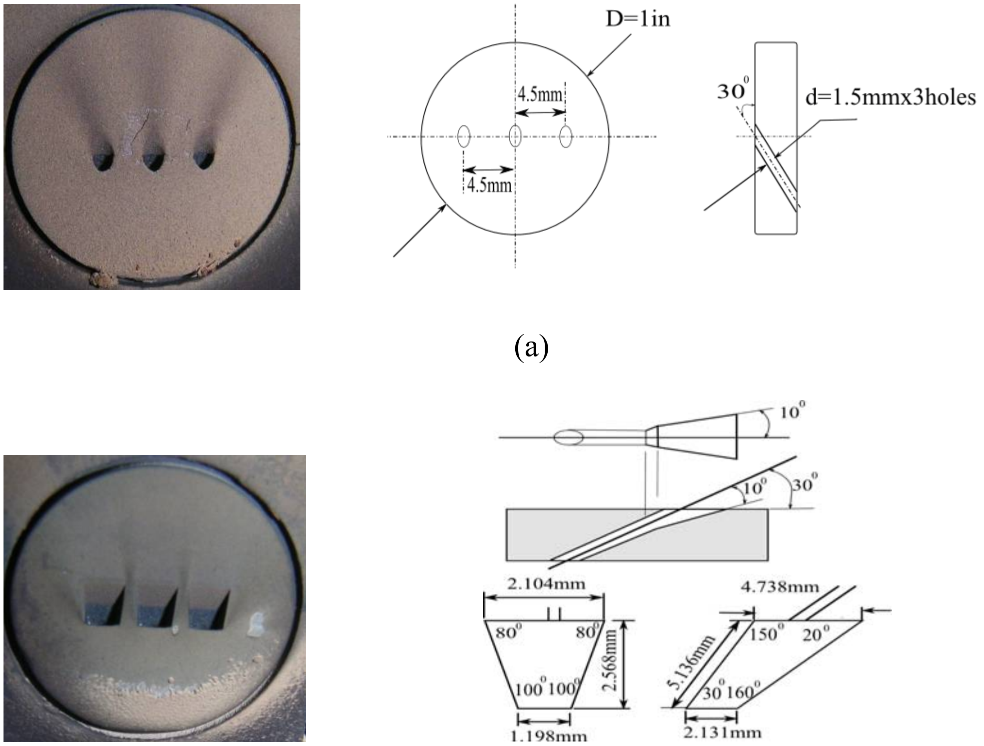

(a)

(b)

Figure 4.5 Geometry of coupon with a) cylindrical holes (M1) and b) shaped holes (M2)

The coated turbine sample coupons with film holes (TBC) were obtained from an industrial sponsor and consisted of a nickel base super alloy substrate approximately 0.3 cm thick. These samples contained two coatings: a High Velocity Oxygen Fuel (HVOF) CaNiMCrAlY bond coating and a Dense Vertically Cracked (DVC) thermal barrier coating (TBC). The samples are representative of a high-performance turbine material system. One of the sample coupons is shown in Figure 4.6. Five cylindrical holes with diameter 1.0 mm were lined across the center of the button like a film row. Their center-to-center spacing was 2.25 mm

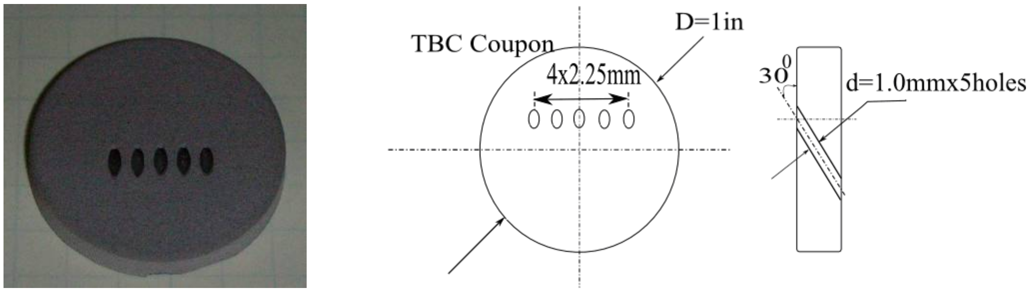

Figure 4.6 TBC sample coupon with cylindrical holes

To study the effect of hole spacing, two metal bare samples were manufactured with hole spacings of 3.37 mm **(M3)** and 4.5 mm **(M4),** respectively. These coupons had five cylindrical, 1 mm diameter holes. The two differing samples are shown in Figure 4.7. A row of five cylindrical holes provide circular injection with a 30 deg inclined angle relative to the coupon surface. The diameter (d) of each hole was 1.0 mm. The middle hole exit was located in the center of the circular coupon, and the other four hole exits were located along a line of symmetry. The coupons were made of Inconel alloy.

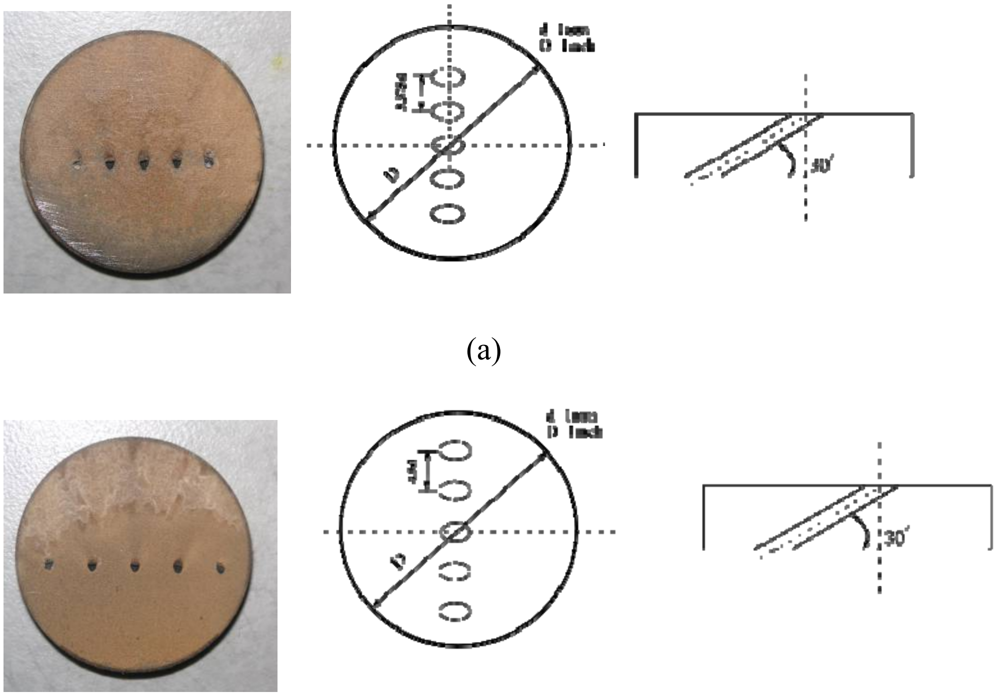

(a)

(b)

Figure 4.7 Cylindrical holes coupon with a) 3.75 mm spacing (M3), b) 4.5 mm spacing(M4)

The trench section in the literature summary above showed that the film cooling holes provide higher film effectiveness when embedded in a trench. In comparison to film-cooling holes without a trench, film-cooling holes with a trench reduced surface heat flux greatly. Thus, a coupon with a trench (M5) was manufactured to investigate the effect of the trench on deposition. Five cylindrical holes with diameter 1.0 mm were lined across the center of the coupon like a film row. Their center-to-center spacing was 2.25 mm (2.25d). The TBC layer on the coupon was removed completely by sanding, thus exposing the Inconnel surface. The trench was constructed in the metal surface as shown schematically in Figure 4.8a. The trench slot was 16 mm in length and 2.5 mm in width with a depth of 0.75 mm. The ratio of width and depth to hole diameter was 2.5d and 0.75d respectively. Based on the assumption that a narrow trench had a greater effect on film cooling effectiveness than a wide trench, the width of trench was set to 2.5d. Due to the trench geometry selected (depth = 0.75d & width = 2.5d) and the 30° inclined film holes, it was not possible to manufacture the trench such that the hole exits were completely confined to the trench floor. Either the windward edge of the hole would protrude partially from the upstream vertical wall of the trench, or the leeward edge of the hole would breach the downstream vertical trench wall. For the present study, the latter configuration was selected and the result was a notch in the downstream vertical trench wall at the exit of the holes (as shown in Figure 4.8a). This is a distinct departure from the configurations studied by others and must be considered in comparing results. The coating of an additional TBC coupon (M6) was removed for comparative baseline tests (see Figure 4.8b). The 2nd and 4th holes were blocked by using ceramic material in some tests to provide a hole spacing of 4.5d.

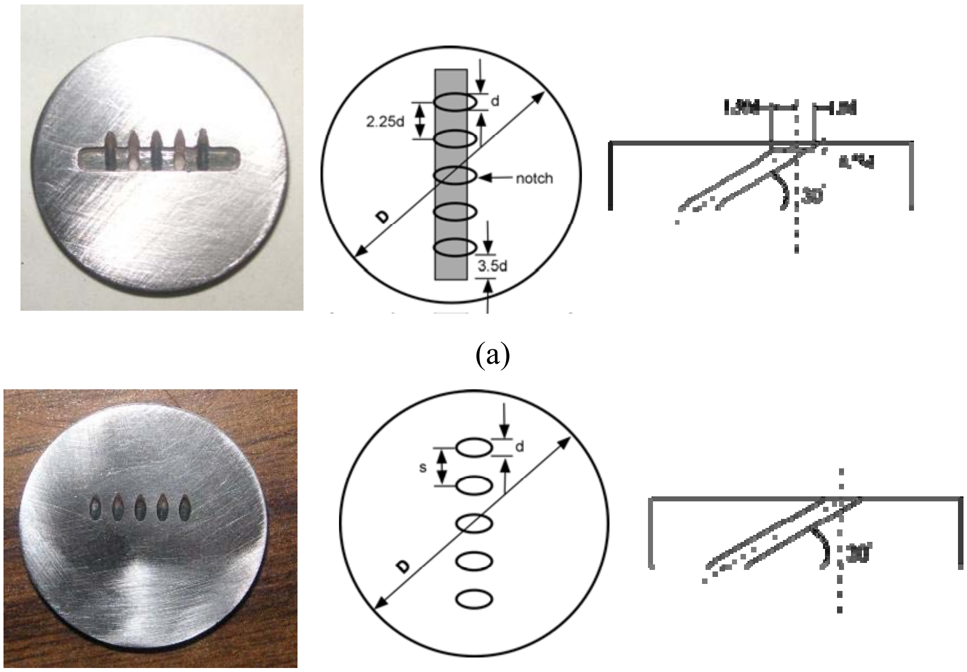

(a)

(b)

Figure 4.8 Bare metal coupon (a) with s/d=2.25 and a trench, (b) without a trench

4.5 Temperature Profile Measurement

The temperature of the coupon surface exposed to the jet exit was measured with an RGB camera. The technique used in the experiment was taken from Lu (2006) and Svensson et al. (2005), and used two of the three pairs of color signals from the RGB ports on a SVS285CLCS Sony Exview HAD CCD camera.

Detailed component specifications of the imaging system are shown in Table 4-2. The corresponding MatLab program was modified to determine the surface temperature at each pixel, allowing measurement of spatial temperature distributions.

Table 4-2. Components and specifications of the imaging system

Camera	SVS-285CSL, 10 bit, shutter speed, frame rate
CCD sensor	Sony ICX285AQ, Cell size 6.45x6.45 µm, Resolution 1036x1024
Lens model	Computer MLH-10X
Image acquisition board	Epix Inc. PIXCI D2X
Camera control software	XCAP2.0

The CCD detector in the camera collected light emitted from the coupon surface and converted the collected light to a voltage signal, which was then transferred to a frame grabber where it was digitized. In the RGB camera, the CCD array had a filter mask that transmitted light preferentially into red, green and blue signals. The measured spectral responses as a function of wavelength (λ) for each color from the RGB camera are shown in Figure 4.9. The digitized intensity was represented by an integral as indicated by the following equation

$$P_i = \int_{t_1}^{t_2} S_i \int_{\lambda_1}^{\lambda_2} \varepsilon_b I_{b,\lambda} \beta_\lambda \tau_\gamma \, d\lambda dt \qquad (4\text{-}1)$$

where P_i is the pixel count for color i and ε_b is the emissivity of the radiating body. During calibration, ε_b is the blackbody calibration source emissivity. During imaging, ε_b is the sample button surface emissivity. An assumption is made that the object is a grey body. Also, β_λ is the system spectral response, τ_γ is the spectral transmittance of any additional optics such as neutral density (ND) filters, t_1 and t_2 are the initial and terminal times of object exposure in the camera, and S_i is the sensitivity constant converting incident light intensity to pixel count. If each of the variables (S_i, and $\beta_\lambda, \tau_\gamma$) is known and if the detector is linear (meaning that S_i is not a function of exposure time or incident intensity), then the pixel count, P_i, for a given color band becomes a function of only two unknowns, ε_b and I_λ, which are unique functions of T. Given two unknowns, any two of the three color bands can then be used to produce two equations, which can be solved for T and ε_b

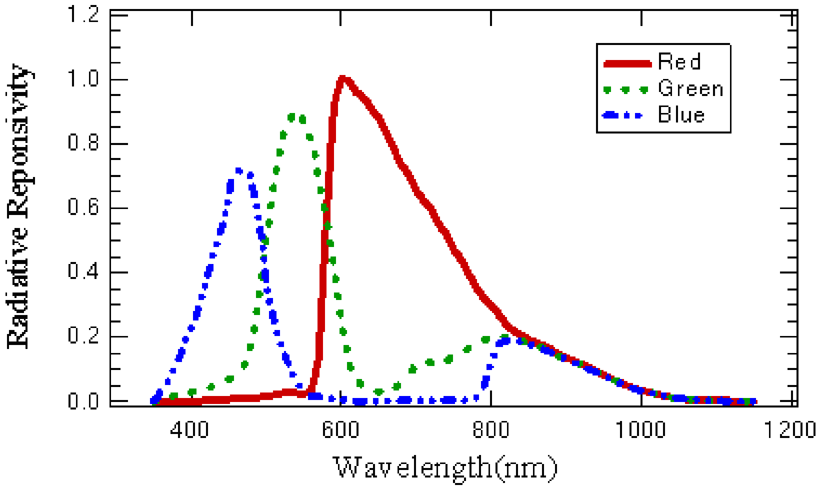

Figure 4.9 Measured relative spectral response of the SVS285CSCL (2006)

In the process of calibrating $S_{i,}$ the camera was placed in front of a Mikron M330 blackbody with the lens at the same level as the source and the working distance was adjusted to match that of the test. The camera was focused on the blackbody opening as the blackbody temperature was increased to the required value. The exposure time was changed to make the intensity number value close to, but less than, 1023 (the maximum value for 10-bit resolution). The exposure time was recorded as part of the calibration. Six images were obtained with the cameras once the temperature had stabilized at each temperature level. Using XCAP image processing software, a rectangular area of the image was chosen and saved, and the average intensity level of each color was determined. An average pixel intensity was then obtained from all the pictures at the same temperature level. Using the computational program Mathcad, the value of S_i was found for each color using a blackbody source at temperatures from 650 °C to 1250 °C.

In calibrating the camera for measurement of sample frontside temperature, the distance between camera lens and sample was 39.8 cm. The source temperature was varied from 900 °C to 1250 °C. The calibration results can be seen in the Table 4-3. The calibrated coefficients for each color (Red, Green and Blue) were 1.088, 1.121 and 1.135, respectively. The pair of red and blue colors with coefficient values of 1.088 and 1.135 was selected for the temperature measurements in this research due to the minimum standard deviation. The uncertainty of the front side temperature measurement was estimated to be 15 °C

The rear RGB camera was calibrated in the same way with a distance of 49.5 cm between the camera lens and the sample backside. The results are summarized in Table 4-4. The red-blue color pair with coefficients of 10.658 and 10.768 was employed in the calculation. The uncertainty of the back side temperature measurements is 7 °C. The front-side temperature measurement may have been affected by flame reflection, but no correction was applied.

Table 4-3. Calibration coefficients and the corresponding temperatures for the front camera

T(°C)	T Obtained from Camera (°C)		
Black Body	**R/G**	**G/B**	**R/B**
1250	1226	1228	1227
1200	1193	1194	1193
1150	1157	1156	1156
1100	1117	1115	1116
1050	1071	1069	1070
1000	1013	1018	1015
950	953	966	957
900	/	918	915
	Red	**Green**	**Blue**
Si	**1.088**	**1.121**	**1.135**

Table 4-4. Calibrated coefficients and the corresponding temperatures for the rear camera

T(°C)	T Obtained from Camera (°C)		
Black Body	**R/G**	**G/B**	**R/B**
1000	991.319	996.667	993.138
950	948.959	953.586	950.492
900	904.719	906.612	905.331
850	857.12	857.383	857.203
800	805.875	802.662	804.912
750	755.73	749.94	753.957
700	704.683	699.796	703.197
650	642.536	640.664	641.967
	Red	**Green**	**Blue**
Si	**10.658**	**10.744**	**10.768**

4.6 Coupon Deposit Analysis

The surface of the coupon was analyzed with a Hommel Inc (Greenport, NY, US). Hommelwerke LV-150 profilometer equipped with a TK100 stylus, which employs contact technology to measure surface profiles, roughness, waviness and other finish parameters. The Hommel profilometer ran the stylus across the surface of a sample. This direction of motion was defined as the x direction. Height variations (z direction) of the tip were recorded and then used to form a texture profile. Once a traverse had been made, the profilometer returned to its start position (i.e, x=0) and stepped a certain distance in the y direction, which was also user-defined. The profilometer then repeated this process until the predetermined number of steps had been made. The profilometer was set to measure a rectangular region located roughly in the center of the circular coupon. A typical scan of a coupon with cylindrical film cooling holes was 15 mm by 15 mm, and included approximately 750 single scans. After these scans were completed, the 750 single scans were compiled into roughness maps using the software Hommel Map Expert version 3.1.7. The measurements were exported as text files containing x, y, and z coordinates. Information acquired from these surface profiles was used to make scaled models of the deposit-laden film holes for wind tunnel testing (Wammack, 2005). A statistical evaluation of the roughness of the deposits formed by the TADF with film cooling was made to describe the effect of film cooling on deposition. These statistics are useful in predicting the convective heat transfer properties of each roughened surface. The profilometer scan was used for cases where small amounts of deposition were obtained at high blowing ratios, since the deposit peaks were too high in other cases.

For the case of the large thickness of deposit obtained in the tests at low blowing ratio or without coolant, the surface of the coupon after testing could not be scanned by the Hommel profilometer. Therefore, a Coordinate Measuring Machine (CMM) was used to scan the surface, which employs non-contact technology. This work was done on a Brown and Sharpe Global Image CMM with a Renishaw PH10M head and a Perceptron ScanWorks Contour Probe. PC-DMIS metrology software was used to operate the hardware and perform measurements. The machine used laser beams that were projected against the surface of the part to obtain the coordinates of points on the object surface for the measurement of the dimensions. Many thousands of points can then be taken and used to not only check size and position, but to create a 3D image of the part as well. This "point-cloud data" can then be transferred to topography software or other software to create a working 3D model of the part. This method of CMM inspection is more accurate than the conventional touch-probe method and many times faster as well.

The statistical parameters obtained for this study were the centerline averaged roughness, Ra, and vertical distance of highest peak and lowest valley, Rt. The centerline averaged roughness Ra was calculated using the following equation:

$$Ra = \frac{1}{IJ}\sum_{i=0}^{I-1}\sum_{j=0}^{J-1}\left|z_{i,j}\right| \tag{4-2}$$

where z is the height of an individual roughness element. Rz was calculated as the mean of the vertical distance between the five highest peak points and five deepest valley points.

4.7 Test Details

All deposition experiments were performed in the TADF. The tests were run under standard combustor operating conditions (gas exit temperature =1183±5°C, Mach = 0.25). In every test, the coupon experienced approximately one-and-a-half hours of warm-up time, during which the TADF was brought to an operational freestream temperature of between 1145ºC and 1155ºC (uncorrected thermocouple reading value) and the temperature of coolant to the film cooling holes reached the specific test value. Once steady state was reached, the particulate was introduced into the facility for a specific period of time. The combustor shut-down was conducted slowly (e.g. -50 K every 10 minutes) to minimize deposit flaking. During each test, the coolant temperature at the entrance to the film cooling holes was measured by a thermocouple 4 mm away from the backside of the coupon to determine the density ratio. The airflow provided for combustion was adjusted by a pressure regulator upstream of an orifice plate. The coolant flow was measured and controlled by a rotameter. The flow rate determined by the rotameter was corrected for the measured coolant temperature and pressure (obtained from a K-type thermocouple and a pressure gauge). The outputs from the pressure transducers and K-type thermocouples mounted just upstream of the orifice plates were connected to a National Instruments SCXI chassis. These pressure and temperature data were monitored by a LabVIEW VI program, which allowed the operator to maintain the proper mass flow rate of the air. The natural gas flow rate was measured with a rotameter with an attached pressure gauge. This flow rate was adjusted by using the rotameter to maintain the desired gas exit temperature. The combustor exit temperature was measured using two 0.8 mm diameter Super OMEGCLAD K-type thermocouple probes, one of which was mounted just inside the equilibration tube while the other was movable. The probes were connected to a National Instruments NI SCXI-1112 thermocouple module mounted in an NI SCXI-1000 chassis. The signal was passed to the same LabVIEW VI program through the interface hardware. The LabVIEW VI program calculated the total gas mass flow rates for the combustor and coolant air.

An RGB camera measured the frontside surface temperature, which initially was the metal or TBC surface temperature. The camera measured the surface temperature of the deposit layer later in the deposition tests. A different RGB camera measured the backside surface temperature simultaneously through a view port, which could withstand temperatures as high as 350ºC, During the test, the RGB camera for temperature measurement of the frontside of the coupon was kept 39.8 cm away from the coupon front surface, while the other RGB camera located behind the fixture holder was located 49.5cm directly behind the backside of coupon. The distance from the coupon was set to be the same distance as that in the calibration to reduce error. Images were taken multiple times throughout the course of a test. Images from the front and backside were taken at approximately the same time. First, images were taken at a frequency of 6 or 4 times per hour before the start of deposition. After the start of the particle feeder, pictures were taken at regular time intervals until the end of the test. The images were grabbed using the software XCAP, which recorded the intensities of each color at every pixel. The corresponding MatLab program was modified to determine the surface temperature at each pixel, allowing measurement of spatial temperature distributions.

5. Experimental Results and Discussion

5.1 Hole Geometry

To study the effect of hole geometry on deposition, two series of experiments were performed on coupons with cylindrical holes and shaped holes. The test conditions are described in Table 5-1. The density ratio in these tests ranged from 2.1 to 2.4. Crosby et al. (Crosby, 2007) showed that slow shut-down of the combustor after the test minimized deposit flaking. Minimal flaking was observed in the current tests using this same slow shut-down procedure. Images of deposits were obtained immediately after slowly cooling the combustor to a complete shutdown, before removing the coupon from the holder.

Table 5-1. Coupon configuration category and test conditions for hole geometry

Case	# of holes	Hole geometry	Hole size (d)	Hole spacing	Impingement angle (α)	Blowing ratio	Testing time
M1	3	cylindrical	1.5mm	3d	45°	0,0.5,1.0,2.0	4 hr
M2	3	Shaped	1.5mm	3d	45°	1.0,2.0	4 hr

5.1.1 Cylindrical Holes, Metal Coupon (M1)

The blowing ratio M is one of the most important parameters affecting film cooling effectiveness and heat transfer. The blowing ratio was changed (M = 0.5 to 2.0) in the tests using Coupon M1 to study the variation of ash deposition. Typical blowing ratios used in actual turbines for the suction side are 1.5 near the leading edge and 1.0 before the gauge point. On the pressure side just downstream of the leading edge, the blowing ratio is 2-4 but is close to 1.0 at the trailing edge. Therefore, the range of blowing ratios used in these tests is representative of actual conditions. The same coupon was re-used after each deposit analysis was completed; i.e., the deposit was ground off and then the coupon surface was refinished to a centerline-averaged roughness (Ra) value of 0.3-0.6 μm.

Figure 5.1 shows post-test images of the test coupon at different blowing ratios. The images show the deposit distribution before and after the cooling holes. The flow channels seen downstream of the left and right side holes deviated somewhat from the expected streamwise direction due to the finite number of holes. This effect became less pronounced with increasing blowing ratio. Assuming that the white streaks in each of the images represented the path of coolant flow, it is clear that the coolant exiting the film cooling holes provided little or no coverage in the region between neighboring holes, and then spread out laterally at downstream locations. Increasing the blowing ratio created film flow patterns that were more aligned with the streamwise flow. This indicates that

a)M=0.6 b)M=1.0 c)M=1.5 d) M=2.0

Figure 5.1 Post test images of deposits on M1 coupon at various blowing ratios

the coolant stream momentum increased due to the increase in blowing ratio, resulting in increased resistance to front-side gas flow impingement.

The coupons were weighed before and after the deposition experiments and the net deposit weights were recorded. The capture efficiency is defined here as the mass of deposit divided by the mass of ash fed into the reactor. As the blowing ratio increased from 0.6 to 2, the capture efficiency decreased by 50%, as shown in Figure 5.2. These results suggest that blowing ratio plays an important role in decreasing deposition on gas turbine blades. The relative uncertainty in the measured net capture efficiency was less than 1% in deposit weight for all tests. The uncertainty analysis was conducted on all of the deposition metrics using the partial derivative method on the equations used to calculate them (Crosby, 2007).

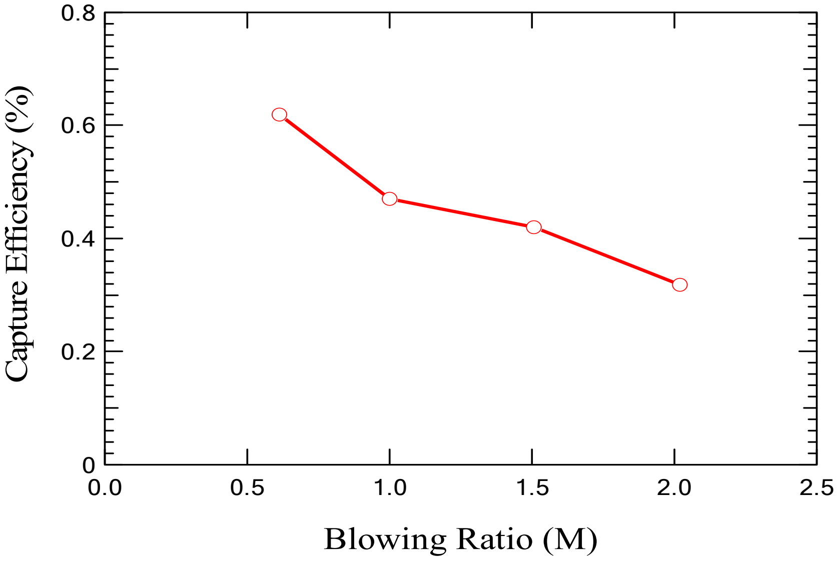

Figure 5.2 Effect of blowing ratio on net capture efficiency of cylindrical hole metal coupon (M1)

Figure 5.3 shows the comparison of the surface height maps (obtained from the profilometer) from three deposition tests with different blowing ratios. The deposit height here is a relative value. The ridges between film cooling holes were apparent at a blowing ratio of 2 but not apparent at M = 1. The tests corresponding to Figure 5.3a and b had comparable capture efficiencies (0.42% and 0.47% respectively), yet the ridges were slightly more visible in Figure 5.3b. These data illustrate the impact that blowing ratio had on the deposit pattern and height. Note that the height scale here was from the minimum deposit height, not from the metal surface.

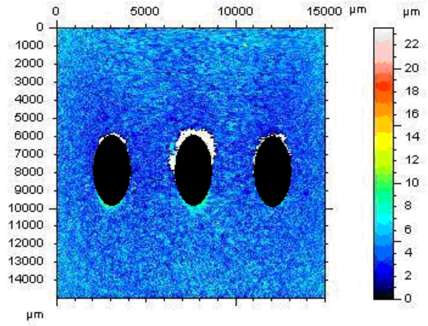

a) M=1.0

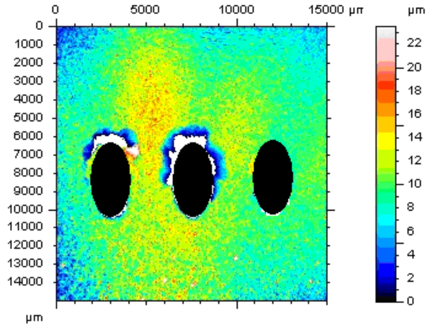

b) M=1.5

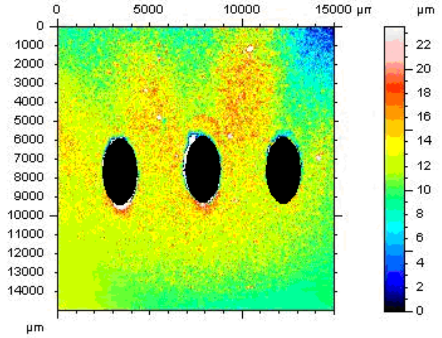

c) M=2.0

Figure 5.3 Surface maps of deposit height for C-M1 coupons obtained at three different blowing ratios. (Hole locations are approximate)

Metal surface temperature is a significant factor affecting the extent of deposition as well as coolant momentum (Crosby et al., 2007). Due to the coolant injection from the film hole, the metal surface temperature distribution was no longer spatially uniform. The temperature maps of the front side of the coupon at different times are shown in Figure 5.4 at a blowing ratio of 2.0. These temperature maps were plotted versus pixel number. The approximate location of the cooling holes is shown for reference. At the beginning of the test, before deposition occurred, the coolant paths downstream of the holes were not identifiable from the temperature maps (Figure 5.4a). As the particulate accumulated on the surface, a temperature pattern resembling the deposit roughness pattern in Figure 5.3 became evident. Similar temperature patterns were observed at other blowing ratios.

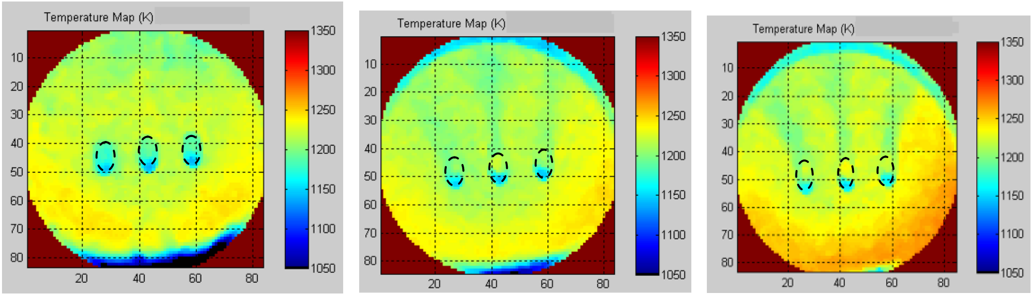

a) 1 hr deposit b) 2 hr deposit c) 3 hr deposit

Figure 5.4 Coupon front-side temperature map at the blowing ratio 2.0

As deposits form in the regions between the cooling holes, the surface temperature of the deposit rose due to lack of cooling and increased deposit thickness (i.e., proximity to the hot gas flow). Since deposition increased with increased surface temperature, the deposit grew faster in these between-hole regions, and not in the cooler surface temperature region in the cooling flow channels. In addition, the clean coolant spread over the surface before mixing with the freestream and shielded the surface from particles. As blowing ratio increased, the channeling effect increased, sweeping particles away in the flow channel and causing non-uniform deposit patterns.

Although the RGB camera measures detailed distributions and contour data over the entire viewing domain, it is instructive to examine spanwise temperature profiles at differing streamwise paths for quantitative comparison. Figure 5.5b shows the spanwise variation of local temperature at two streamwise locations: y/d= 0.5 and 2.0 after a few miniutes deposition test. The origin of x and y is located at the downstream edge of the center hole and does not correspond to the labeled distances on the axes in the figure. The coolant flow paths were visible at both streamwise locations in Figure 5.5b, although the channels on the right- and left-hand sides deviated slightly from the streamwise direction. Since the y/d = 0.5 line crossed the flow channels, three temperature valleys were easily visible.

To further verify the proposed mechanism of deposition on the film-cooled coupons, a test was conducted at the same test conditions except for an increased particle feed rate (corresponding to 75 ppmw in a 4-hr test). The coupon used in this test had some deposit residue from a previous deposition test, although much of the deposit had flaked off after the first test. The re-deposition test lasted an additional 4 hours beyond the initial deposition test. The deposit pattern seen in Figure 5.6 was well defined between the downstream passages of the film holes. The coupon surface temperature was not uniform because the area downstream of the coolant holes was at a lower temperature than the area exposed directly to the high temperature mainstream. The deposit formed initially in the high-temperature regions between cooling holes, where local heat transfer from the cooling jets was low, resulting in more deposit forming readily in these locations. These deposit roughness features bear resemblance to roughness measurements made by Bons et al. (2001) on serviced film-cooled turbine components. Figure 5.6b shows a “furrowed” pattern of roughness downstream of two film cooling holes (drawn to the left of the figure) on a first stage turbine vane.

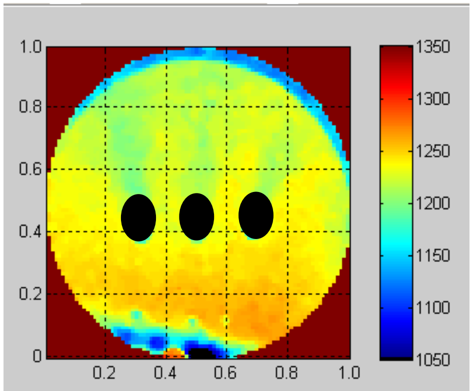

(a)

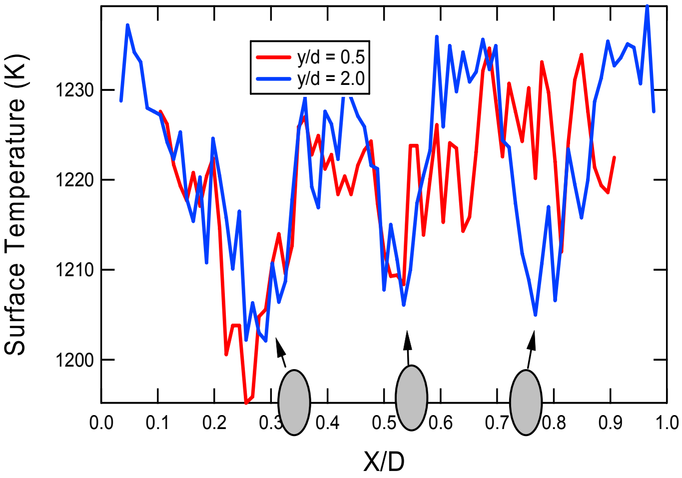

(b)

Figure 5.5 **(a) The temperature map for this condition. (b) Spanwise distribution of temperature for cylindrical holes at y/d = 0.5 and 2, M = 1.5. Gray circles represent hole positions**

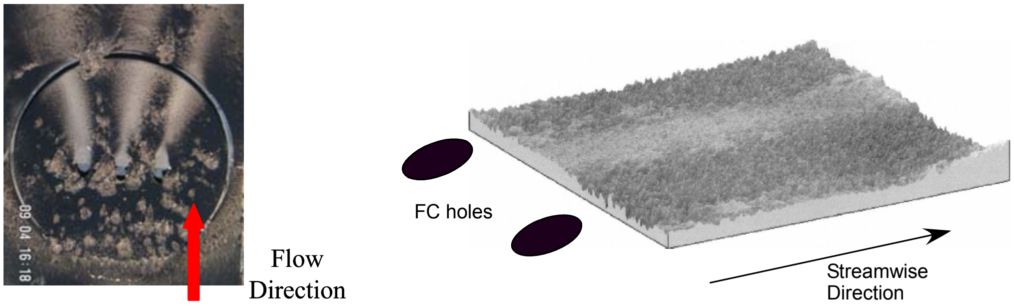

(a) TADF deposits (b) Serviced turbine blade deposits

Figure 5.6 (a) Photo of deposits at high loading in the TADF. (b) Roughness plot of the surface of a deposit on a serviced turbine blade. Note visible "ridges" of deposit between film cooling holes

5.1.2 Shaped Holes, Metal Coupon (M2)

Two tests were performed in the TADF at blowing ratios of 1.0 and 2.0, using coupon M2 with shaped cooling holes. The blowing ratio for the shaped holes was based on coolant mass flux at the inlet of the cooling hole rather than the exit velocity, and hence the testing conditions were similar to those used in the tests on coupons with cylindrical holes (M1). Figure 5.7 shows post-test images, which were taken immediately after the slow shutdown of the combustor. The images show the effect of the shaped holes on the streamwise and spanwise distribution of the deposit. The lighter section in the image shows that the area affected by the shaped-hole coolant was larger than that of the cylindrical holes. Cooling areas from individual holes almost overlap. The dark area in these images actually came from soot from the natural gas flame, which was caused by incomplete combustion during the shutdown procedure. The film cooling did not permit soot deposition downstream of the cooling holes. The thin layer of soot deposition was small (< 1% on a weight basis); subsequent tests were made using a procedure to avoid soot deposition.

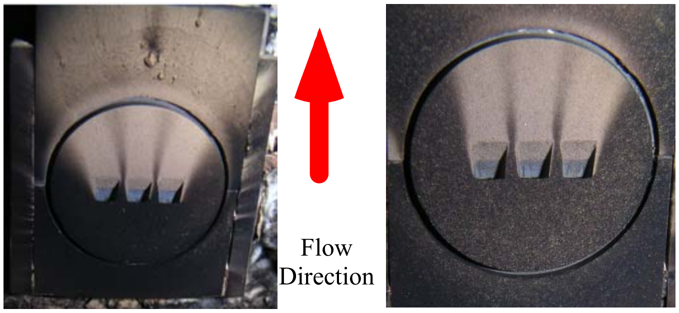

(a) (b)

Figure 5.7 Post test images of deposits on the shaped hole coupon at two blowing ratios (a) M=1.0, (b) M=2.0. Both tests ran for four hours

The capture efficiencies for the shaped holes were 0.81% for M = 1 and 0.24% for M = 2. The trend in capture efficiency versus blowing ratio for shaped holes was the same as for cylindrical holes. For M = 2, the capture efficiency (0.24%) for shaped holes was lower than observed for the corresponding cylindrical hole condition (i.e., 0.32%). This indicates that shaped holes reduced the surface deposit more efficiently than cylindrical holes at this blowing ratio. At M = 1, the capture efficiency measured with cylindrical holes (0.47%) was lower than for the shaped holes (0.81%). It is possible that there was an exit velocity threshold between these two blowing ratios where the shaped holes became more efficient. These numbers are also influenced by the fact that less than one half of the coupon surface was affected by the coolant flow path.

The temperature map from a shaped-hole test is shown in Figure 5.8. The film-cooling-hole exits of the shaped holes were closer together than the cylindrical holes, which gave rise to the uniform temperature in the entire lateral region downstream. The enlarged cooling flow coverage by the shaped holes seemed to be effective in preventing deposition.

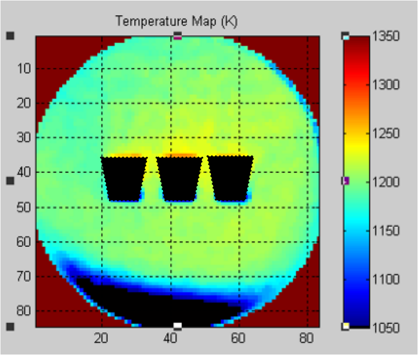

Figure 5.8 Temperature map of shaped hole coupon during deposition testing at M = 2.0

5.2 Effect of TBC Layer

In order to investigate the effects of TBC layer with film cooling holes on particle deposition with the variation of blowing ratio, 1-hour deposition tests were conducted on TBC coupons and a bare metal coupon with same configuration. Blowing ratios ranged from 0.0 to 4.0 and the density ratio was in the range of 2.2-2.4. The M = 0.0 test was conducted with no coolant flowing through the holes and no impingement cooling. The interior passage of the cooling fixture was insulated with blanket insulation material. The 1-hr tests enhanced the observed deposit pattern due to a higher particle loading (310 ppmw instead of 40 ppmw). The initial hole spacing of 2.25d obscured the effect of blowing ratio for these 5-hole coupons. Therefore, the second and fourth holes were plugged with insulation, giving a hole spacing of 4.5d for the remaining three holes. The testing conditions and coupon configuration are listed in Table 5-2

Table 5-2. Coupon configuration category and testing conditions for the study of TBC effect

Case	# of holes	Hole geometry	Hole size (d)	Hole spacing	Impingement angle(α)	Blowing ratio	Testing time
TBC	3	cylindrical	1.0mm	4.5d	45°	0,0.5,2.0,4.0	1 hr
M4	3	cylindrical	1.0mm	4.5d	45°	0,0.5,1.0,2.0	1 hr

*TBC means with thermal barrier coating, and M means bare metal coupon

5.2.1 TBC Coupon (TBC)

5.2.1.1 Surface deposition pattern

Figure 5.9 shows the deposition pattern on the TBC coupon as a function of blowing ratio. Images of the deposition pattern on the sample were taken immediately after the combustor was shut down. When no coolant was used, the sample was found to be almost entirely coated by an uneven deposit. The deposit in the central section, where the particles first impinged on the surface, was larger than that in the peripheral locations. The sample tested at a blowing ratio of 0.5 showed that deposition was lessened somewhat downstream of the cooling holes. The extent of deposition upstream, however, was similar to the no-coolant condition. On an operating turbine, the roughness of the upstream deposit increases the turbulence intensity of the main flow and has a significant negative effect on the area-averaged cooling effectiveness (Goldstein et al., 1985). Figure 5.9b-c show partially-blocked cooling holes, which changes the momentum and trajectory of the cooling jet (Sundaram et al., 2007).

The effect of blowing ratio in the reduction of deposition is especially significant downstream of the coolant holes. As seen in Figure 5.9, regions of dramatic spatial variation of deposition were developed downstream of the film cooling holes at the elevated level of blowing ratio. Three distinct furrows appeared downstream of the holes on the sample tested at a blowing ratio of 2.0. In general, the presence of deposit will affect the average effectiveness the lateral distribution of the local effectiveness and heat transfer. The large trenches appearing here certainly curtail spanwise diffusion of the coolant and may inhibit jet blow-off altogether.

Very little deposition appeared downstream of the coolant holes when the blowing ratio increased to 4.0. The deposition in the central location was apparently less than at other blowing ratios. This was partially caused by the increase of coolant mass flow resulting in an enhancement of backside impingement cooling. Perhaps the more important reason was that coolant stream with a high blowing ratio improved the flow field in the portion near the surface downstream cooling holes and reduced the opportunities of particles arriving at the surface

a) M=0 b) M=0.5 c) M=2.0 d) M=4.0

Figure 5.9 Variation of deposit patterns on the C-TBC surface with blowing ratio from M=0 to M=4

5.2.1.2 Spanwise temperature distribution

Lateral temperature distributions downstream of film cooling holes at different blowing ratios are shown in Figure 5.10. Three streamwise trenches are identified from the minimum temperatures in the M=2.0 case. The lateral average temperature at the location of y/d = 2.5 increased from 1227K to 1305K with the decrease of blowing ratio from 4.0 to 2.0. The average temperature at the value of M=4.0 dropped below the critical value necessary for deposition, and thus mitigated deposition. Due to the significance of metal surface temperature during deposition, the temperature map, together with the deposit patterns, illustrates the great effect blowing ratio has on deposition. These results suggest that film cooling reduces the metal surface temperature, dilutes particles concentration impacting on the coolant passage of target surface, and is responsible for the generation of furrows in the deposit pattern.

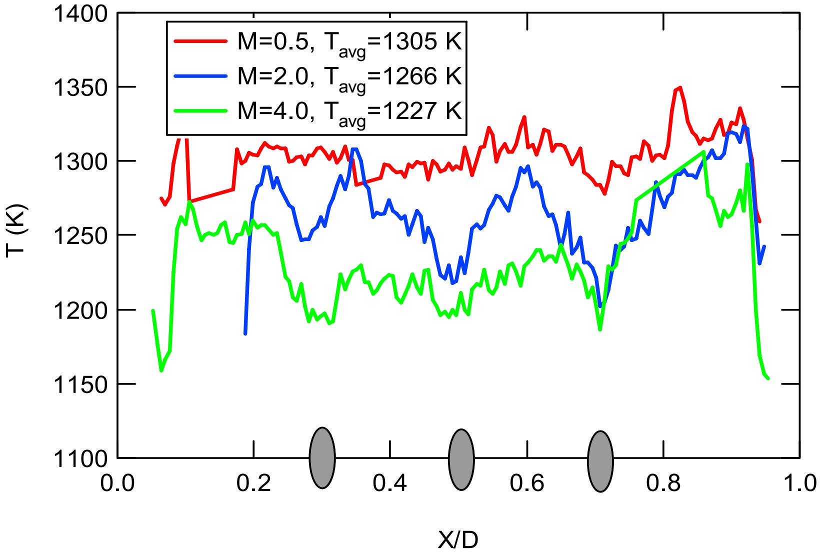

Figure 5.10 Spanwise distribution of temperature for the C-TBC tests at y/d=2.5, M=0.5, 2.0 and 4.0 respectively. Gray circles are the approximate hole locations

5.2.1.3 Deposition development

The deposit behavior show considerable variablility, not only with coal type and combustion condition, but also with time. The development of the deposit as a function of time in the M = 2.0, 1-hour test, is illustrated in Figure 5.11. In the initial 20 minutes, little deposition was observed on the sample surface. However, a defined deposit pattern formed rapidly in the following 10 minutes, and a large portion of the surface was covered with a massive deposit in the next 30 minutes. This non-linear deposit pattern is consistent with the mechanism of deposition discussed above, where the surface temperature of the deposit increased as the deposit grew, thereby enhancing the capture efficiency. This result also implies that regular cleaning at early stages of deposition might keep deposition rates low. Baxter and Hencken (1990) documented that deposit initially increased with elapsed time. As the deposit grew, it often became unstable and collapses. This deposit shedding generally starts rather slowly. Finally, the deposit shedding became catastrophic, releasing big flakes. This process was repeated over time, with the deposit peak height increasing for each subsequent cycle.

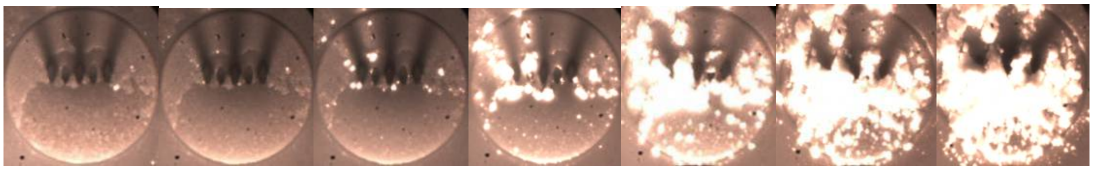

0 min 10 min 20 min 30 min 40 min 50 min 60 min

Figure 5.11 Deposit development with the elapsing time at the value of M=2.0. (C-TBC test series)

The effect of blowing ratio on surface coverage by the deposit as a function of time is shown in Figure 5.12. A number of similarities were observed for the three tests. All three tests showed an initial period of approximately 20 minutes where no deposits adhered to the surface. Following this initial period, deposits slowly began to accumulate on the coupon. After the initial accumulation, the coverage growth rate increased substantially until a maximum growth rate was obtained. This deposit growth behavior suggests that the entrained particles more readily adhere to coupon surfaces that have some initial deposit coverage as opposed to clean, smooth surfaces.

Figure 5.12 also shows that both the resultant percentage covered as well as the maximum rate of coverage values decreased with the blowing ratio. The deposit growth was shown to occur mostly between or upstream of the coupon holes as opposed to directly in the coolant path. The trends observed are consistent with the increased cooling and, hence, lower surface temperatures with higher blowing ratios

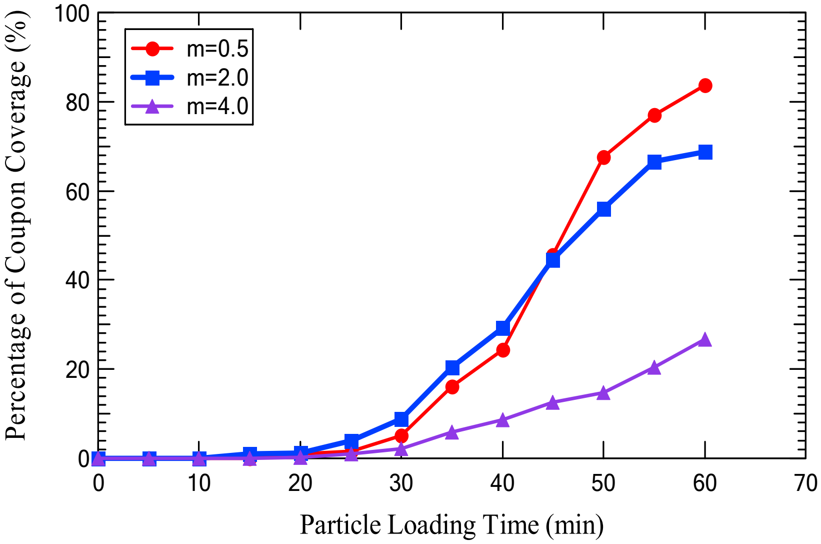

Figure 5.12 Influence of blowing ratio (M) on deposit surface coverage at a set particulate loading rate

5.2.2 Bare Metal Coupon with s/d= 4.5 (M4)

A series of tests was conducted on a bare metal (M4) coupon with s/d = 4.5 at blowing ratios from 0 to 4.0 to compare with the TBC coupon tests with s/d = 4.5. The M = 0 test was performed without coolant flowing through the holes and the coupon backside was insulated by a ceramic blanket material, resulting in a near adiabatic condition. Holes 1 and 5 were blocked for all other tests to compare with the TBC coupon tests at s/d = 4.5 with 3 holes.

5.2.2.1 Surface deposit pattern

The deposit pattern shown in Figure 5.13 for M=0 appeared similar to that of M=0.5. The surface was entirely covered by the deposit at M = 0. The sample tested at M = 0.5 shows that the cooling holes were blocked by deposition. These deposits were not tenacious, and a large portion of deposits flaked off shortly after the combustor was shut down. This flaking may be caused by a difference in thermal coefficient of expansion. It is thought that as the metal coupon cooled down and contracted, the deposits did not contract as much, causing thermal stress at the metal-deposit interface. Less deposit residues were observed on the M4 coupon at M = 2 than on the TBC coupon (Figure 5.9c) due to the higher surface temperatures of the TBC coupon caused by the difference in thermal conductivity. Deposits on the TBC coupon formed inside the cooling holes and adhered to the inner coolant passage, even blocking the holes, which deteriorated cooling performance.

M=0 M=0.5 M=1.0 M=2.0 M=4.0

Figure 5.13 Variation of deposit patterns on bare metal coupon with three holes, s/d = 4.5, and blowing ratios from M = 0 to M = 4.0

Deposition was mitigated slightly at M = 1.0. The effect of blowing ratio in the reduction of deposition is significant with the increase of the blowing ratio to M =2.0. As seen in Figure 5.13, the amount of deposit at M = 2.0 decreased substantially compared with the low blowing ratio cases. Deposition was concentrated in only a few small areas on the surface. In the M=4.0 test, no large deposits were observed. In general, the deposition upstream of the cooling holes in these tests was mainly influenced by the increase of coolant flow rate, resulting in the enhancement of internal heat transfer. The combined heat transfer of internal and external coolant led to a reduction of deposition over the entire surface at high blowing ratios.

5.2.2.2 Temperature distribution

Lateral temperature distributions measured in the middle of each test at the location y/d = 2.0 downstream of the film cooling holes are shown in Figure 5.14 as a function of blowing ratio. The spanwise average temperature decreased from 1301 K to 1190 K when the blowing ratio increased from 0.5 to 2.0. The coolant temperature at the entrance to the film cooling holes increased in these tests with blowing ratio, which in turn increased the density ratio 1.5 to 2.2. Therefore, the difference in spanwise average temperature and deposit pattern was attributed to the variation of both the blowing ratio and density ratio. Three small valleys were observed in the M = 1.0 temperature profile in Figure 5.14, but not for the M = 0.5 and M = 2.0 cases. The 3 small valleys indicate that at M = 1 the jets had not merged completely in the spanwise direction. At M = 0.5, the coolant stream was overpowered by the main gas stream. At M = 2, some blowoff may have occurred, which enhanced mixing/diffusion and causes a more rapid spanwise merging of the jets.

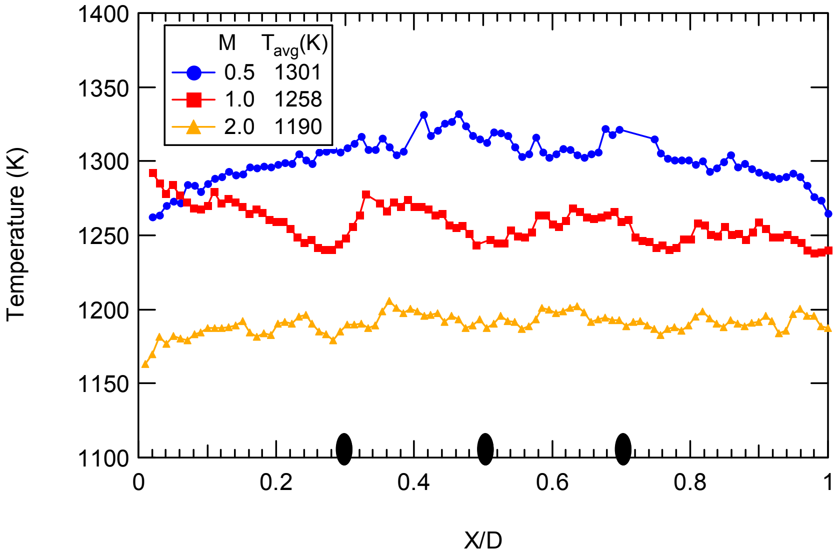

Figure 5.14 Spanwise distribution of temperature for the metal coupon 3 holes, s/d = 4.5 at y/d = 2.0, M = 0.5, 1.0 and 2.0, respectively

5.2.3 Comparison between Bare Metal Coupon and TBC Coupon

A comparison of capture efficiency for the M4 and TBC tests is shown in Figure 5.15. The capture efficiency for both coupons decreases with increasing blowing ratio. The tests with the TBC coupon had higher capture efficiencies than the metal coupon at each blowing ratio. These results suggest that the blowing ratio between values of 0.5 and 2.0 has a greater effect on capture efficiency for the bare metal coupon than for the coupon with TBC.

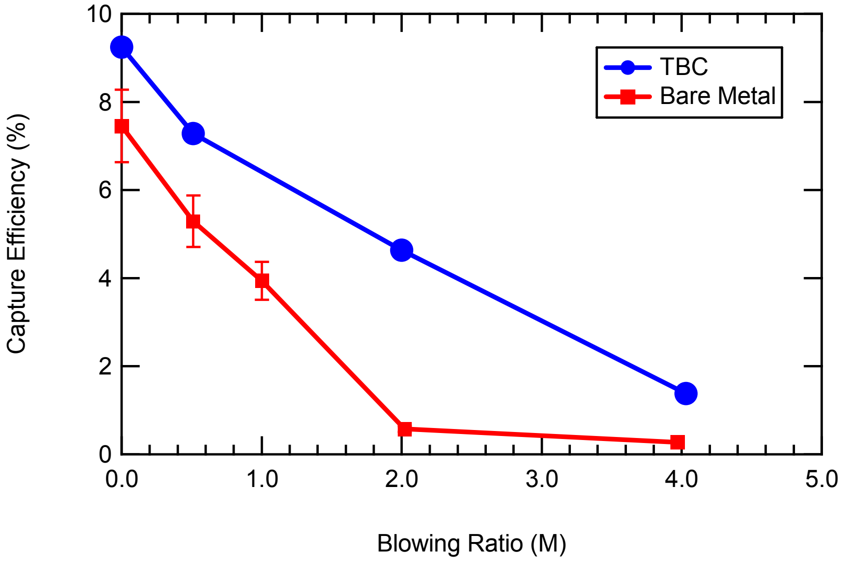

Figure 5.15 Capture efficiency measured for M3 and TBC coupons with 3 holes and s/d=4.5 as a function of blowing ratio

Figure 5.16 shows a comparison of spanwise surface temperatures at a location y/d = 2.0 downstream of the cooling holes made for the M4 and TBC tests at M = 2.0 and the same density ratio. The average surface temperature of the TBC coupon was observed to be 76 K higher than that of the metal coupon, which was partially responsible for the higher capture efficiency. This measured result of increased temperature for the TBC contradicts the modeling results of Na et al. (2007), who reported that the surface temperature decreased when the TBC was added. This may have been due to the values of thermal conductivity used in the modeling study by Na and coworkers. Due to the significance of surface temperature on deposition, the data shown here illustrate that the

TBC thermal resistance and structure is likely responsible for the increased deposition in this case. The temperature valley formed by coolant at the M4 surface was not as apparent as for the TBC coupon temperature data. This suggests that the coolant in the M = 2.0 case has a more significant effect on the TBC surface temperature pattern than on the bare metal surface, which is likely related to the difference in thermal conductivity.

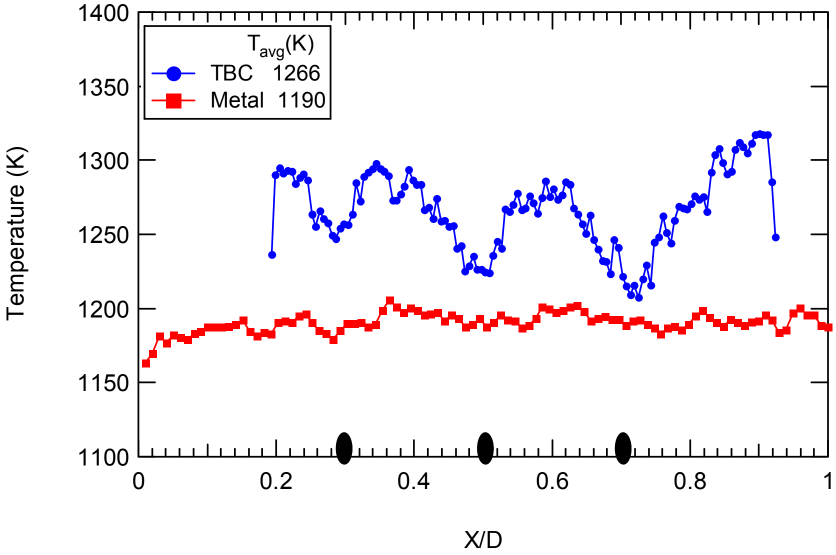

Figure 5.16 Spanwise distribution of temperature at y/d=2.0 for the metal coupon M4 and TBC coupon with 3 holes, s/d=4.5, and M=2.0

Deposit thickness maps are shown in the Figure 5.17 for the M = 4.0 cases with and without TBC. Figure 5.17a was obtained by scanning the entire TBC surface with CMM. A Hommel profilometer was used to measure deposit thickness in the region downstream of film cooling holes for the M4 test, as shown in Figure 5.17b. As can be seen in these figures, there was a much thicker deposit on the TBC coupon than on M4 coupon in these M = 4.0 tests. Deposits formed mostly upstream of the holes on the TBC coupon. The difference in height of the surface between the highest peak and lowest point was about 3.5 mm for the TBC coupon. However, little deposition appeared in the coolant flow path area, indicating that the high blowing ratio cooled the entire downstream surface of the coupon effectively. In the metal coupon scan three troughs can be distinguished in the section downstream of the holes. The height of the ridges was only about 10 μm above the troughs. No distinct deposit variations were observed at locations upstream of the film cooling holes, which was consistent with the deposit photo previously shown in Figure 5.13. The deposit thickness in the area downstream of holes for the TBC coupon was not measured.

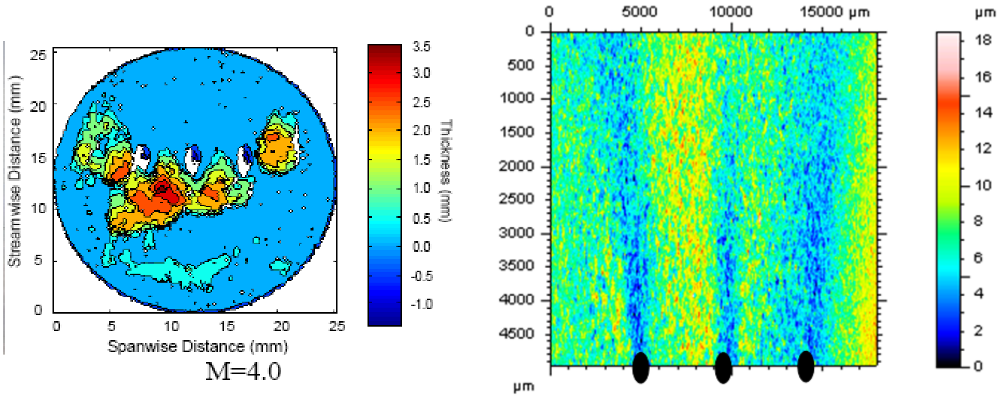

a) b)

Figure 5.17 Deposit thickness variation map at M=4.0 for s/d = 4.5. a) TBC coupon, b) bare metal coupon (M4) (3 holes blowing)

5.3 Hole Spacing

The configuration of coupons and testing condition are shown in the Table 5-3. A series of tests were performed to examine the effect of hole spacing on deposition characteristics. Test results from a TBC coupon with s/d=2.25 and s/d=4.5 are described first, followed by results with bare metal coupons at an interim hole spacing (3.375d).

Comparisons between the data from the TBC coupons and the bare metal coupons are also presented.

Table 5-3. Coupon configuration and testing conditions for the study of hole spacing

Case	Holes	Hole geometry	Hole size (d)	Hole spacing	Impingement angle(α)	Blowing ratio	Testing time
TBC	5	cylindrical	1.0mm	2.25d	45°	2.0	1 hr
TBC	3	cylindrical	1.0mm	4.5d	45°	2.0	1 hr
TBC	3	cylindrical	1.0mm	2.25d	45°	2.0	1 hr
M3	3	cylindrical	1.0mm	3.4d	45°	0,0.5,1.0,2.0	1 hr

5.3.1 TBC Coupon with s/d=2.25 and s/d=4.5

The initial TBC coupons used in this series of tests had five 1 mm holes spaced 2.25d between hole centers. To investigate the effects of spanwise pitch-to-diameter ratio on deposition, two additional tests were conducted. In one test the second and fourth holes were plugged with insulation, giving a pitch-to-diameter ratio of 4.5 for the three open holes. The other test was performed on the coupon with the first and fifth holes blocked, leaving the middle three holes open and s/d = 2.25. The deposit patterns on the TBC coupon with s/d = 2.25 and s/d = 4.5 at constant M = 2.0 are shown in Figure 5.18. There was no pronounced deposit variation appearing in the downstream region of the film cooling holes for 5 holes and s/d = 2.25 (Figure 5.18a). The deposit was evenly distributed across the upstream section of the cooling with the exception of two small blocks of deposit. For the coupon with wide spacing (s/d = 4.5) shown in Figure 5.18b, three distinct furrows appeared in the area between coolant passages. For the third case (Figure 5.18c), a hole was blocked by the deposit, and deposit troughs were not observed.

Quantitative measurements for the third case were not possible since the deposit stuck so well to the coupon holder. However, these figures show qualitatively that the amount of deposition was similar for Figure 5.18b and Figure 5.18c. One reason for the enhanced deposition on the 3-hole coupons is that for the same blowing ratio, the cooling flow rate was 5/3 higher in the 5-hole test than in the 3-hole test. The enhanced cooling flow rate resulted in a lower surface temperature due to the coolant impingement on the backside of the coupon.

(a) (b) (c)

Figure 5.18 Variation of deposit patterns on the TBC coupon at M=2.0 with (a) s/d=2.25 (5 holes), (b) s/d=4.5 (3 holes), (c) s/d=2.25 (3 holes)

The lateral temperature distributions at a location of y/d = 2.5 from the downstream edge of the film hole are shown in Figure 5.19 for these three hole spacing tests. The laterally-averaged surface temperature is plotted versus the normalized spanwise distance. The three valleys observed for case (b) indicate the coolant passages. The temperature distribution for case (a) shows uniform cooling coverage, with no distinct pattern of temperature variation downstream of the area between cooling holes.

In case c, coolant from the three middle holes lowered the surface temperature in the central area. The spanwise temperature at this location increased from 1193 K for s/d = 2.25 to 1265 K for s/d = 4.5. For cases (b) and (c), the spanwise-averaged temperature was almost the same.

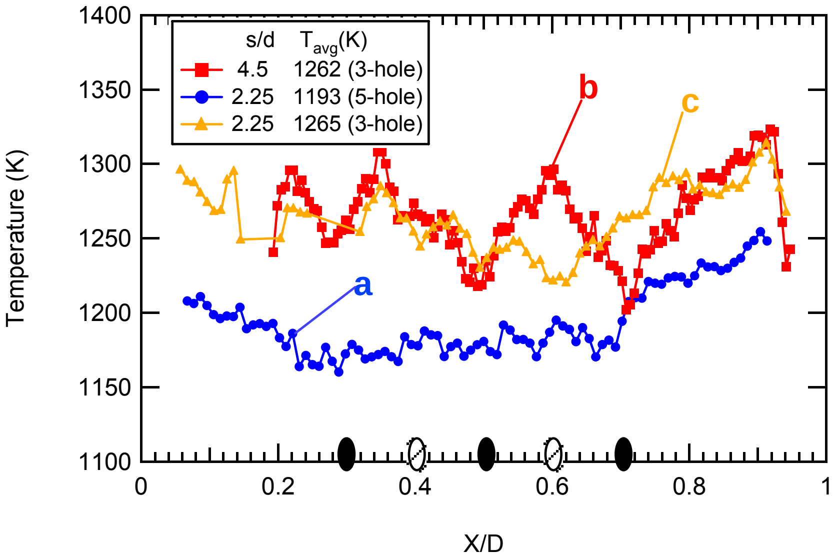

Figure 5.19 Spanwise distribution of surface temperature for TBC coupon at y/d=2.5 and M=2.0 for s/d=2.25(5 holes), s/d=4.5(3 holes), and s/d=2.25 (middle 3 holes)

5.3.2 Bare Metal Coupon with s/d = 3.375 and 4.5 (M3 and M4)

The same testing conditions used on the coupon with s/d = 4.5 were applied to the coupon with s/d = 3.375 to provide insight into the effect of hole spacing on deposition (with 3 holes).

5.3.2.1 Surface deposit pattern

Figure 5.20 shows the deposit pattern at blowing ratios from M = 0 to M = 2.0 for s/d = 3.375. The coolant path downstream of the holes can be distinguished by the color contrast. When Figure 5.20 is compared with Figure 5.13, it can be seen that the coolant flow in the case of s/d = 3.375 was more aligned with the bulk flow streamlines than the case of s/d = 4.5 at the blowing ratio of M = 2.0. The deposit patterns were similar for both hole spacing configurations.

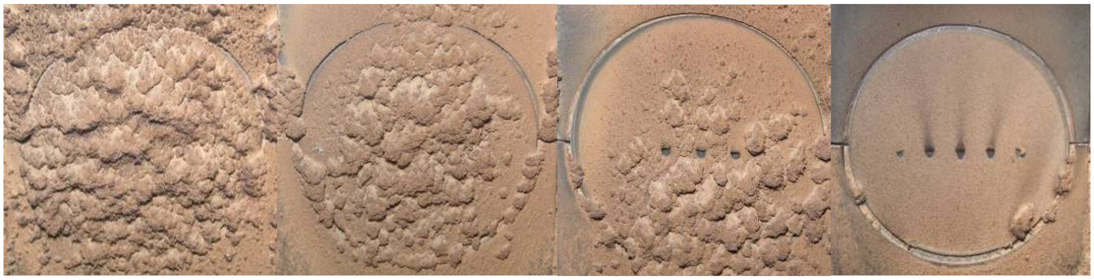
M=0.0 M=0.5 M=1.0 M=2.0

Figure 5.20 Variation of deposit patterns on the surface of coupon M3 with 3 holes, s/d = 3.375d, and M from M=0 to M=2.0

The measured capture efficiencies at different blowing ratios for the two different hole spacing cases are shown in Figure 5.21. As shown earlier, the trend is that capture efficiency decreased with increased blowing ratio. The capture efficiency for s/d = 3.375 at M = 0 and 2.0 was close to that for s/d = 4.5, whereas for the M = 0.5 and 1.0 cases, the coupon with a close hole spacing had a lower capture efficiency than that of the coupon with a large hole spacing. The capture efficiencies for the s/d = 3.375 case were 1.5% lower on an absolute scale for blowing ratios between 0.5 and 1.0 than in the s/d = 4.5 case. This was a difference of 33-60% on a relative scale. This difference illustrates that the effect of hole spacing on particle deposition is correlated with other factors, such as blowing ratio. One replicate test was performed at each of two blowing ratios (M=0.5 and 1.0) for each hole spacing configuration. The upper and lower 95% confidence limits were generated based on the sample mean and deviation. The mean and standard deviation were calculated from the two tests at each condition. It is assumed that the replicated tests are systematice throughout. Therefore, the error bar was applied to all test results, as shown in Figure 5.21. These data indicate that the confidence levels were fairly narrow for the capture efficiency (within 9% of the mean).

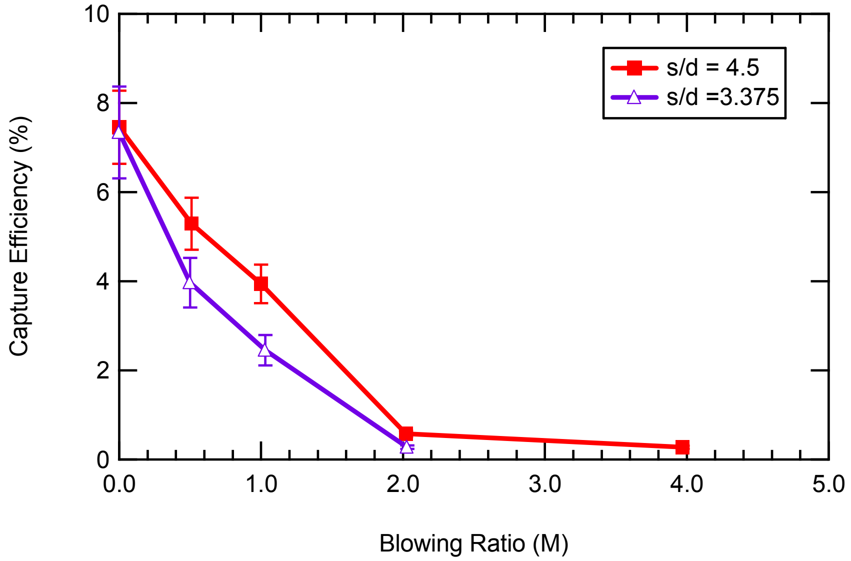

Figure 5.21 Capture efficiency at various blowing ratios for bare metal coupons with 3 holes, s/d = 3.375(M3) and 4.5 (M4)

5.3.2.2 Thickness of deposit

The roughness characteristics of deposits obtained for the two different hole spacing test series for different blowing ratios are summarized in Figure 5.22. Roughness data at M = 2.0 were obtained with the contact profilometer, while data for M < 2.0 were from the optical CMM technique. Because the deposit flaked off, the results at M = 1.0 and M = 0.5 shown in this figure were acquired by scanning the deposit recovered from deposit pieces collected after the test, reassembled on the basis of photos. The roughness data from the no-cooling case (M = 0) were shared for both hole spacing series. Both coupons show a monotonic decrease in roughness parameters Ra and Rt with elevated blowing ratio, with the most substantial decrease occurring at blowing ratios from 0.5 to 1.0. The roughness statistics change the most for the smaller hole spacing case between M=0.5 and M=1.0. However, the roughness statistics for the s/d=3.375 case are lower than for the s/d=4.5 case, especially at high blowing ratios. The close-hole spacing enhances the interaction of neighboring jets and improves coolant coverage, resulting in a low temperature region and reduced amounts of deposit. This influence of jet interaction is more significant at high blowing ratios.

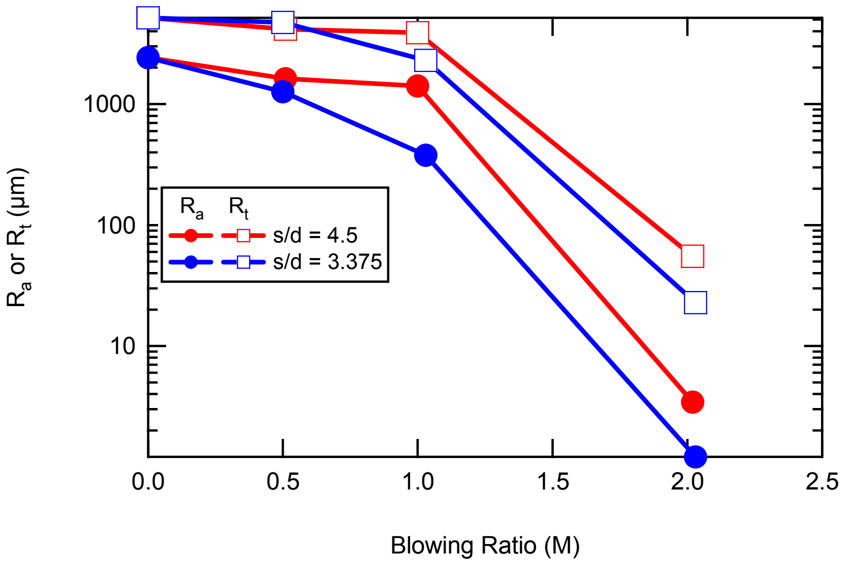

Figure 5.22 Roughness statistics of deposit on bare metal coupon with 3 holes and varying hole spacing in the downstream region

5.3.2.3 Surface temperatures

Surface temperature maps at three different blowing ratios for the bare metal coupons with two different hole spacings (M3 series and M4 series) after 20 minutes are shown in Figure 5.23. This time corresponds to the beginning stages of deposit formation.

The effect of blowing ratio is very apparent in the average temperature of the surface. The increased backside cooling from the increased cooling flow rate at higher blowing ratios is effective at lowering the average surface temperature. The coolant flow paths in these experiments were visible more for the blowing ratios of 1.0 and 2.0. The difference in temperature between the flow paths and the gaps between the flow paths was most apparent for blowing ratios of 1.0. Spanwise temperature profiles for the different hole spacing cases are shown in Figure 5.24 at the location of $y = 2.0d$ for $M = 1.0$. The average spanwise temperature for the close-hole spacing case was 1241 K, slightly less than the average temperature of 1257 K for the large hole spacing case. The maximum peak-to-valley temperature difference for the left-hand flow path was quite pronounced for the $s/d = 4.5$ case, but similar to the $s/d = 3.375$ case for the middle and right-hand flow paths. This seeming discrepancy was due to small ridge of deposit that formed between the flow paths in the $s/d = 4.5$ case (Figure 5.23e), and the surface temperature increased in that local area due to increased deposit height.

The surface temperature in these experiments is influenced by the convective heat flux from the gases impinging on the front side of the coupon, the flow rate and pathway of the gas passing through the film cooling holes, the backside impingement cooling before the coolant gases flow through the cooling holes, conduction to the coupon holder, and radiation to the surroundings. As blowing ratio is increased, the competition between the convection heating and impingement and film cooling shifts more towards cooling, and the average surface temperature decreases. At the blowing ratio of 2.0, the backside impingement cooling seems to become quite important, since the coolant flow paths from the holes are less visible and the peak-to-valley temperature difference is small.

s/d = 3.375

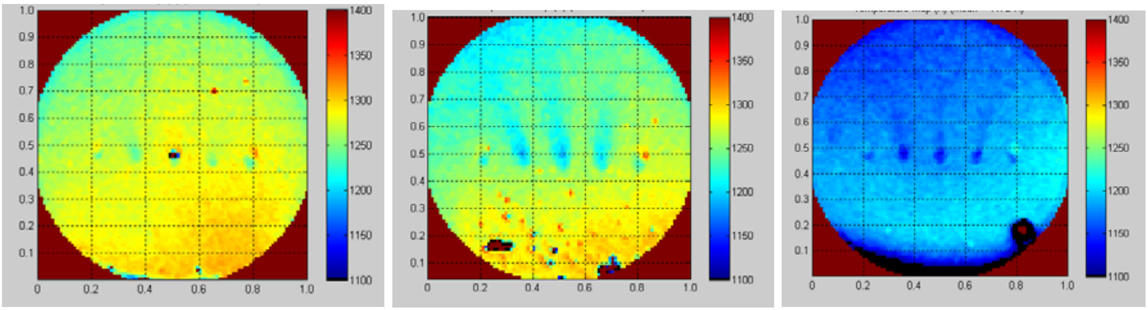

(a) M = 0.5 (b) M = 1.0 (c) M = 2.0

s/d = 4.5

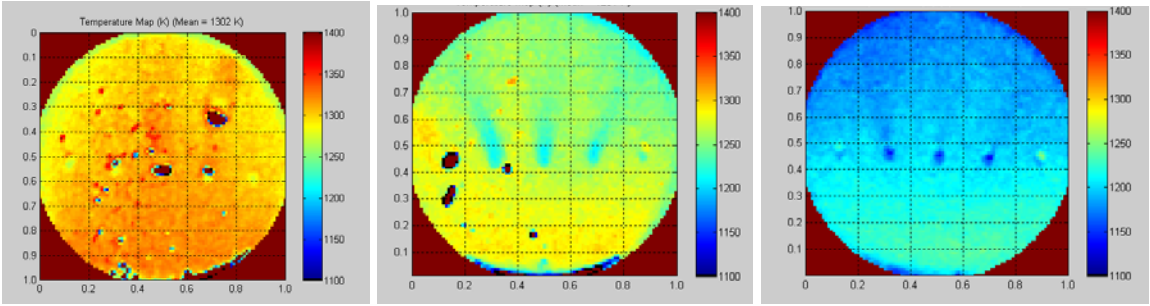

(d) M = 0.5 (e) M = 1.0 (f) M = 2.0

Figure 5.23 Surface temperature maps of metal coupons after 20 minutes deposition for different blowing ratios and hole spacings. Color bar indicates surface temperature in Kelvin. Flow is upward in these figures (3 holes blowing)

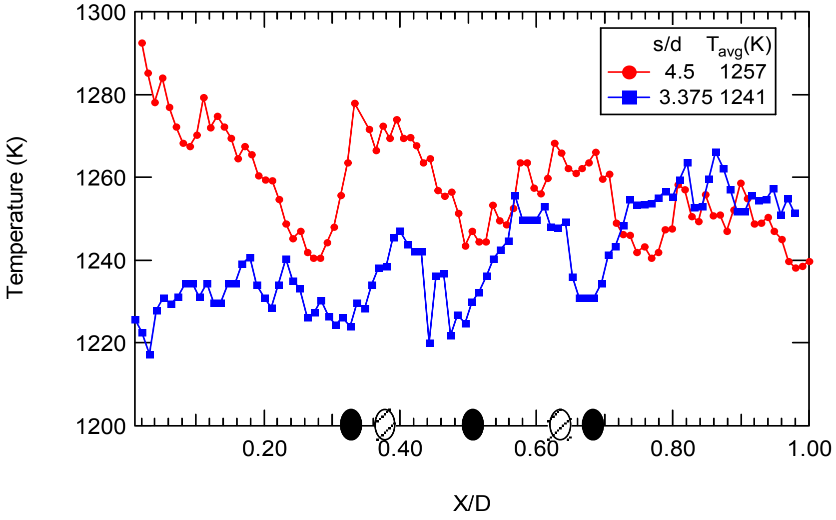

Figure 5.24 Spanwise temperature distribution at y/d = 2.0 downstream of the cooing holes for M = 1 and with s/d=3.375 (cross-hatched holes) and 4.5 (solid holes) respectively (3 holes blowing)

The centerline film effectiveness η_{ce} in the streamwise direction downstream from the middle hole was also examined quantitatively. η_{ce} is defined as

$$\eta_{ce} = \frac{T_{\inf} - T_s}{T_{\inf} - T_c} \tag{5-1}$$

where T_c is the coolant temperature at the entry to film holes, T_s is the wall surface temperature, and T_{inf} is the gas temperature. Since the gas temperature above the holes is not known, T_{inf} was replaced by the wall surface temperature from the M=0 case. The values of η_{ce} for s/d = 3.37 and 4.5 are shown in Figure 5.25 for three different blowing ratios. The streamwise distance from the exit of the center hole was normalized by the hole diameter d.

Figure 5.25 shows that η_{ce} increased with increasing blowing ratio for both hole spacing cases. These test results are compared with the literature (Yuen and Martinez-Botas, 2005). The effectiveness factor defined in the literature is the adiabatic film cooling effectiveness, as opposed to the definition used here based on the local measured surface temperature with no cooling (Equation 5-1). The hole spacing for the Yuan and Martinez-Botas data was 3d. Figure 5.25a shows that the maxium effectiveness reported by Yuan and Martinez-Botas occurred at M= 0.6. The lower effectivness at high blowing ratios was caused by the occurrence of coolant lift-off after exiting from the cooling holes. The contradiction of the current work with the literature may be due to the 45 degree freestream impingment angle in this experiment.

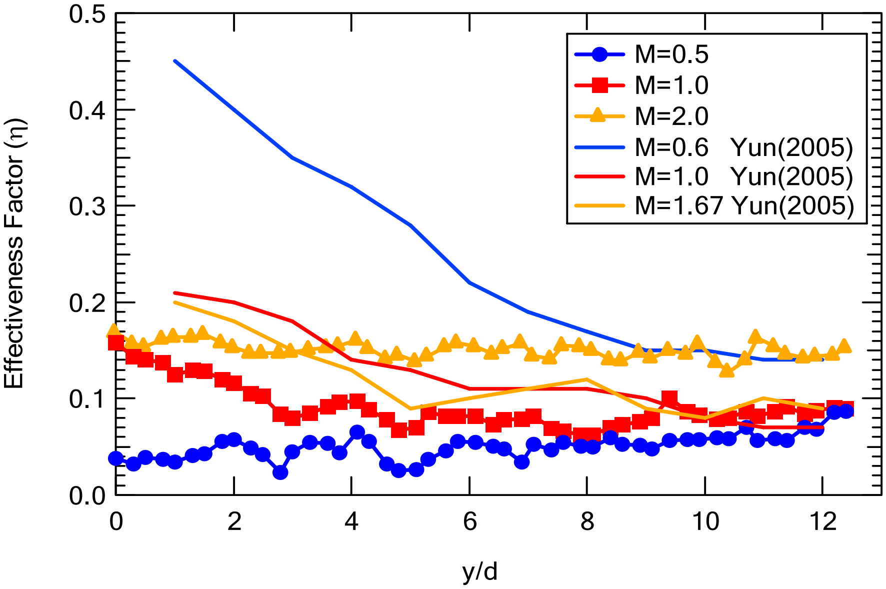

(a)

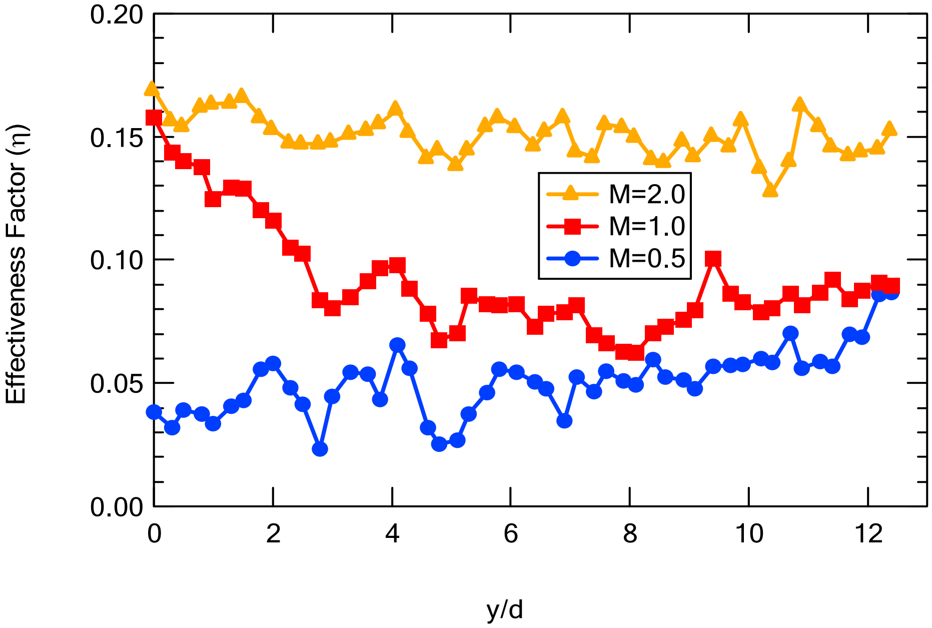

(b)

Figure 5.25 Streamwise surface temperature distributions along the centerline downstream of the middle hole at different blowing ratios. (a) s/d = 3.375, (b) s/d = 4.5d (3 holes blowing)

The value of η_{ce} for s/d = 3.37 was lower than that for s/d = 4.5d at each blowing ratio. Referring to the case of s/d = 3.375, η_{ce} decreased in the streamwise direction for M = 1.0 and 2.0, but at M = 0.5 values of ηce increase. For s/d = 4.5 and M = 1.0, the η_{ce} curve was similar to that for s/d = 3.375, decreasing along the centerline in the streamwise direction. At M = 0.5 and 2.0, the temperature curve appeared relatively flat, inconsistent with previously reported results obtained in low-temperature film cooling tests (Walters and Leylek, 1996; Silieti et al., 2005). It was expected that the η_{ce} should increase in the streamwise direction along the centerline. The heat transfer occurring on the component surface depends on multiple factors such as coolant flow momentum, blowing ratio, backside cooling, and mainstream flow properties. The similarity of these centerline profiles for different hole spacings, along with the relatively-small difference in spanwise temperature profiles (Figure 5.24) indicates that the backside cooling may be almost as significant as the film cooling in these tests.

5.4 Effect of Particle Size

The smaller particle size distribution (d_{avg} = 4 μm) is more representative of what might be expected to pass through a syngas filter system than the larger size distribution (d_{avg} = 13.4 μm). The tests to study the effect of particle size on sample surface and ash deposition were performed on the coupon M3 and M4 at the different blowing ratios. Conditions used for the small particle tests were the same as the conditions in the large particle test (See Table 5-4). The density ratio for these tests ranged from 1.8 to 2.2. The testing time was 1 hour and the particle loading was 160 ppmw.

Table 5-4. Coupon configurations and test conditions for the small particle tests

Case	# of holes	Mean Particle size(um)	Hole geometry	Hole size (d)	Hole spacing	Impingement angle(α)	Blowing ratio	Testing time
M3	3	4	cylindrical	1.0 mm	3.4d	45°	2.0	1 hr
M4	3	4			4.5d	45°	0,0.5,1.0,2.0	1 hr

5.4.1 Surface Deposit Pattern

Deposit patterns obtained for four tests conducted with small particles and blowing ratios from 0 to 2.0 are shown in Figure 5.26. The deposits from the small particles stuck to the surface more tenaciously after combustor shut down than did the larger particles, meaning that less flaking occurred. At M=2.0, the deposit was concentrated in the upstream region of the coupon before the cooling holes, where particles impacted first. The amount of deposit observed with small particles was slightly larger than observed with the larger particles. At M=1.0, three distinct furrows appeared downstream of the holes on the sample tested, and formed a region of dramatic spatial variation of deposition in this region. No such distinct furrows were apparent for the large particle tests, as seen in the Figure 5.26 for M=1.0. The deposit valley indicates the coolant path. The deposit appearance for these small particle tests shows local flow directions that deviated from the main flow direction (e.g., see circled area for M = 0.5). The flow directions could not be discerned from the local deposit appearance for the large particle tests. The coolant flow paths also show this “fanning” effect. Deposits upstream of the cooling holes were evenly distributed. For blowing ratios of 0.5 or less, the cooling holes were blocked after the first twenty minutes, after which deposits began to form and spread over the entire sample surface. The deposits from the small particles appeared more smooth (i.e., less jagged) than in the large particle tests.

The capture efficiencies obtained with s/d=3.375 for small and large particles are shown in Figure 5.27. At M=2.0, the capture efficiency for small particles was 0.64%, similar to that for the large particles. At blowing ratios less than 2.0, the capture efficiencies for small particles were smaller than for large particles. The capture efficiency for large particles increases significantly with the reduction of blowing ratio. In the test without coolant, the capture efficiency for small particles was 3.0 %, much less than the value of 7.3% observed for large particles. The capture efficiency of the large particles decreased by a factor of 13 when the blowing ratio was increased from 0.5 to 2.0, but only a factor of 2.6 for the small particles. Also shown in Figure 5.27 are earlier data by Jensen et al. (2005) using the same two sizes of particles with M = 0 but in a 4-hr test and 10-13 grams of particulate. The agreement between the two sets of data taken several years apart illustrates the robustness of the testing technique, even with very different test durations and loading. At M=2.0, the capture efficiency from small particles was slightly lower than that from large particles, although this may be within experimental error. However, the blowing ratio for the small particle case was slightly less than 2.0, and the decreased surface temperature at the higher blowing ratio may have reduced deposition for the large particle case. These results indicate that the large particles generally have a higher propensity to deposit on the surface than the smaller particles under the same test conditions. The larger particles are more sensitive to the blowing ratio. The blowing ratio influences the surface temperature in these tests, with higher surface temperatures at lower blowing ratios. The implication is that the large particles are more inclined to deposit above some critical surface temperature, which is influenced by the blowing ratio.

M=0.0 M=0.5 M=1.0 M=2.0 M=1.0(Large)

Figure 5.26 Variation of deposit patterns from fine particles and large particle (right side) on the M3 coupon surface with hole spacing 3.375d at blowing ratios from M = 0 to M = 2.0 (holes 1 & 5 blocked)

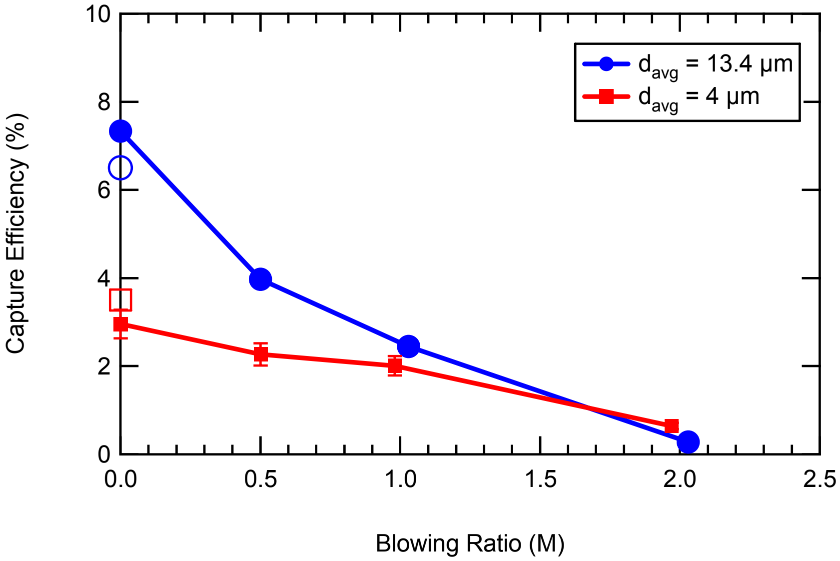

Figure 5.27 Capture efficiency observed for the M3 bare metal coupon (s/d = 3.375) at various blowing ratios for average particle sizes of 4 μm and 13.4 μm. Open symbols are from experiments by Jensen et al. (2005) using the same two sizes of particles with M = 0 but in a 4-hr test and 10-13 grams of particulate

5.4.2 Thickness of Deposit

Thickness maps obtained from deposits obtained in the small particle tests at different blowing ratios are shown in Figure 5.28. Deposit flaking occurred for the large deposit cases after the specimens were removed from the test facility. The separated deposits were reconstructed based on the pictures taken before the CMM measurement. Three distinct troughs appeared in the region downstream film holes at M=2.0 and 1.0. The deposit was very thin at M=2.0 due to the combined influence of internal and external cooling. For the case of M=0.5, particles deposited initially in the region close to holes and eventually covered the hole. Figure 5.29 presents the roughness statistics for the deposit in the region downstream of the holes. At M=2.0, Ra for small particle is 1.12 µm, which was similar to that observed for the large particles. As the blowing ratio decreased, Ra and Rt for both particle sizes increased two orders of magnitude and reached a level value at M=0.5. At low blowing ratios, the roughness of deposit formed by large particles was larger than for the small particles, in good agreement with the trend in capture efficiency (see Figure 5.27).

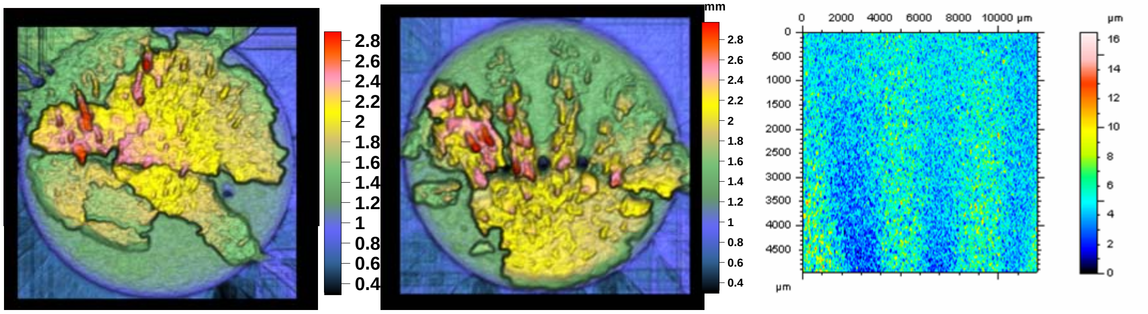

M=0.5 M=1.0 M=2.0

Figure 5.28 Surface maps of deposit height observed for fine particle tests on a M3 bare metal coupon with s/d = 3.375 at blowing ratios ranging from 0.5 to 2.0 (holes 1 & 5 blocked)

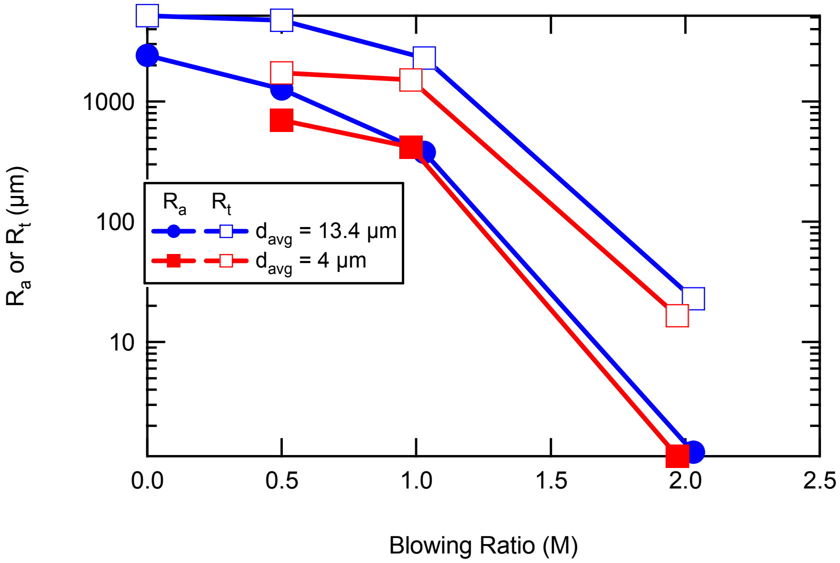

Figure 5.29 Roughness statistics of deposits in the region downstream of the cooling holes for tests with two particle sizes on the M3 bare metal coupon s/d = 3.375 (holes 1 & 5 blocked)

The small particles were also used in a test on the coupon with s/d = 4.5 at a blowing ratio of 2.0. The deposit pattern and thickness map for this test are presented in Figure 5.30. Due to a smaller degree of coolant coverage downstream of the film holes, even at M = 2.0, the small particles formed three apparent furrows. The capture efficiency for this case was 0.95%, which is larger than the capture efficiency of 0.58% for the larger particles with s/d = 4.5. The Ra and Rt measured for this test were 137.6 μm and 904.2 μm, respectively.

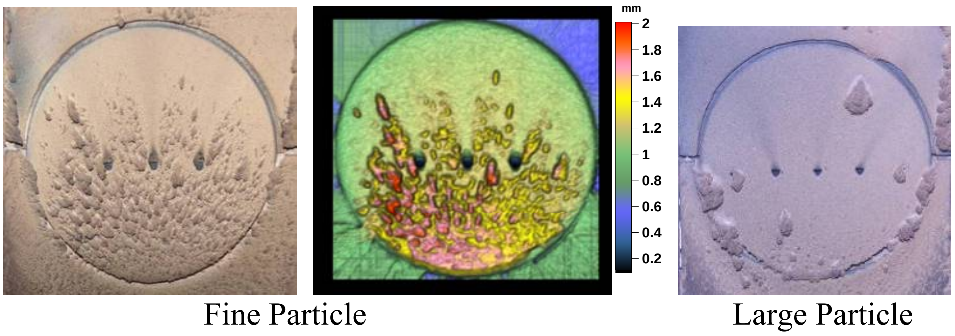

Figure 5.30 Surface maps of deposit height from fine particle (two left panels) and large particle (right) for bare metal coupons with s/d = 4.5(M4) at M = 2.0

5.5 Trench Configuration

For the trench configuration M5, several impingement angles were tested at a blowing ratio of 2.0 to determine a suitable value for trench studies. Subsequently, the effect of trench configuration on deposition was tested at blowing ratios from 0.5 to 2.0 by comparing M5 with the base case M6. The test matrix is shown in Table 5.5. Test data include deposit patterns, temperature distributions, capture efficiencies and deposit roughness analyses.

Table 5-5. Coupon configuration and testing conditions for the study of trench configuration

Case	# of holes	Hole geometry	Hole size (d)	Hole spacing	Impingement angle(α)	Trench	Blowing ratio	Testing time
M5	3	cylindrical w/trench	1.0	2.25d	45°,30°,15°	Width=2.5d Depth=0.75d Length=16d	2.0	1 hr
M5	3	cylindrical w/trench	1.0	2.25d	30°	Width=2.5d Depth=0.75d Length=16d	0.5,1.0,2.0	1 hr
M6	3	cylindrical	1.0	2.25d	30°	NO	0.5,1.0,2.0	1 hr

5.5.1 Effect of Impingement Angle

Most previous tests in the TADF have been performed with an impingement angle of 45°, since this seemed to provide suitable deposits in a reasonable amount of time. However, trench configurations were originally conceived for vane endwall cooling applications. Thus, lower impingement angles were considered to be more relevant. A series of three tests were performed with impingement angles of 45°, 30° and 15° at a blowing ratio of 2.0 and density ratio of 2.1, using the coupon M6 listed in Figure 5.5. The second and fourth holes were blocked by ceramic material to obtain a hole spacing of

4.5d. The impingement angle is defined in Figure 5.31d to be the angle between the centerline of combustor tube and the line parallel to coupon surface (0° being parallel). Deposition patterns are shown in Figure 5.31 for these tests. At an impingement angle of 45°, the coupon surface was entirely covered by deposit, and the film cooling holes and trench were blocked. Since deposition has been shown to increase at lower blowing ratios, further tests at 45° for lower blowing ratios would likely obscure the effect of the trench and other parameters. Therefore, deposition tests were conducted at the other two shallower impingement angles. At an angle of 15°, no significant deposit was observed on the surface or inside the trench (Figure 5.31c) and the measured capture efficiency was 0.079%. At an angle of 30°, most of the deposition was concentrated in the region upstream of the trench. The slightly brighter color appearing in the area downstream of the trench indicated the coolant paths. It can be seen upon close inspection in Figure 5.31b that the coolant flow path extended not only directly downstream of the film cooling holes, but downstream of the blocked holes as well. This suggests that the coolant ejected from the holes impacted against the trench wall and spread in the trench, resulting in the better lateral coolant distribution downstream of the trench. Some deposit developed in the trench between the downstream grooves at the hole exits (see arrow in Figure 5.31b). Once deposition starts in a region, the deposition rate increased in that region due to increased deposit surface temperature.

The variation of capture efficiency versus impingement angle is shown in Figure 5.32, indicating that the capture efficiency dramatically increased when the impingement angle increased from 15° to 45°. At an angle of 45°, the capture efficiency reached the value as high as 3.39%. The red square spot indicates the capture efficiency of 0.6%

obtained from a test at M=2.0 on a coupon without a trench, which was much less than that from a coupon with a trench. Deposition pattern development as a function of time is presented in Figure 5.33 for the 45° impingement angle test for M = 2, illustrating the significant role of the trench configuration. In the initial 10 minutes, some deposit was formed between the grooves in the downstream edge of the trench (like in Figure 5.31b). After 20 minutes, deposition was observed along the entire downstream wall of the trench, which effectively changed the shape of the trench. Eventually, the deposits almost bridged across the trench (~40 min), which prevented the coolant from spreading across the trench and deteriorated the local heat transfer downstream of the trench. The deposit within the trench accumulated until the holes were blocked (~50 min) and film cooling was disabled. A massive deposit accumulated in the region downstream of the trench during subsequent testing times. It is noteworthy that the deposit mass in the vicinity of the two side edges of the trench was much less than any other region. It seems that the coolant ejected from the holes was blocked by the deposit and leaked out into the sides of the trench, resulting in a lower temperature area and mitigating the deposition in that region.

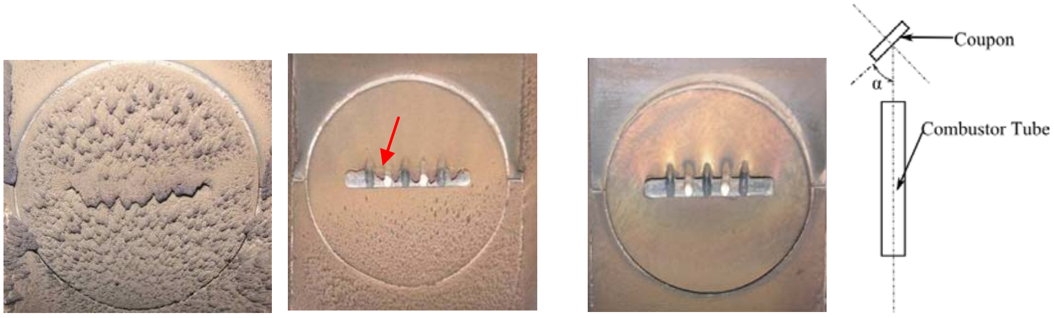

(a) (b) (c) (d)

Figure 5.31 Deposit patterns from fine particles on the trench coupon (M5) for M = 2.0 for various impingement angles (a) α=45°; (b) α=30°; (c) α=15°; (d) schematic of impingement angle (s/d=4.5, holes 2 & 4 blocked)

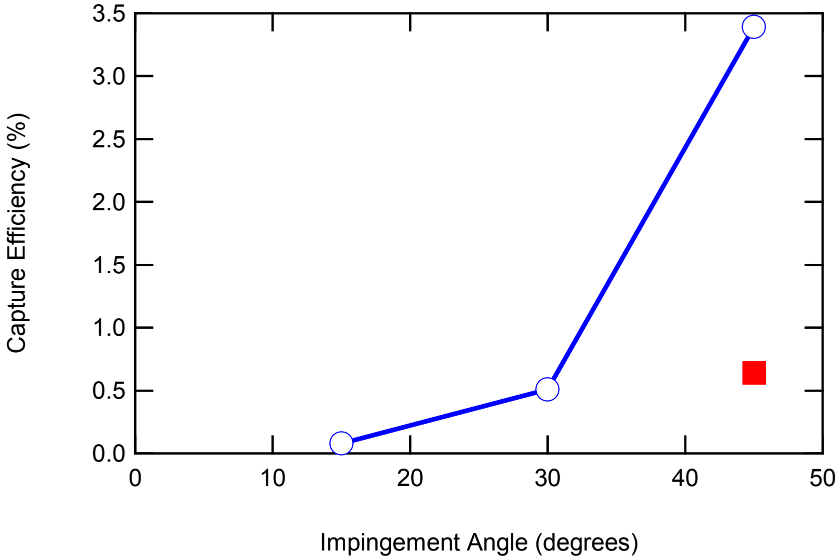

Figure 5.32 Capture efficiency of the bare metal trench coupon (M5, open circles) and baseline coupon without trench (M6, solid square) at M = 2.0 (3 holes blowing) for various impingement angles

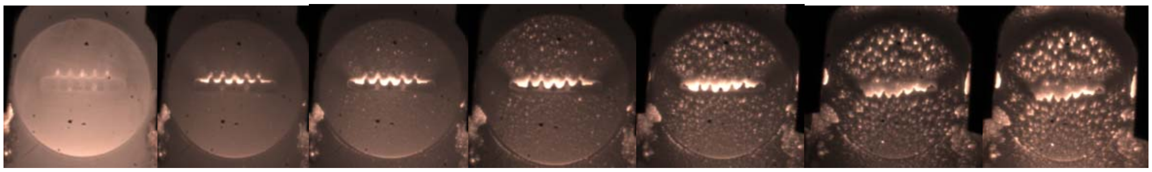

Figure 5.33 Deposit development versus time at α=45° and M=2.0 with M5 trench coupon (3.holes blowing)

Surface temperature maps for the deposition tests at the three different impingement angles are shown in Figure 5.34 taken before deposition started. For the 45° impingement angle case, the spatial temperature in the region upstream the trench was higher than the other two cases. The coolant flow paths were not clearly visible at the current testing blowing ratio, which may be due to reduced jet exit momentum caused by the trench. It is likely that at α = 45° the mainstream gas penetrated the trench upstream of the cooling hole, which mixed with the coolant and resulted in failure of a cooling film to expand laterally over the surface. For α = 30°, the entire surface temperature was lower than for the 45° case, especially in the region downstream of the trench. This indicates that at α = 30° the trench was effective at distributing the coolant flow in the spanwise direction and providing good film cooling downstream of the trench. This would also indicate that the upstream wall blocked the mainstream flow penetration into the trench at this angle. For the 15° case, the impingement angle was the shallowest, and the coolant paths were clearly observed downstream of the trench where the color was deep blue compared with the surrounding area. These data indicate minimal penetration of the main gas stream into the trench at this shallow angle. Since too much deposition was observed at α = 45°, and minimal deposition was observed in the 1-hr tests at α = 15°, all subsequent tests to show trench effects were performed at α = 30°.

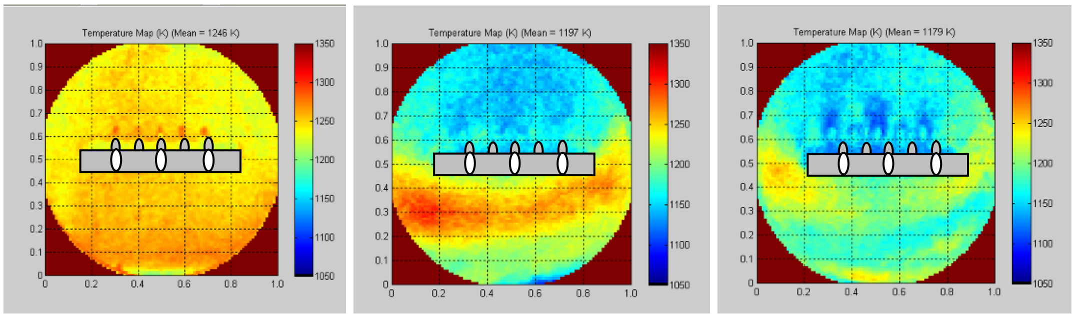

(a) (b) (c)

Figure 5.34 Surface temperature maps after approximately10 min for M = 2.0 at different impingement angles (a) α=45°; (b) α=30°; (c) α=15°

5.5.2 Bare Metal Coupon with Trench Configuration

To study the effect of the trench on particulate deposition, two sets of experiments were designed and performed. The first set of tests was carried out on the coupon M6, which had no trench and was treated as the baseline case. The other set was performed on the coupon M5 with a trench. The second and fourth holes were blocked for both cases to obtain a hole spacing of 4.5d. Figure 5.35 shows the post-test deposition pattern at blowing ratios of 0.5, 1.0 and 2.0. At M=0.5, deposits were visible in the region downstream of the film holes for both test coupons. Some deposit was built up at the exit of holes and reduced the cross sectional area of coolant flow on coupon M6. On coupon M5, deposits formed on the downstream trench wall between the exit grooves and extended upstream to almost bridge the trench, significantly changing the trench geometry configuration (in a manner similar to Figure 5.31b). The coolant flow path was not evident for either case at M = 0.5. At M = 1.0, seven coolant streaks were observed downstream of the trench for case M5, and the length of the coolant paths downstream were much longer than for case M6. The amount of deposit observed in the area circled in red for case M5 was less than for case M6. It seems that the coolant ejected from holes was mixed inside the trench and diffused across the surface downstream along the entire trench length. At M=2.0, due to the increased momentum ratio, the coolant paths are visible for case M6. Very little deposition occurred downstream of the cooling holes for M = 2.0; most deposition occurred upstream of the film holes for both of cases. For case M5, more deposit on the downstream wall of the trench was observed at M=2.0 than at M=1.0. This suggests that the increase of blowing ratio expedited the escape of coolant from the trench and shortened the time the coolant resided inside the trench to cool down the wall.

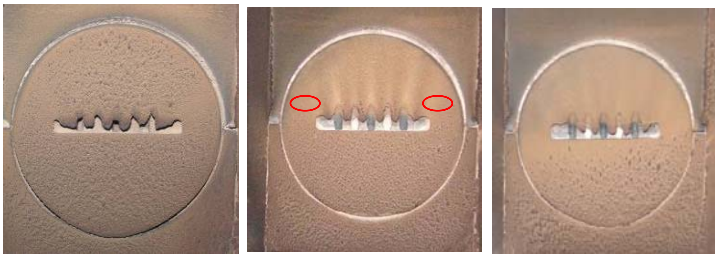

a) M=0.5 b) M=1.0 c) M=2.0

Case M5 (with a trench)

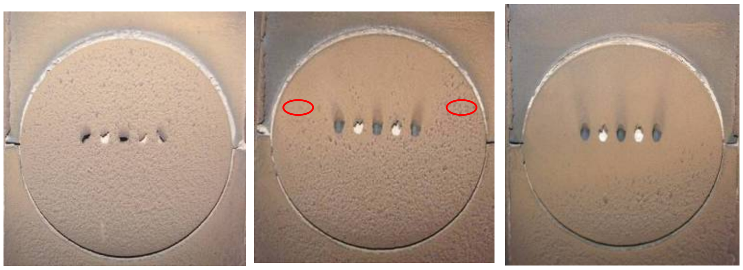

a) M=0.5 b) M=1.0 c) M=2.0

Case M6 (without a trench)

Figure 5.35 Deposit patterns from fine particle on the coupon with and without a trench configuration (M5 and M6 respectively) for M = 0.5 to 2.0 and α = 30° (3 holes blowing)

Figure 5.36 shows the impact of the trench on particulate capture efficiency. As indicated in the Introduction, recent literature indicates that cylindrical holes embedded in a transverse trench perform better than cylindrical holes with respect to heat transfer and film cooling effectiveness. Based on these findings, it was expected that the particulate capture efficiency obtained from the coupon with a trench should be lower than the result from the sample without a trench. However, the test results indicated that at M=0.5 and 2.0, the capture efficiency for case M5 was slightly higher than that for case M6. The capture efficiency for M6 was somewhat lower than for case M5 at M = 1.0. Multiple points in this figure represent repeat tests, and indicate a measure of the repeatability for these experiments. The differences in collection efficiency caused by the trench may be within the margin of error for these experiments. The development of the deposit as a function of time for the M5 coupon is shown in Figure 5.37. After 20 minutes, the bright color located in the trench wall in the image indicated the commencement of deposition. At later times, the brightness increased in the trench area, indicating deposit growth and increased surface temperature. These photos suggest that for the trench configuration, deposition started in the trench area. Deposition started upstream of the cooling holes for the M6 case. It appears two competing effects are being observed with the trench configuration. The increased cooling effectiveness of the trench configuration was a driving force for lower amounts of deposition downstream of the trench. In contrast, increased particulate deposition was observed in the trench itself. The net effect was a slight increase in capture efficiency in the trench configuration.

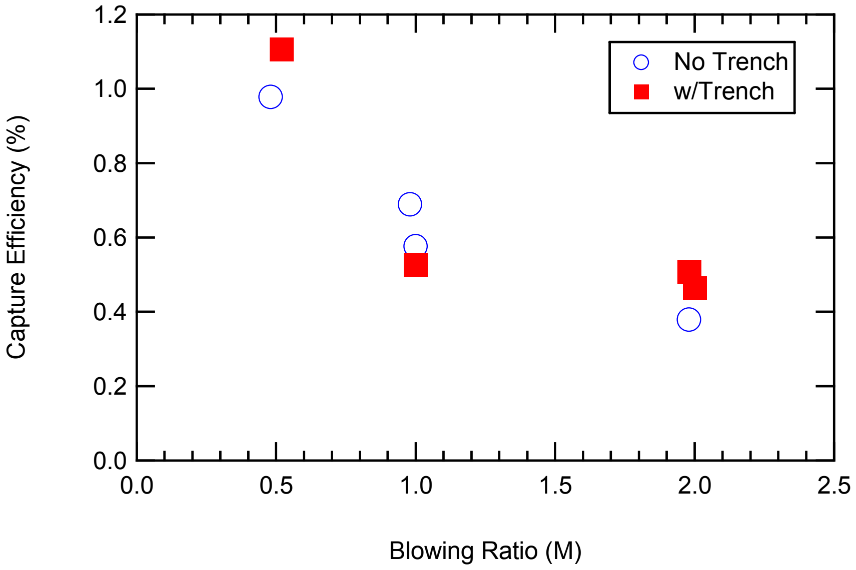

Figure 5.36 Capture efficiencies measured for bare metal coupons with and without a trench configuration (M5 and M6 respectively) at the various blowing ratios for α = 30° (3 holes blowing)

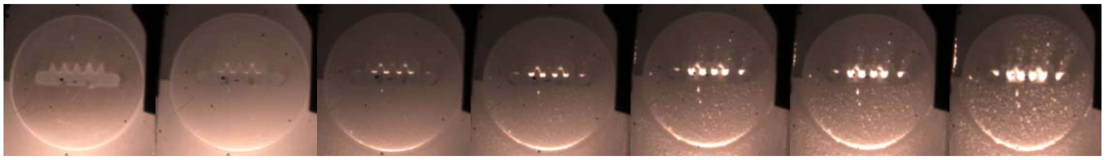

0 min 10 min 20 min 30 min 40 min 50 min 60 min

Figure 5.37 Time-dependent deposit development on the M5 coupon for α = 30° with and M = 1.0

5.5.2.1 Temperature maps

Temperature maps of the entire surface of the coupons with and without the trench configuration are shown in Figure 5.38 for M = 0.5 to 2.0 after 40 minutes. The direction of the main flow is from bottom to top. To distinguish observed features, the temperature maps are scaled from 1050 K to 1350 K for M = 2.0, and from 1150 K to 1350 K for the M = 1.0 and 0.5 cases. The X-Y coordinates are normalized by the coupon diameter. At M = 2.0 (Figure 5.38a1), no distinct coolant flow paths were observed downstream of the trench, but there is a large area where the downstream area was cooled. This effective cooling region suggests that the coolant ejected from the holes impacted on the trench wall, flooded laterally within the trench, and spread over the metal surface, greatly increasing coolant coverage under these conditions. Meanwhile, at M = 2.0 for the coupon without a trench (Figure 5.38b1), a region of low temperature caused by the coolant also appeared downstream of the film holes. However, distinct flow paths were visible, indicating good but not quite complete cooling coverage and minimal interaction between coolant flow paths at this blowing ratio. At M=1.0, the surface temperature distribution for the trench (Figure 5.38a2) indicates that the coolant coverage was not greatly affected by the decrease of blowing ratio. For case M6 (Figure 5.38b2), coolant coverage was reduced and two higher temperature bands appeared in the region between coolant paths. These data illustrate that blowing ratio influences the coolant coverage on the coupon without a trench more significantly than that with a trench. For M = 0.5, there did not seem to be significant cooling downstream of the cooling holes for either case (Figure 5.38a3 and Figure 5.38b3). With such a low blowing ratio, it appears that the mainstream momentum was much greater than the coolant, deterring the development of the coolant film. The M = 0.5 case with no trench seems to had slightly better cooling downstream of the holes than the case with the trench.

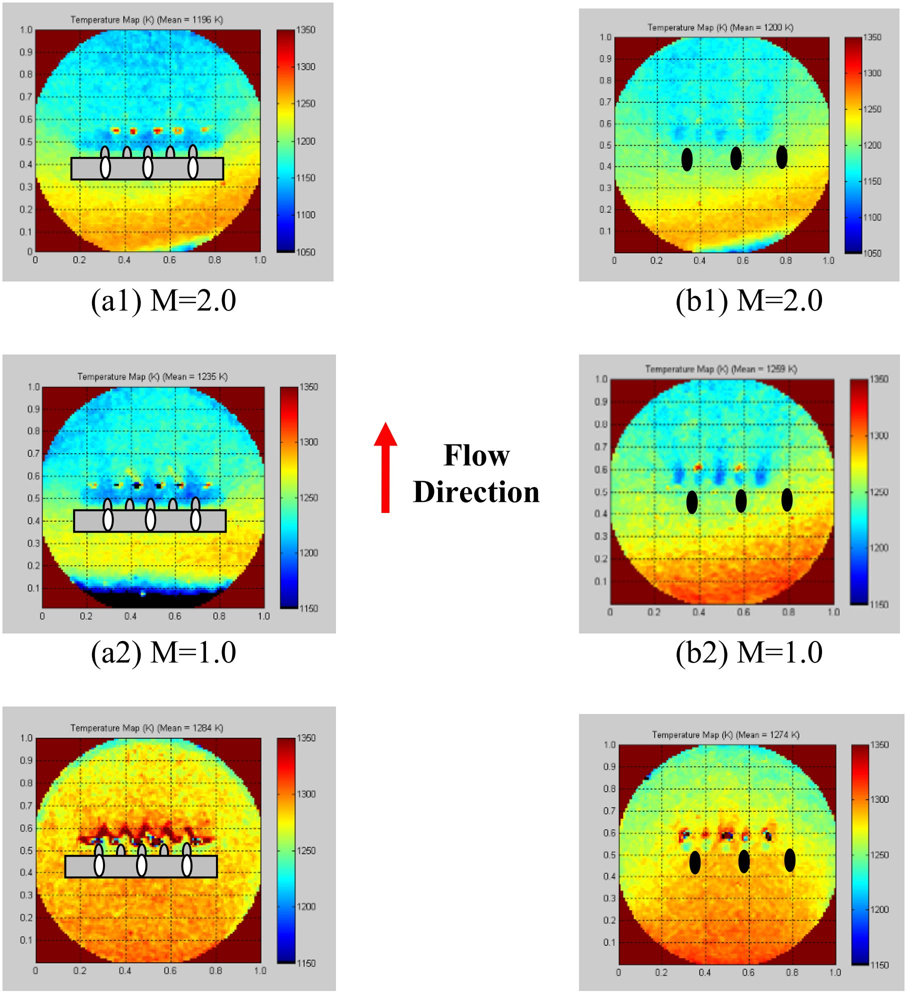

(a1) M=2.0

(b1) M=2.0

(a2) M=1.0

(b2) M=1.0

(a3) M=0.5

(b3) M=0.5

With a trench (M5)

Without a trench (M6)

Figure 5.38 Surface temperature maps after 40 minutes from fine particle tests on coupons with and without a trench for M = 0.5 to 2.0 and α = 30° (3 holes blowing)

Since the color maps can hide some trends, spanwise temperature distributions at y/d=2.0 downstream of the film holes are shown in Figure 5.39 for M = 2.0. The average spanwise temperature was 1234 K for case M6 and 1241K for case M5. The temperature of the region located on the two sides downstream of the film holes was lower for case M5 than for case M6. The temperature in the region covered by coolant on the coupon with a trench was relatively leveled, compared with the coupon without a trench, indicating that the coolant coverage caused by a trench was larger than pure cylindrical holes in this case. The two temperature peaks for both cases were downstream of the blocked holes, where more deposition occurred than at other locations.

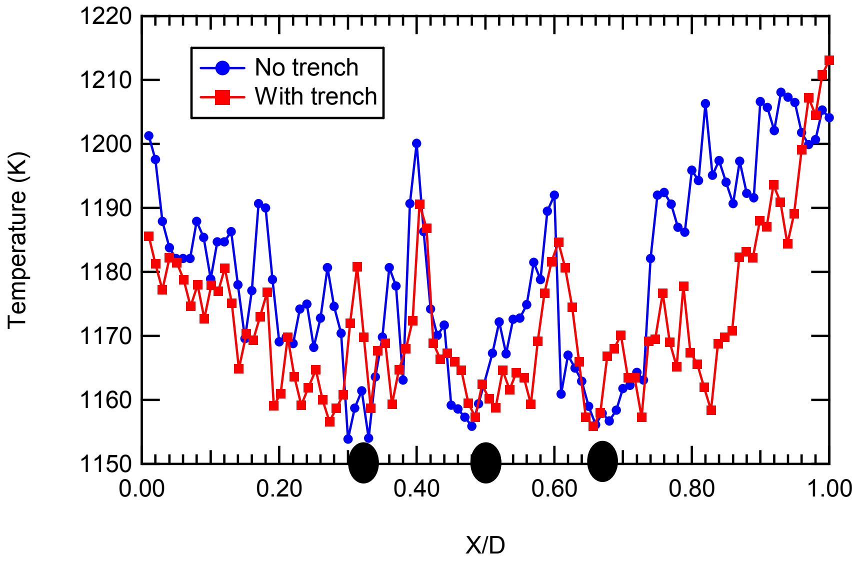

Figure 5.39 Comparison of spanwise temperature distribution for coupon with/without a trench at y/d=2.0 and M=2.0 for $\alpha = 30°$

5.5.2.2 Roughness

The coupon deposit was scanned after tests. At M=2.0, deposit in the region near the trench on coupon M5 with a trench was slightly higher than that at the same locations on the coupon M6 without a trench. The deposit for case M5 was distributed more evenly than for case M6 for the region scanned. Figure 5.40 summarizes the roughness statistics of deposits in the downstream region of film cooling holes for coupons with and without a trench for various blowing ratios. As can be seen, Ra and Rt decreased with increased blowing ratio. Ra decreased two orders of magnitude and Rt decreased one order of magnitude when M was increased from 0.5 to 1.0. Values of Ra and Rt are close for the two cases (with and without the trench).

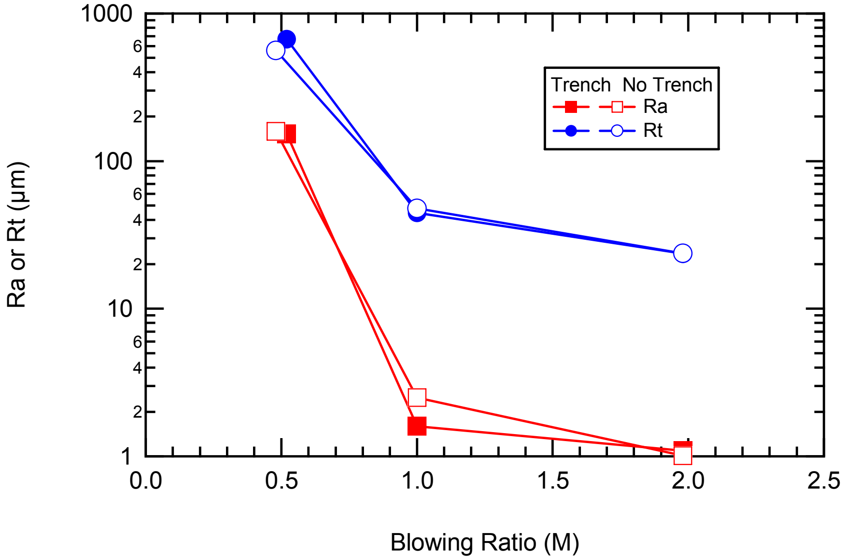

Figure 5.40 Roughness statistics of deposits in the downstream region of film cooling holes for coupons with and without a trench for various blowing ratios and $\alpha = 30°$

5.6 Summary of Experimental Results

Tests were performed in the TADF to evaluate the influence of hole geometry and size, blowing ratio, hole spacing, particle size, TBC and trench configuration on deposit formation from subbituminous coal flyash. Gas temperature, velocity, and net throughput of particulate out of the combustor were set to match conditions for a modern power turbine. Nominal combustor exit flow conditions were $\mathcal{M} = 0.25$ and a gas temperature of 1183°C.

The tests on the uncoated coupons with cylindrical and shaped holes showed that the capture efficiency decreased with increased blowing ratio. Shaped holes provided more spanwise coverage of coolant than the cylindrical holes, resulting in lower capture efficiency.

The observed deposition rate increased with time in a nonlinear fashion. The entrained particles more readily adhered to coupon surfaces where some initial deposit has been formed.

The surface temperature measurement suggests that the thermal resistance of the TBC layer raised the surface temperature compared with a bare metal coupon for the same gas temperatures and blowing ratios. The high surface temperature for the TBC coupon enhanced the particulate capture efficiency.

The effect of hole spacing on deposition was examined by performing tests on coupons with $s/d=3.375$ and 4.5. The roughness statistic parameters decreased monotonically with increasing blowing ratio for both values of hole spacing. Closer hole-spacing decreased capture efficiency slightly. Analysis indicated that heat transfer was influenced by multiple factors such as coolant flow momentum, blowing ratio, backside cooling, and mainstream flow properties.

The effect of particle size on deposition was investigated using particles with mean diameters of 4 μm and 12 μm. The smaller particles had lower particle capture efficiencies and more tenacicous deposits than the larger particles at the temperatures investigated here.

Deposit patterns were observed at impingment angles from 45° to 15°. A 30° angle was selected to study the effect of trench configuration on deposition. The surface temperature measurement suggested that the trench provided good coolant coverage at high blowing ratios (M = 1 to 2). However, the capture efficiency was not significantly improved despite the increased coolant coverage, since deposition occurred in the trench. At a low blowing ratio (M = 0.5), the case without a trench outperformed the case with a trench due to flow pattern changes caused by deposits in the trench. Even without the deposits, the trench configuration at M = 0.5 had lower cooling performance because the coolant momentum from the film cooling holes embedded in the trench permitted penetration from the bulk gas stream.

6. Film Cooling and Ash Deposition Modeling

The following modeling work investigates film cooling effectiveness and heat transfer coefficients with both conjugate heat transfer and adiabatic conditions in the region close to film-cooling holes and in the region downstream of a row of film-cooling holes. The simulation employed unstructured grids and the standard k-ω turbulence model. Comparisons are made between computational and experimental results to understand the effect of film hole spacing, hole-size and TBC on surface heat transfer. After heat transfer calculations, particle capture efficiencies are calculated and compared with measured values to evaluate the performance of the ash particulate deposition model. The following section introduces the details of the numerical computation model including the computational approach, conditions modeled, and the model predictions and discussion.

6.1 Model Description

The CFD model consists of a film cooling model and an ash deposition model. The ash deposition model includes (1) the delivery process of particles to the target surface and (2) the particle sticking process. A User Defined Function was written to describe the two processes described above and implemented in FLUENT to determine capture efficiencies of ash particles. A flow chart of the logic in the model is shown in Figure 6.1.

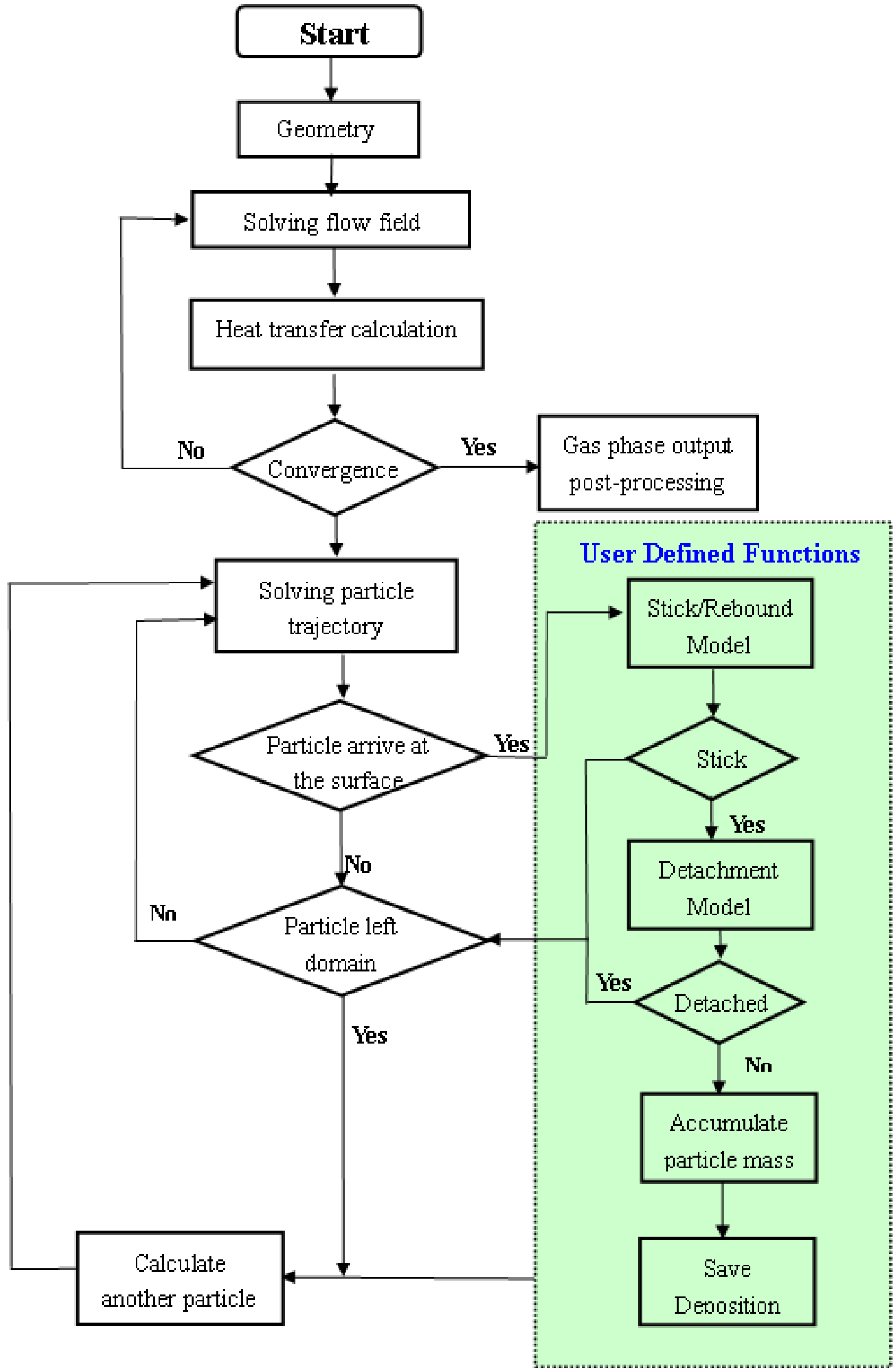

Figure 6.1 Deposition model flow chart

The deposition model of El-Batsh (2002) was employed in this simulation to study the particle-wall interaction. First, the flow field for the given geometry was solved using the appropriate fluid flow and heat transfer models and the specific boundary conditions. After the convergence of the gas phase, the Lagrangian dispersion model was employed to calculate the particle trajectories. User Defined Functions linked to Fluent were developed in the C language to describe particle sticking and detachment. These two models were applied to describe the interaction of particles with the wall surface to calculate the actual rate of particle deposition when the particles impinge the surface. These calculations were repeated until all particles were counted. The mass of particles sticking to the surface was accumulated and saved to calculate the corresponding capture efficiency.

6.2 Approach

6.2.1 Gas Phase Simulation

Simulations were performed using FLUENT 6.3.26 with Reynolds-averaged Navier-Stokes (RANS) transport equations (2005). The continuity, momentum and energy equations in the fluid and solid regions were solved to predict film cooling effectiveness, velocity, and temperature fields for conjugate heat film cooling from the holes. The interface between fluid and solid was specified as a coupled boundary, which avoided the use of the film-cooling heat transfer boundary condition and allows a direct calculation of the heat transfer and wall temperature. The physical domain was separated into fluid and solid blocks by the wall. The three-dimensional Navier-Stokes equations and turbulence equations were solved in the fluid blocks. The Fourier equation was applied in the solid body blocks. Coupling of fluid blocks and solid blocks was achieved by equating the local heat fluxes passing through the common cell faces.

The SIMPLE (2005) algorithm was used to couple the pressure and velocity equation. Numerical coefficients are determined by the QUICK (Leonard, 1990) scheme for the momentum equations. The discretization of the energy conservation equation was performed using a first-order upwind scheme, and the k-ω equation was discretized using a second-order upwind scheme. Convergence was determined by the orders of magnitude reduction of parameter residuals: 4 for the residuals for continuity, 6 for velocity, 7 for energy, and 5 for turbulence quantities.

6.2.2 Ash Deposition Model

6.2.2.1 Particle transport model

The Lagrangian approach has been applied in many studies of particle or droplet-laden flow, with good success. This approach also gives the complete information on particle impact at the surface required for sticking studies. The two forces considered in the transport model were the drag force at steady state and the Saffman lift force. The drag force at various Reynolds numbers was based on the introduction of the drag coefficient C_D, defined as:

$$C_D \equiv \frac{F_D}{1/2\rho_p \Delta V^2 A} = \frac{24}{\mathrm{Re}_p} \text{ , where } \mathrm{Re}_p = \frac{d_p \rho |u - u_p|}{\mu} \qquad (6\text{-}1)$$

where F_D is the drag force in x-direction, d_p is the particle diameter, Re_p is the particle Reynolds number, u is the fluid velocity, u_p is the particle velocity, and μ is the molecular viscosity of the fluid. The equation is suitable in the case where Re_p is less than or equal to 1.

The Saffman lift force is a result of the non-uniform relative velocity over the particle moving in a shear layer. The force F_s (Safman, 1965; Li and Ahmadi, 1992)is defined as

$$F_s = \frac{2K\nu^{1/2}\rho d_{ij}}{\rho_p d_p (d_{lk} d_{kl})^{1/4}} (\vec{v} - \vec{v}_p) \qquad (6\text{-}2)$$

where K=2.594 and d_{ij} is the deformation deformation tensor. This form of the lift force is intended for small particle Reynolds numbers. Also, the particle Reynolds number based on the particle-fluid velocity difference must be smaller than the square root of the particle Reynolds number based on the shear field. However, the particle and gas velocity components are fluctuating due to turbulence. Modeling particle impaction is difficult. In this model, the dispersion of particles was predicted using the particle cloud model.

The trajectory of the particle was predicted by the integration of its equation of motion that is written as:

$$m\frac{du_p}{dt} = F_D + F_x \qquad (6\text{-}3)$$

The first term on the right hand side of this equation represents the drag force per unit particle mass, and F_x stands for additional accerlation term.

Only the heating of particles was considered in the calculations of the heat transfer. Bio number calculated from particle with diameter of 5μm is 0.043, which was less than 0.1 and satisfied the criterion of the lump capacitance method. Phase changes of the particle and particle radiation were not taken into account. The equation of particle temperature is defined as:

$$m_p C_p \frac{dT_p}{dt} = hA_p (T_\infty - T_p) \qquad (6\text{-}4)$$

where m_p is the particle mass, C_p is the particle specific heat. T_p is the particle temperature, A_p is the surface area of the particle, and h is the convective heat transfer coefficient. The assumption is made that the particle has no effect on the fluid flow due to the dilute flow.

6.2.2.2 Particle-wall interaction

The particle-wall interaction determines the fraction of incident particles that remain on the surface, and consists of two interaction processes. One interaction is a pure mechanical interaction in the absence of the fluid force. This interaction mainly determines the condition at which no rebound occurs and is called the sticking process. The other interaction is the detachment process, which is a fluid dynamic interaction between the fluid and the adhered particles. This second interaction describes the stability of the particles at the surface.

Once particles impact on the surface, deposit build-up depends on the balance of sticking forces and removal forces acting on the particles at the surface. The sticking coefficient is the mass fraction sticking to a surface among incident particles. Van der Waals forces, electrostatic forces and liquid bridges play a significant role during the process of particle sticking. In the case of particle deposition on gas turbines, the van der Waals force is the major contributor to the particle sticking force. The sticking force F_{po} in the macroscopic approach (Soltani and Ahmadi, 1994) is calculated as:.

$$F_{po} = k_s W_A d_p \tag{6-5}$$

where k_s is equal to $3\pi/4$ and W_A is a constant which depends upon the material properties of the particle and of the surface.

The capture velocity is defined as the velocity at which the particles are captured by the surface. The capture velocity in the present study is given by (Brach and Dunn, 1992)

$$v_{cr} = \left[\frac{2E}{d_p}\right]^{\frac{10}{7}} \tag{6-6}$$

$$E = 0.51\left[\frac{5\pi^2(k_1 + k_2)}{4\rho_p^{3/2}}\right]^{2/5} \tag{6-7}$$

$$k_1 = \frac{1 - \nu_s^2}{\pi E_s} \tag{6-8}$$

$$k_2 = \frac{1 - \nu_p^2}{\pi E_p} \tag{6-9}$$

where υ_{cr} is the particle capture velocity [m/s], E_s is the Young's modulus of surface material [Pa], ν_s is the Poisson's ratio of surface material, E_p is the Young's modulus of particle material [Pa], ν_p is the Poisson's ratio of particle material, d_p is the particle diameter [m], and ρ_p is the particle density [kg/m^3].

The particle normal impact velocity is compared to the particle capture velocity, and if the particle normal impact velocity is smaller than the capture velocity, the particle sticks. Otherwise the particle rebounds and continues the trajectory until it leaves the domain or impacts the surface at another place.

The critical moment theory (Soltani and Ahmadi, 1994) is applied to describe the mechanism of particle detachment from a surface. The critical wall shear velocity $u_{\tau c}$ is:

$$u_{\tau c}^{2} = \frac{C_u W_A}{\rho d_p} \left(\frac{W_A}{d_p K_c} \right)^{\frac{1}{3}} \tag{6-10}$$

where $u_{\tau c}$ is the critical wall shear velocity, C_u is the Cunningham correction factor, d_p is the diameter of particle, and K_c is the Composite Young's modulus. The particle will be removed from the surface if the turbulent flow has a wall friction velocity (= $\sqrt{\tau_{\omega} / \rho}$, where τ_w is the wall shear stress) which is larger than $u_{\tau c}$.

6.3 Young Modulus Determination

6.3.1 2-D Modeling

The sticking model used here calculates the capture velocity of the particle at the surface based on the van der Waals force. The capture velocity was determined by the size of the particle, temperature, and the material properties of the particle and target surface. An important model parameter in the model is the Young's modulus (E), which is not available in the literature. Soltani and Ahmadi (1994) documented that the E of the target surface for the steel is 2.15×10^{14} Pa while E of the particle ranges from 1×10^{5} Pa to 1×10^{10} Pa. The E was obtained in this study by fitting experimental data. Experiments were performed in the TADF with gas temperatures varying from 1294 K to 1453 K. The coupon was made of Inconel and the backside was insulated by ceramic material, resulting in adiabatic conditions. The ash-laden gas impinged upon the disk with a 45° angle. The capture efficiency was calculated as the deposit mass divided by the particle mass fed into the system. The testing conditions and capture efficiency are summarized in the Table 6-1.

Table 6-1. Summary of experiments to tune the value of the Young Modulus

Inlet velocity [m / s]	173		
Coupon	Bare Metal		
Particle mass mean d [um]	13.4		
Temperature [K]	Gas	Metal Surface	Capture Efficiency(%)
	1453	1311	7.87
	1425	1281	4.47
	1408	1270	2.938
	1374	1234	0.932
	1352	1232	0.517
	1293	1191	0.0001

Two-dimensional numerical computations were performed to solve the flow field and particle trajectories for this set of tests. A schematic and boundary conditions of the model are presented in Figure 6.2 and Figure 6.3. The model geometry included 30,100 cells. The inlet velocity was 173 m/s and the wall of the inlet tube was adiabatic. All other walls were assumed as a pressure outlet with a temperature of 300 K, simulating atmospheric conditions. The fluid was incompressible air and the flow field was calculated using the standard k-ω model.

When the particles arrived at the target surface, the sticking model was applied to determine whether the particle sticks to the surface or escapes. To investigate the correlation of Young's modulus with temperature, the model was tuned to fit the capture efficiency obtained in the experiments. The assumption was made that the particle sticking properties represent the target surface properties as well. The temperature used is the average value of surface cell and particle. The composite Young's modulus was computed by setting the Poisson ratio to a constant value of 0.27 for both the particle and the surface since a thin deposit layer has developed on the surface after several miniutes in deposition test.

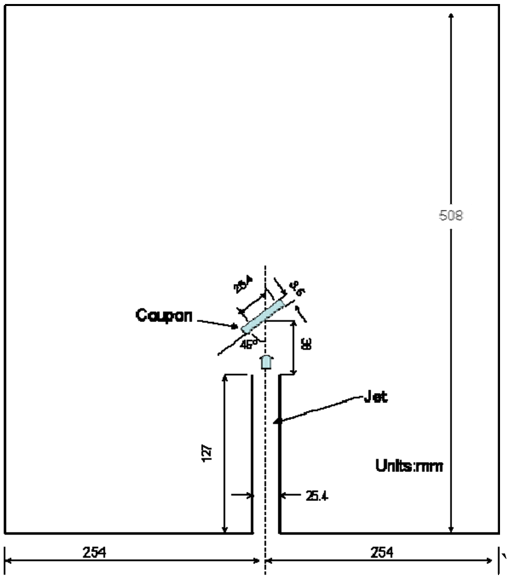

Figure 6.2 Schematic of the 2D model

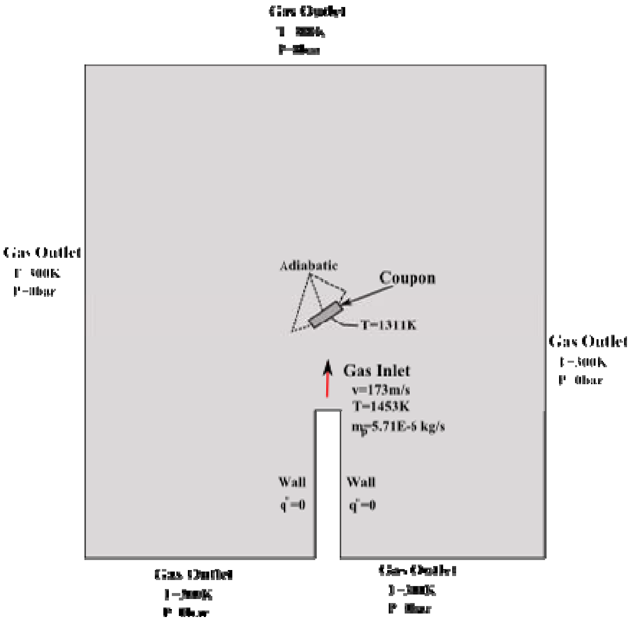

Figure 6.3 2D model boundary conditions

The continuous-phase flow field was solved and the discrete-phase trajectories were tracked. As the particle impacted on the target surface, the particle temperatures and velocity were calculated as well. The capture velocities were calculated on the basis of the fitted value of the Young's modulus. The particles with normal velocities less than the capture velocity stuck to the surface. The capture efficiency is the ratio of the mass of the adhered particles to the total mass of particles injected into the domain. The average between the particle temperature and the surface temperature was used to determine the properties for the deposition model. This process was iterated with different values of E_p until the capture efficiency in the model was in agreement with the result obtained in the experiments for each gas temperature. The dependence of Young's modulus on the temperature was then fit to an exponential function, as shown in Equation 6-11. Figure 6.4 shows the calculated capture efficiency from the CFD model using Equation 6-11. Good agreement is shown with the experiments performed as a function of gas temperature.

$$E_p = 3\times 10^{20} \exp(-0.02365 T_g) \qquad (6\text{-}11)$$

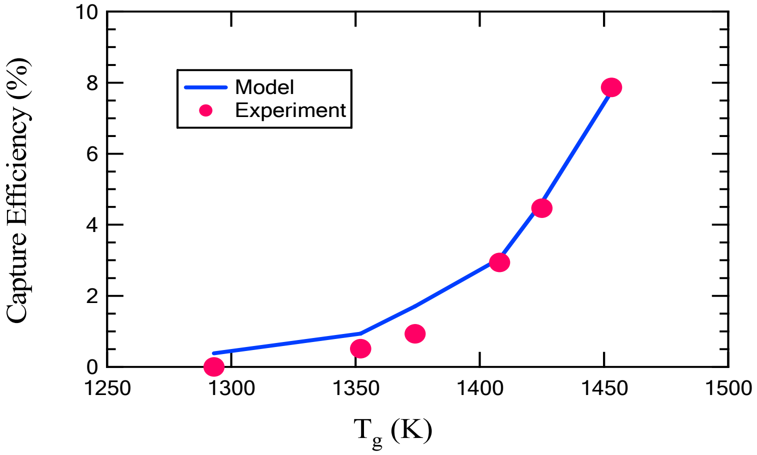

Figure 6.4 **Fitted capture efficiencies obtained from 2-D CFD modeling versus measured values**

6.3.2 Description of Input Parameters in UDF

The User Defined Functions (UFDs) describing the deposition model and post-process have some input and output parameters throughout the simulation process. The definitions of these parameters are given at Table 6-2 below for easily reading and understanding, including the units where applicable.

Table 6-2. List of parameters used in the UFD

Variables in the text	Parameters	Description	Unit
Input Parameters			
E_p	YM_EP	Young's modulus of surface materials	Pa
E_s	YM_ES	Young's modulus of particle material	Pa
ν_p	PR_VS	Poisson ratio of surface material, constant=0.27	
ν_s	PR_VP	Poisson ratio of particle, constant=0.27	
W_A	WA	Sticking work between particle and the surface, constant=0.039	J/m^2
R	Gas_Con	Gas constant=286.9	J/ (K.kg)
	GasV	Mean molecular speed	m/s
μ	GasViscosity	Gas Viscosity=1.79×10^{-5}	Pa.s
	Kn	Knudsen Number	
	Cu	Cunningham correction factor=1.2	
E	Kc	The composite Young's modulus	Pa
u_p	absP_V	particle velocity magnitude	m/s
Output Parameters			
/	Position_x	x coordinate value of position as the particle impinges on the surface	m
/	Position_y	y coordinate value of position as the particle impinges on the surface	m
/	Position_z	z coordinate value of position as the particle impinges on the surface	m
/	Avg_diameter	The average diameter of particles hitting on the surface	m/s
/	Num_of_Hits	The total number of particles hitting on the surface	
/	Sum_Mass	The flow rate of particles hitting on the surface	$[g/s]x10^{-9}$
/	Surface_T	Surface temperature	K

Table 6-2 (Continued)

Variables in the text	Parameters	Description	Unit
/	Particle_T	Particle temperature	K
/	P_Stick_Mass	flow rate of particle sticking to the surface	[g/s]x10^{-9}
/	Thickness	deposition thickness	um
/	CaptureEff	Overall capture efficiency	%
/	ImpactEff	Overall impact capture efficiency	%
/	Impact_Cap[]	Impact capture efficiency of varied size particles	%
/	Stick_Cap[]-	Stick capture efficiency of varied size particles	%

6.3.3 UDFs Intergated in FLUENT

Before UDFs are utilized, they need to be connected with FLUENT. After UDFs were interpreted or compiled and loaded into FLUENT, the function(s) contained in the interpreted code or shared library will appear in drop-down lists in graphical interface panels, ready to hook to the CFD model. Of the six functions, three must be properly incorporated into FLUENT to work properly, the other three were executed upon demand. The function of gas density dependence on temperature was intergrated in the material properties. The deposition model UDF, which determines particles sticking to the surface, was hooked via the wall boundary conditions panel under the DPM (discrete phase model) tab. The injection-initializing UDF was incorporated into FLUENT through the injections panel under the UDF tab. Before executing the post-processing function, the memories had to be reset.

6.3.4 2-D Modeling Results

Although particles can be delivered by the inertial force to the targeted surface, the deposition that occurs depends on whether particles stick upon arrival at the surface. To specify the effect of delivery and attachment on surface deposition, the capture efficiency was divided into two terms: impact efficiency and sticking efficiency. Impact efficiency is defined as the ratio of mass of particles impacting the surface to the total particle mass flowing into the system. Sticking efficiency is the ratio of the mass of particles sticking on the surface to the mass of impacted particles. Figure 6.5 shows calculated impact efficiency, sticking efficiency and overall capture efficiency for different size-classes of particles. As can be seen, the impact efficiency increased with particle size. For 8-10 um diameter particles, the impaction efficiency in this experiment was close to 100%. This is due to the large Stokes number, which enabled particles to maintain their line tracks and impact the target surface. The temperature had only a slight effect on impaction efficiency. Equation (6-12) above shows that the critical capture velocity of particles was decreased to particle size, which indicates that small particles had a greater tendency to stick on the surface than large particles. Figure 6.5b shows that the sticking efficiency decreased with increasing particle size. For particles larger than 10 um, the sticking efficiency was close to zero while for particles less than 2 um, the sticking efficiency was 100%. For a given particle size, the sticking efficiency increased with increasing temperature.

The capture efficiency for different particle sizes was obtained by multiplying the impact efficiency by the sticking efficiency, as shown in Figure 6.5c. At the lowest temperature of 1293 K, the peak capture efficiency appeared in the size range of 2-4 μm. At 1453 K, the peak was located in the range of 8 μm. The influence of temperature on deposition for various particle sizes was implied in the Young’s Modulus correlation (Eq. 6-13). The capture efficiency peak shifted to the larger sized particles with increased temperature. This result was consistent with the conclusion made by Wenglarz and

Wright (2003) who reviewed test results for a number of alternate fuels. When the gas temperature is below the transition temperature, the main contribution to desposition is vaporized species from small particles. Above the transition temperature, particles larger than 1 μm are molten. Due to the high delivery rate of large particles, a much greater mass of large particles stick on the surface, resulting in a significant increase in the mass of deposit.

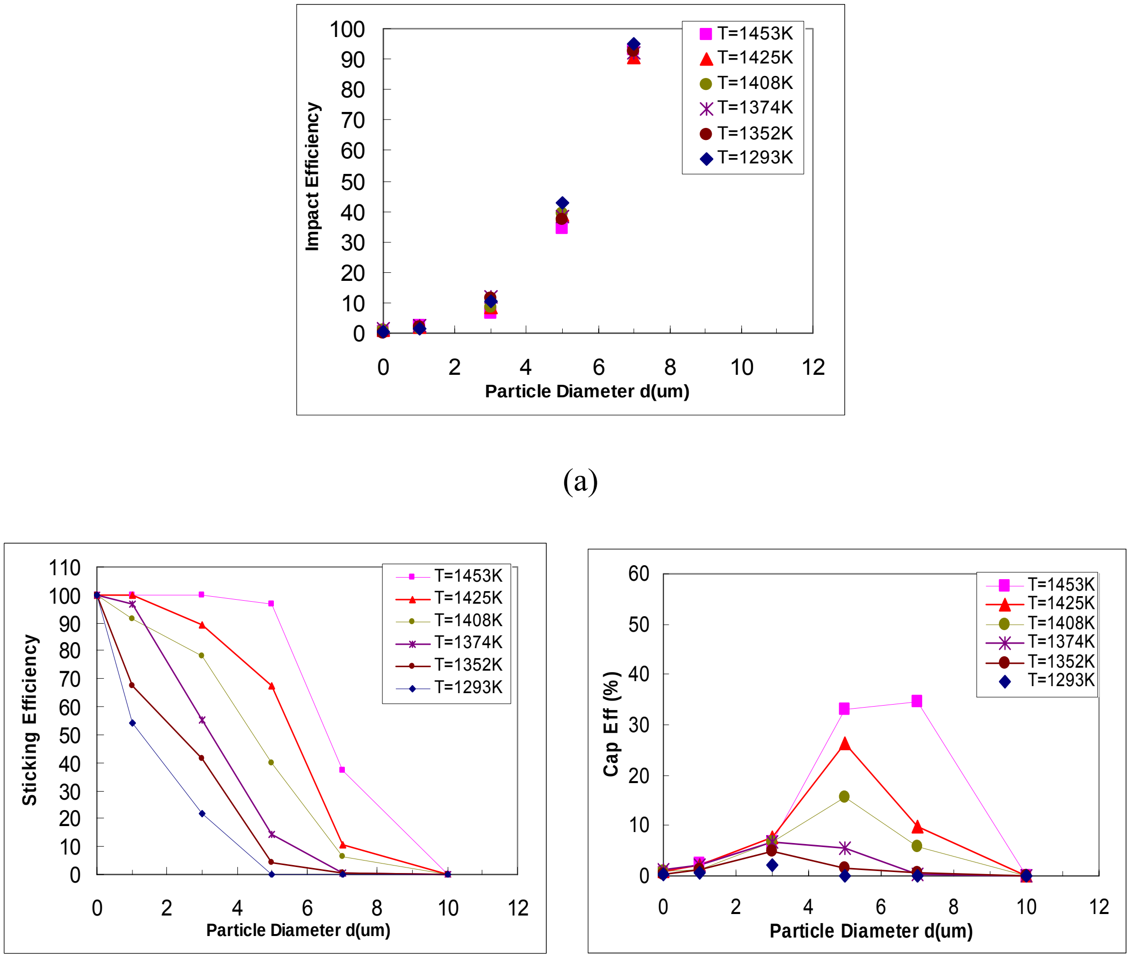

(a)

(b)

(c)

Figure 6.5 2-D CFD calculations of (a) impact efficiency, (b) sticking efficiency, and (c) capture efficiency versus particle size for various gas temperatures

6.4 3 Dimensional Film Cooling Model

6.4.1 Geometry

A schematic of the computational domain to simulate the experiment is shown in Figure 6.6. The computational domain included the coolant supply channel, the cylindrical cooling holes, and mainstream duct. The crossflow section was 39 mm in width, 36 mm in height and 81 mm in length. The row of three inclined film-cooling holes with a 30° angle against the plate was located 36 mm downstream of the flat plate leading edge and 45 mm upstream of the fluid outlet. The hole diameter was 1.5 mm and hole spacing was 3 times that of the hole diameter for case M3. The thickness of the plate was 3.5 mm and the length-to-diameter ratio L/d of coolant passage was 4. A high temperature circular gas jet with a diameter of 25.4 mm impinged on the flat plate with a 45° angle, and blended with the film cooling air, and then flowed out at the exit located in the schematic to the right side of duct. The coolant fluid was injected from a tube with a diameter of 13.5 mm to a plenum located beneath the plate. The coolant plenum was 40.5 mm in height, 39 mm in width and 81 mm in length. The mainstream gas temperature was specified at 1453 K, and the measured density ratio was matched by varying the temperature of the inlet coolant. Additional cases were performed with the same geometry except for different hole sizes and hole spacing.

6.4.2 Grid Generation and Independence

Geometry and the mesh grid were generated in GAMBIT using unstructured tetrahedral topology grids, which consisted of tetrahedral cells, as shown in Figure 6.7. The total number of computational cells was 475,034 for case M3 and 421,949 for cases

M1 and M2. The accuracy of the computational model is strongly dependent upon the quantity and location of grids that resolve the relevant flow physics. To study grid-independence, three test grids were used to compute film cooling of the flat plate with conjugate heat transfer, with 475,034 to 1,551,455 cells. The centerline effectiveness downstream of the middle film hole is shown in Figure 6.8 for the grid-independent calculation. The finer mesh resulted in little change downstream in the region close to film holes (Y/d < 10). Therefore, the mesh with the lowest number of grids was adapted for subsequent computational cases.

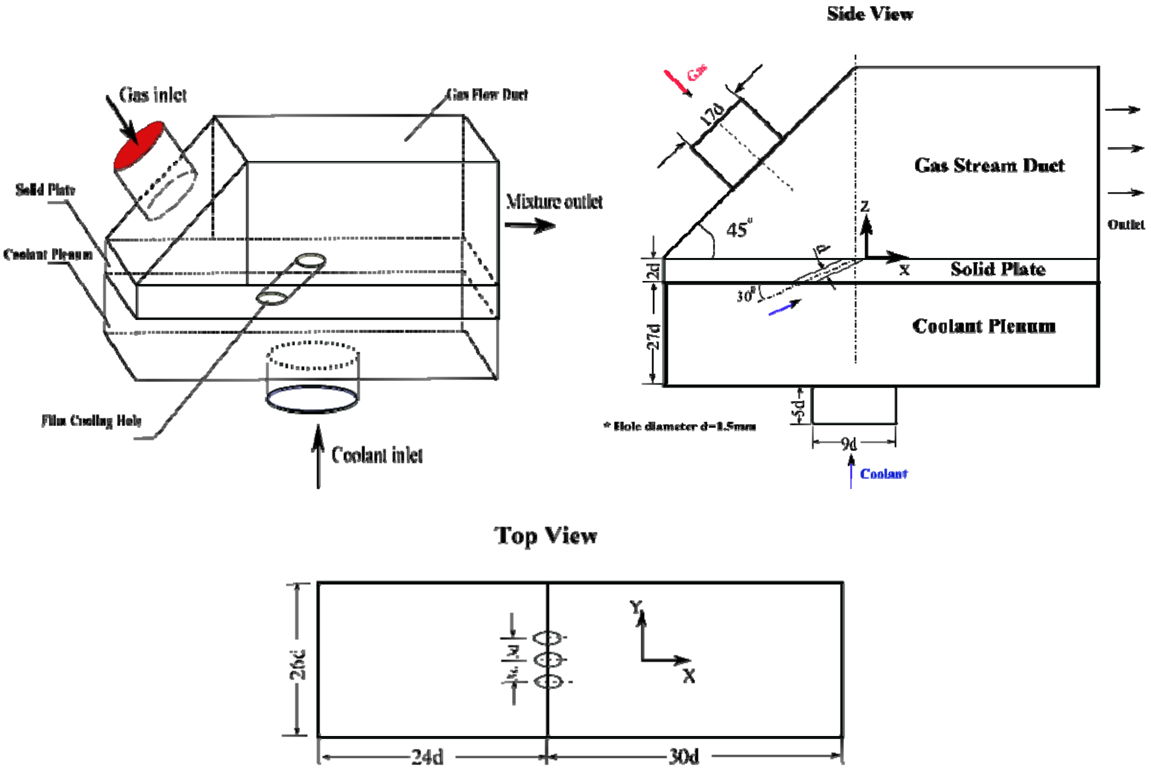

Figure 6.6 **Schematic of the overall computational domain**

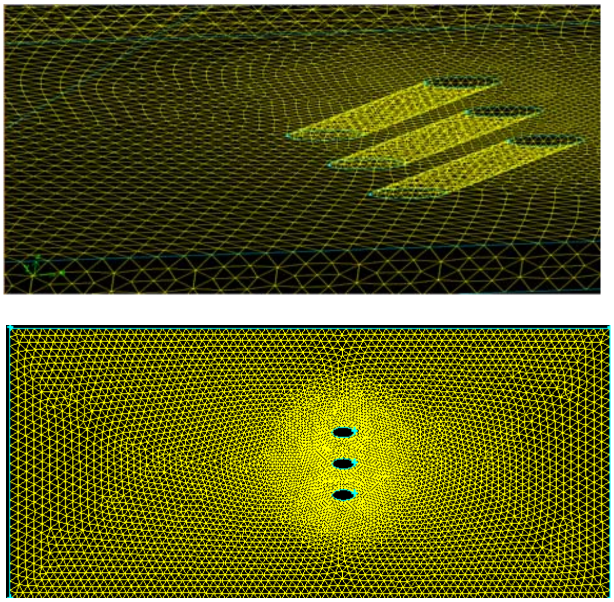

Figure 6.7 Details of the grid used in the simulations

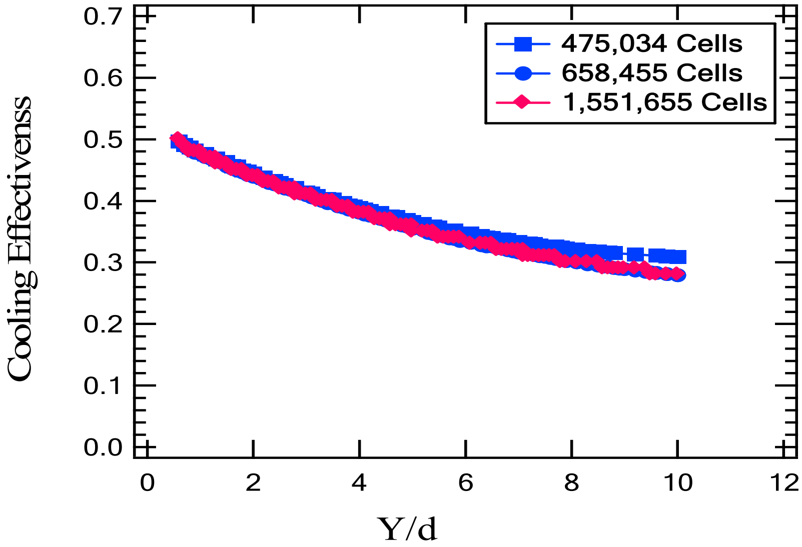

Figure 6.8 Grid sensitivity study-centerline normalized temperature for the three grids

6.4.3 Boundary Conditions

Seven simulation cases were chosen to match the experimental test cases, as shown in Table 6-3. The boundaries were defined from experimental conditions. The mainstream inlet velocity was set to 173 m/s and 1453 K for all cases. The k and ω profiles were specified using a uniform distribution corresponding to a turbulence intensity of 4.7% for most cases. The temperatures on the top and side walls of the mainstream duct were set to 900 K except for the wall close to the inlet, which was 300 K. The viscosity of fluid was set to a constant value of 1.79×10^{-5} kg/(m·s). The top and bottom walls of the solid plate were specified as a coupled wall in the FLUENT solver, which avoided specifying the heat flux or other boundary conditions. The surrounding walls of the solid plate were set to be adiabatic, requiring the heat flux to be in only one direction inside the solid plate. At the outflow boundary, the gradients of all flow variables with respect to the streamwise direction were set to zero, and the no-slip condition with wall function was applied at the walls. The temperature at the inlet of the coolant plenum was varied to obtain the measured density ratio in each experiment. The walls of the coolant plenum were set to be adiabatic. The gas was modeled as incompressible air using the ideal gas law, with gas density a function of the fluid temperature.

In the deposition simulation, 5000 ash particles were released at the center of the mainstream inlet surface and impinged the target plate. The temperatures and velocities of the particles were set to the same values as the mainstream gas. The properties of the ash particles are listed in the

Table 6-4. The average size of particles in the simulation was 13.4 um and the particle size bins complied with a Rosin-Rammler logarithm distribution. Particle trajectories and temperatures were modeled using the Lagrangian stochastic random-walk model, which is based on the force balance on the particle and on the convective heat from the particle. The Runge-Kutta method was used to integrate the particle equations, and the Cunningham correction to Stokes's drag law was also used. The Cunningham correction factor is set as a value of 1.2 in consideration of the particle size range. Each particle in the deposition simulation was tracked as it was carried through the computational domain by a combination of steady velocity streamlines and simulated turbulent eddies.

Table 6-3. Summary of cases simulated

Case	Plate Hot side	Plate	D (mm)	s/d	TBC	k_t of SA/TBC (W/m·K)	Blowing Ratio (M)
1	Conjugate	M1	1.0	3.4	N/A	9/n.a.	0.5,1.0,2.0
2	Conjugate	M2	1.0	4.5	N/A	9/n.a	0.5,1.0, 2.1
3	Conjugate	M3	1.5	3.0	N/A	9/n.a	0.5,1.0,1.5,2.0
4	Adiabatic	M2	1.0	4.5	N/A	0/n.a.	1.0
5	Adiabatic	M3	1.5	3.0	N/A	0/n.a.	1.0
6	Conjugate	TBC	1.0	4.5	Yes	9/1.78	1.0
7	Conjugate	TBC	1.0	4.5	Yes	9/0.3	1.0

* k_t is thermal conductivity. SA means super-alloy, vs. TBC.

Table 6-4. Particle properties

d(μm)	ρ(kg/m^3)	Cp(J/kg·K)	K(W/m·K)
13.4	990	984	0.5

6.4.4 Results and Discussion

6.4.4.1 Hole spacing(s/d=3.375 and 4.5)

To study the effect of hole spacing on film cooling, computations were made for two cases with hole spacings of s/d=3.4 (Case 1) and 4.5 (Case 2) for blowing ratios (M) from 0.5 to 2.0. Comparisons were made of predicted and measured average front and rear plate temperature (Figure 6.9) and deposition capture efficiency (Figure 6.10). The temperature here was obtained by using 2-color camera technique in the expriments. As can be seen in Figure 6.9, the predicted temperatures at M=2.0 for case 1 agrees with experiments better than at M=1.0. The predicted temperatures for both front and back sides at M=0.5 were higher than the measured values. For case 2, the predicted temperatures at M=0.5 and 2.0 were close to the experimental results while there was a slight disagreement at M=1.0. In general, the predictions for case 2 agreed with the data better than for case 1.

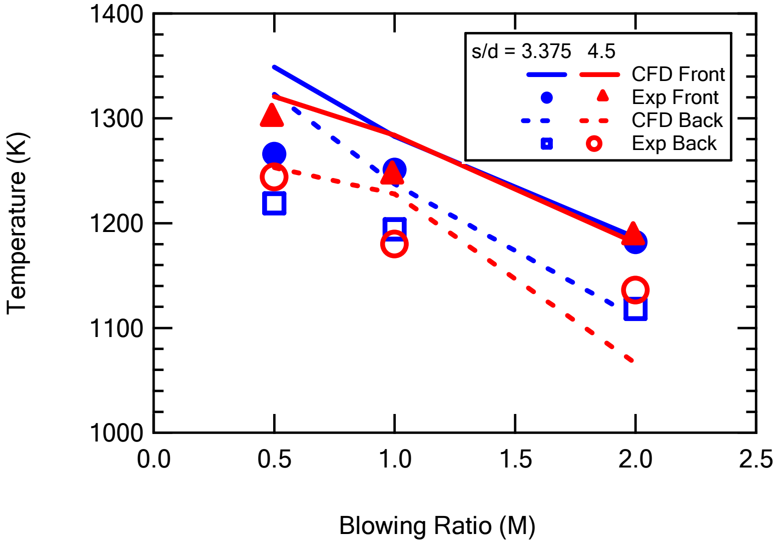

Figure 6.9 Comparison of averaged front-side and backside plate temperature for cases s/d=3.4 and 4.5 from experiment and 3-D modeling

Figure 6.10 shows the deposition capture efficiency as the function of blowing ratio for varying hole spacing cases. The figure suggests that the deposition model correlates capture efficiency fairly accurately over this range of blowing ratios. The areas of disagreement shown in this figure reflect the areas of disagreement shown earlier for the respective plate surface temperature. Capture efficiency was over-predicted slightly for case 1 with M=0.5 and 1.0 due to a higher simulated surface temperature. The predicted capture efficiency for case 2 with M=1.0 was lower in the simulation than that obtained from experiments. This figure also shows that the capture efficiency for close hole spacing was slightly lower than for wide hole spacing except at M=1.0.

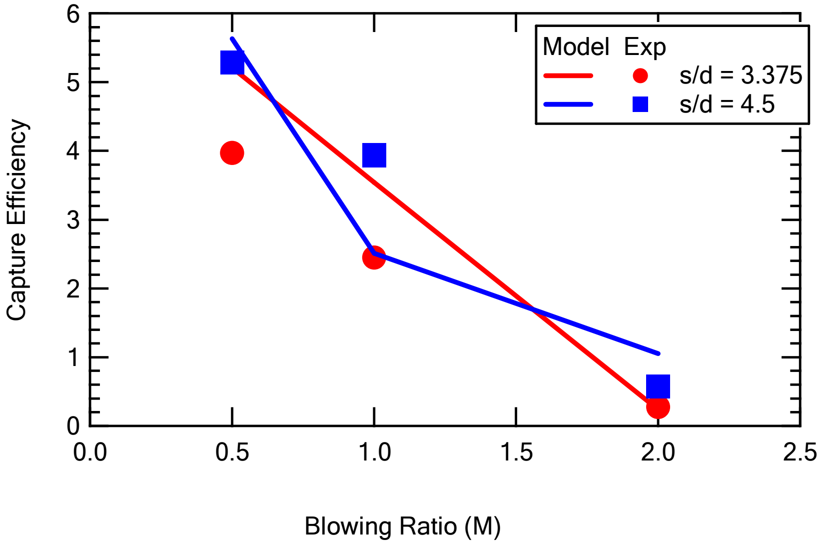

Figure 6.10 Capture efficiency at M=0.5 to 2.0 for cases s/d=3.4 and 4.5 from experiment and 3-D modeling

6.4.4.1.1 Film cooling effectiveness

The use of an overall effectiveness factor is a method of normalizing the temperature, and is defined as:

$$\eta = \frac{T - T_\infty}{T_c - T_\infty} \tag{6-14}$$

where T is the wall surface temperature downstream of film holes, T_c is the coolant temperature at the entry of the passage of the holes and T_∞ is the mainstream temperature. The laterally averaged effectiveness was obtained by spanwise averaging of the local values. This evaluation was performed for the downstream range from Y/d=1 to 12, where Y = 0 at the hole axis. The diameter of coupons used in the experiment was 25.4 mm. Therefore, only the local points within a radius of less than 12.7 mm were accounted for averaging lateral values.

Figure 6.11 shows the results of the laterally-averaged effectiveness for a variation of the blowing ratio from 0.5 to 2.0 with the two differing hole spacings. The curves reflect the effects of three cooling air jets interacting with each other and mixing with hot gas crossflow. The figure shows that cooling effectiveness rose with the increase of blowing ratio. The development of lateral effectiveness with downstream distance continuously decayed due to the interaction with the hot mainstream after ejection from the cooling holes. The different hole spacing caused a slight variation in the downstream decay characteristic, which developed more rapidly for a plate with a wider hole spacing. The cooling effectiveness for the plate with wide hole spacing was larger than the case with close hole spacing at all blowing ratios in the location near cooling holes. Due to less support of neighboring coolant jets with large hole spacing, the coolant flow was diluted by the hot gas flow at the region far away from the cooling holes, resulting in a lower cooling effectiveness than the close spacing at the Y/d greater than value of 5. This was most apparently observed at the low blowing ratio of 0.5.

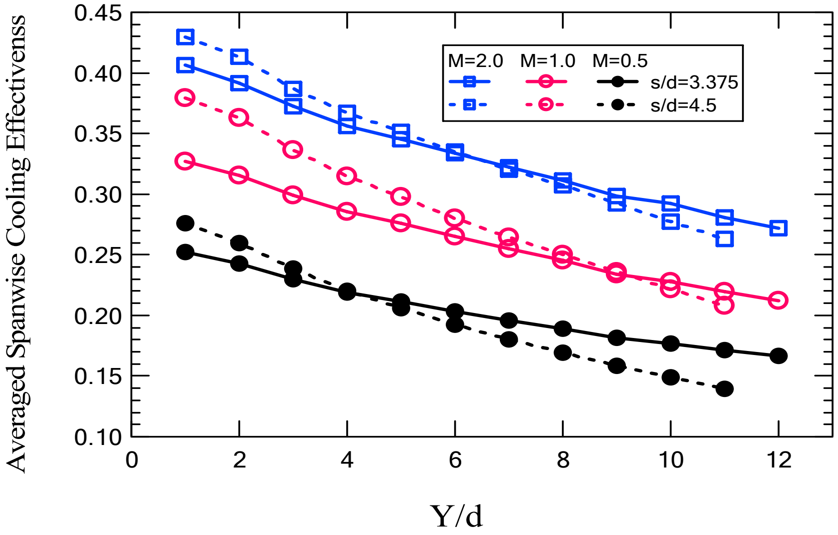

Figure 6.11 Laterally-averaged film cooling effectiveness at the variation of M from 0.5 to 2.0 with s/d=3.4 (Case 1) and 4.5 (Case 2)

The centerline cooling effectiveness for a variation of the blowing ratio from 0.5 to 2.0 with two differing hole spacings is shown in Figure 6.12. The centerline is defined as the region downstream of the middle hole. As can be seen, the centerline cooling effectiveness monotonically decreased along the downstream distance. In the region downstream close to film cooling holes, it did not appear as in the adiabatic case that the cooling effectiveness at low blowing ratio was greater than that at high blowing ratio. It indicates that conjugate heat transfer impeded the occurrence of ejected coolant at higher blowing ratio. The value of the cooling effectiveness along the centerline was slightly higher than the laterally-averaged spanwise cooling effectiveness. Otherwise, the centerline effectiveness curves were similar to the spanwise-averaged curves. For all of the blowing ratios, the wide hole spacing yielded better cooling effectiveness than close hole spacing in the region close to the exit of coolant.

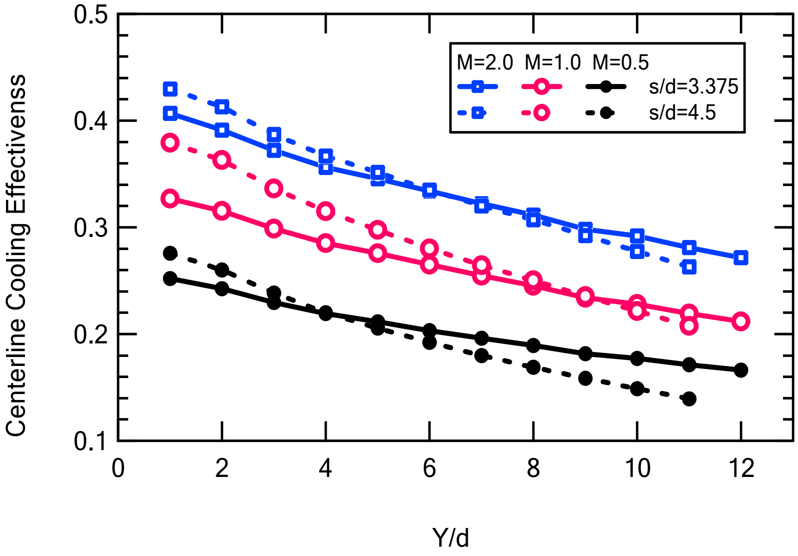

Figure 6.12 Centerline film cooling effectiveness at the variation of M from 0.5 to 2.0 with s/d=3.4 (Case 1) and 4.5 (Case 2)

6.4.4.2 Hole size (d=1.5 mm, s/d=3.0)

The hole diameters were changed from 1 mm to 1.5 mm for case 3, with M ranging from 0.5 to 2.0. Figure 6.13 shows predicted and measured capture efficiencies. It is clearly seen that the predictions at M=1.0 and 2.0 agreed well with the experimental measurements. At M=0.5, the predicted capture efficiency was higher than the measured value. The exact cause for this discrepancy is not known, but is thought to be caused by the differences between predicted and actual surface temperatures for this case. Note that the capture efficiencies for this case were much lower than for case 1 (shown in Figure 6.10), which trend was accurately modeled.

A comparison of laterally-averaged cooling effectiveness between cases 2 and 3 is shown in Figure 6.14. For case 3, the effectiveness increased at the location close to the ejection of the cooling holes until a maximum value appears at y/d=2 where the best surface coverage was obtained. Downstream of this location, effectiveness began to decay due to the entrainment of hot gas, which seemingly overweighs the beneficial effect attained by the increased film cooling coverage. At M=0.5, the peak was not obvious, compared with the other two blowing ratios. It is likely that the coolant jet was spread on the surface immediately after exiting the holes. Due to the decrease of coolant flow rate, the coolant was readily entrained by the mainstream and resulted in a relatively-small peak. Figure 6.14 also shows that the effectiveness provided by a large hole was larger than from small holes, which was due to the increase of flow rate.

Centerline film cooling effectiveness is shown in Figure 6.15. The cooling effectiveness decreased with decreasing blowing ratio, and case 3 had larger cooling effectiveness than case 2. However, the peaks did not appear in the region close to the holes as did the spanwise averaged effectiveness shown in Figure 6.14. The increase of coolant flow rate for case 3 slowed down the effectiveness decay downstream of the cooling holes.

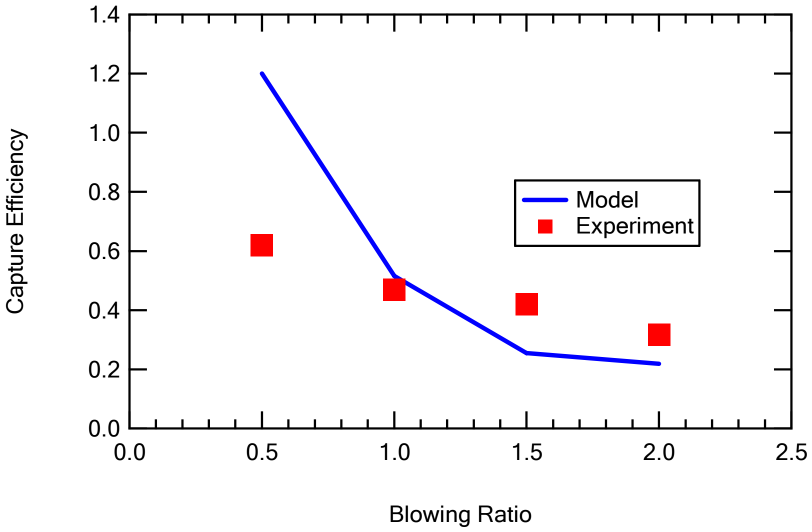

Figure 6.13 Predicted and measured capture efficiencies at M=0.5 to 2.0 for a hole size of d=1.5 mm (Case 3, s/d = 3.0)

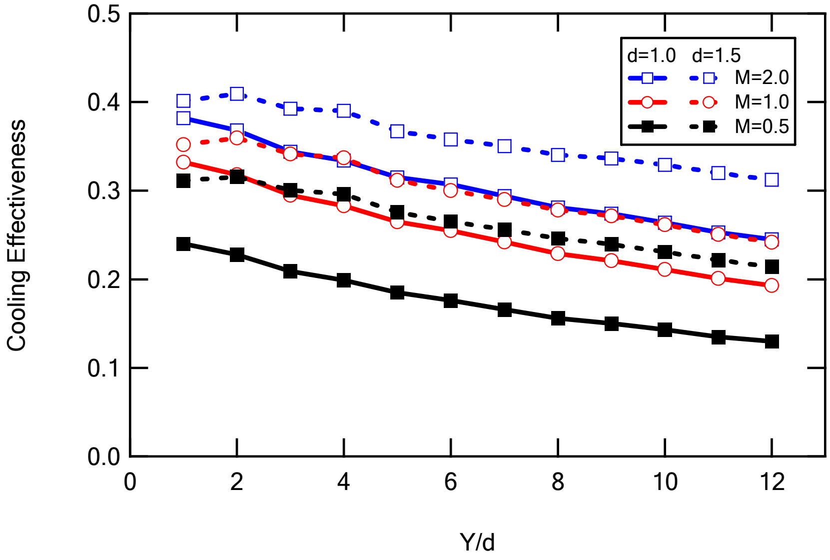

Figure 6.14 Laterally averaged film cooling effectiveness with M= 0.5 to 2.0 for Case 2(d=1 mm) and Case 3 (d=1.5 mm).

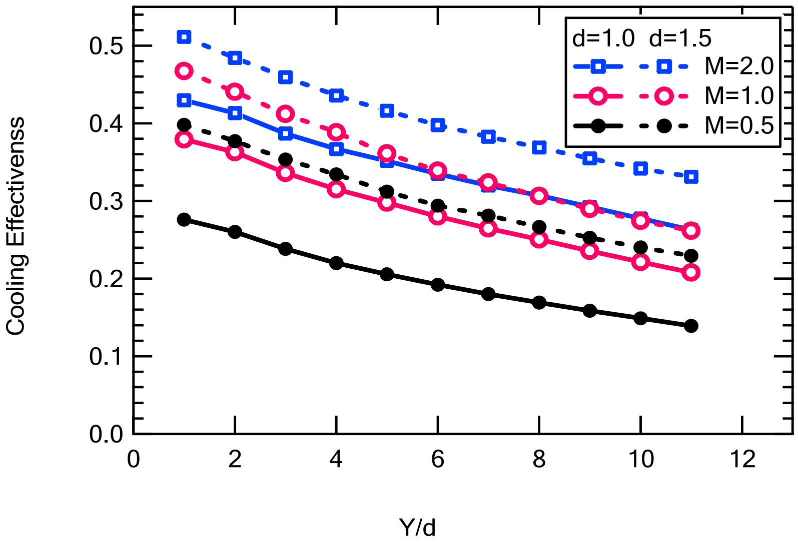

Figure 6.15 Centerline film cooling effectiveness with the variation of M from 0.5 to 2.0 for Case 2(d=1 mm) and Case 3 (d=1.5 mm)

The flow field results computed for M=0.5 to 2.0 for cases 2 and 3 are shown in Figure 6.16. The computed velocity magnitude contours were obtained along the centerline plane (y=0) and their scales were different. Velocity gradients in the cooling-hole passage were apparent in each case. The exit velocity from the large holes was less than that from the small holes, due to a slight difference in predicted gas temperature at the hole exit. The large hole case had a higher coolant mass flow rate to maintain the same blowing ratio. Jet penetration into the region just above the hole exit and slightly downstream was greater for the larger diameter hole-case. The formation of a boundary layer is more apparent for the M=1.0 and 0.5 cases. Vertical slices of the gas temperature distribution near the center cooling hole at a downstream location of X/d = 2 are shown

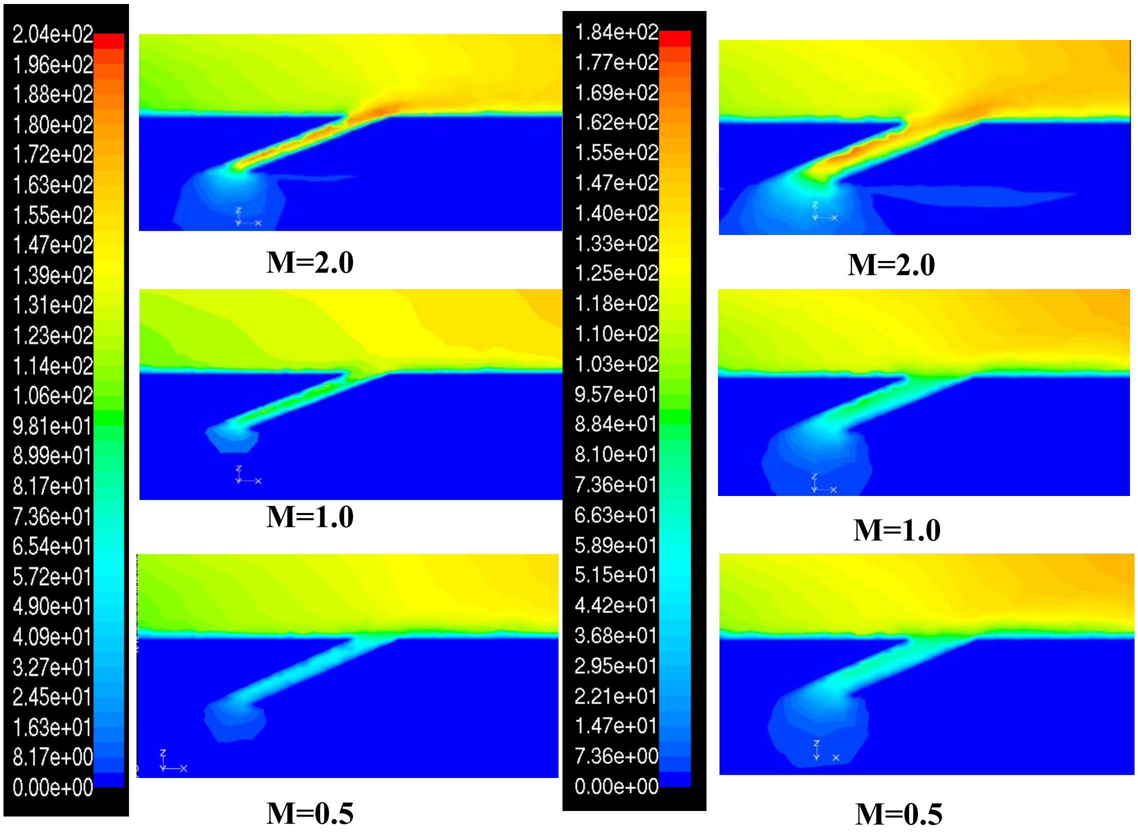

(a) d=1 mm, s/d=4.5 (b) d=1.5 mm, s/d=3

Figure 6.16 Velocity magnitude contours (m/sec) with blowing ratio from 0.5 to 2.0 along centerline plane for case 2 and 3

in Figure 6.17 for cases 2 and 3. The jet lift-off can be observed to occur at M=2.0 for case 3 (Figure 6.17b), since the low temperature core of the jet was lifted slightly above the coupon surface. The temperature map just downstream of the small hole simulation (Figure 6.17a) shows that the coolant jet core was closer to the wall and avoided lift-off.

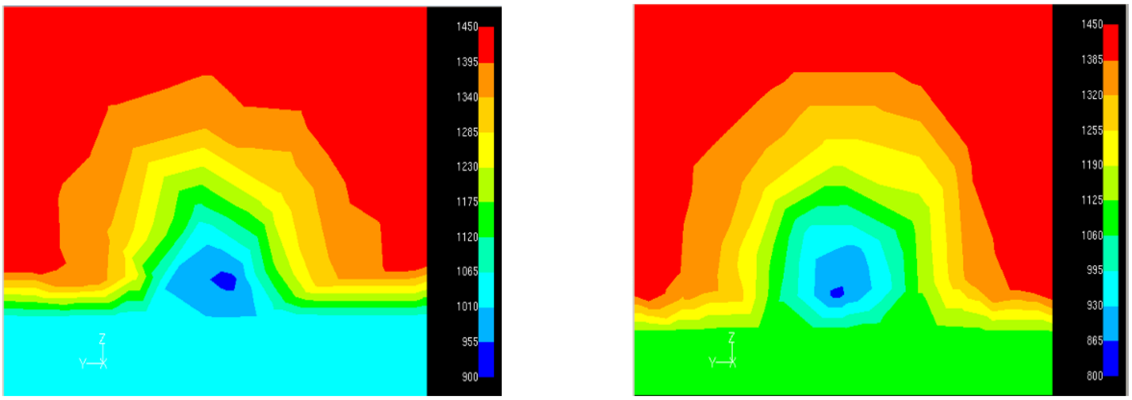

(a) d=1.0 mm, s/d=4.5, M=2.0 (case 2)   (b) d=1.5 mm, s/d=3.0, M=2.0 (case 3)

Figure 6.17 Gas temperature distribution in X/d=2 for case 2 and 3. Temperatures are in Kelvin

6.4.4.3 Effect of conjugate heat transfer

This section discusses the predicted effect of conjugate heat transfer. The thermal conductivity of the plate was set to a value close to zero for the adiabatic conditions. Cases 4 and 5 are the adiabatic simulations corresponding to cases 2 and 3 with M=1.0. Comparison of the adiabatic cases with the conjugate heat transfer cases shows the influence of heat transfer through the coupon on the film cooling effectiveness.

Figure 6.18 compares the temperature contours of the entire hot surface for the adiabatic and conjugate conditions (cases 2 and 4) before ash deposition. For the adiabatic case, the surface temperature approached the hot gas temperature except in the flow paths of the coolant jets. Low surface temperatures were observed near the hole exits. When conjugate heat transfer was taken into account, the average surface temperature was significantly lower than the adiabatic wall case, especially in the regions outside of the cooling flow channels. In the conjugate case, the low temperature region upstream of the cooling holes was indicative of the effect of internal cooling. The decrease in the entire surface temperature was caused by both film cooling and internal cooling from backside impingement on the coupon.

The coolant channel Figure 6.18 was not apparent for the conjugate case, which simulated the bare metal coupon experiments. In Figure 6.18c, the coolant passages appear more clearly with the elapsed time and extent of particle deposition. The temperature history suggests that clean coolant dominated the initial deposition process by blowing off the particles and preventing particles from impacting on the surface. Initial deposits mainly formed between coolant channels. Due to increasing deposit surface temperature, subsequent deposition occurred on top of initial deposits, which led to the formation of distinct ridges between coolant paths.

In Figure 6.19 the laterally-averaged film cooling effectiveness is plotted versus the distance downstream of the cooling holes for cases 4 and 5. It is apparent that the conjugate case had a higher value presenting a better cooling performance than the adiabatic case for both hole diameters. An effectiveness peak appeared at the location of Y/d=1.0 for cooling holes with large sizes. Effectiveness for the adiabatic case decayed more rapidly than for the conjugate case. The reason is the temperature increase of the hot surface in the region far downstream of the holes. For the conjugate condition case, the temperature increase was suppressed by the internal cooling.

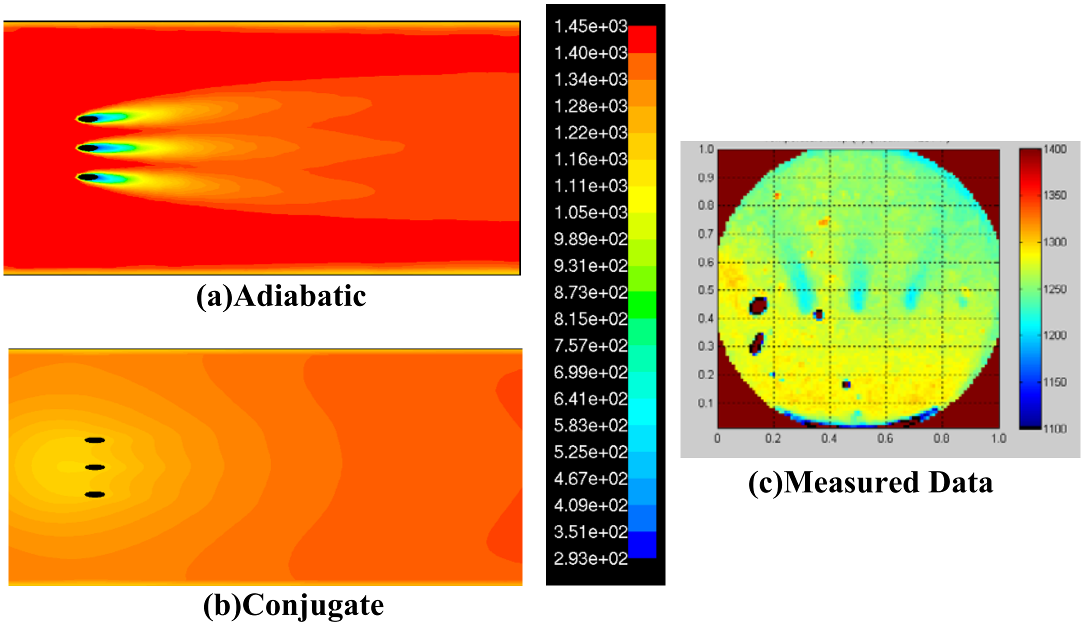

(a)Adiabatic

(b)Conjugate

(c)Measured Data

Figure 6.18 Surface temperature profiles of the coupon surface for M=1.0 from (a) adiabatic case predictions; (b) conjugate case predictions; (c) Measured data with conjugate case after 20 minutes deposition test. Hole diameters were 1.0 mm. Temperatures are in Kelvin

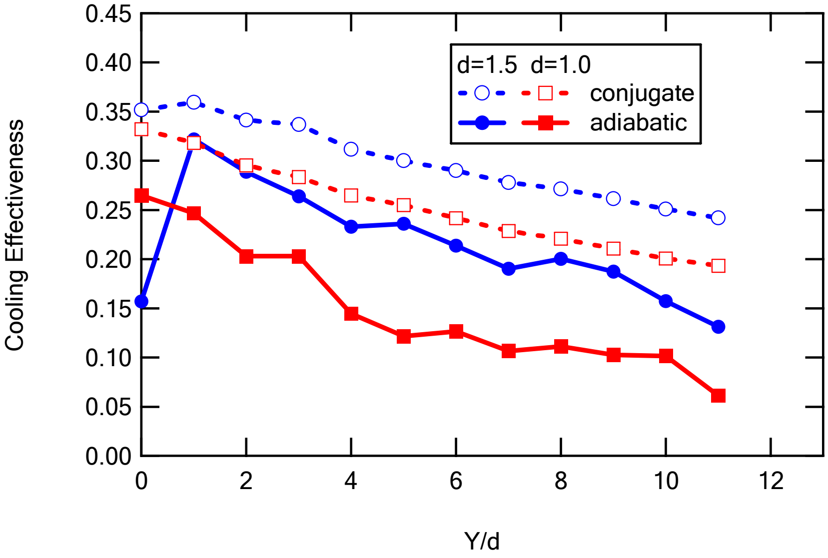

Figure 6.19 Laterally averaged film cooling effectiveness at M=1.0 for adiabatic and conjugate cases

Figure 6.20 presents centerline film cooling effectiveness at M=1.0 by comparing the adiabatic case with the conjugate heat transfer case. In the adiabatic condition, the coolant jet was not heated up by the plate wall before exiting the hole and, hence, maintained the coolant inlet temperature. Therefore, the cooling effectiveness approached 1.0 at the exit of the holes. However, a rapid decay of the effectiveness is shown downstream of the holes as the mainstream hot gas entrained with the coolant in the film. In the conjugate condition, the coolant was heated as it impinges on the cooler side of the coupon. Additional heat transfer occurred during passage through the holes, which led to an additional temperature increase compared to the adiabatic condition. As a result, the film cooling effectiveness at the exit of the jet is 0.4 to 0.5, much lower than the adiabatic condition. Due to a slower decay, the conjugate condition outperformed the adiabatic cases at a distance Y/d >8 for d = 1 and greater than 12 for d = 1.5.

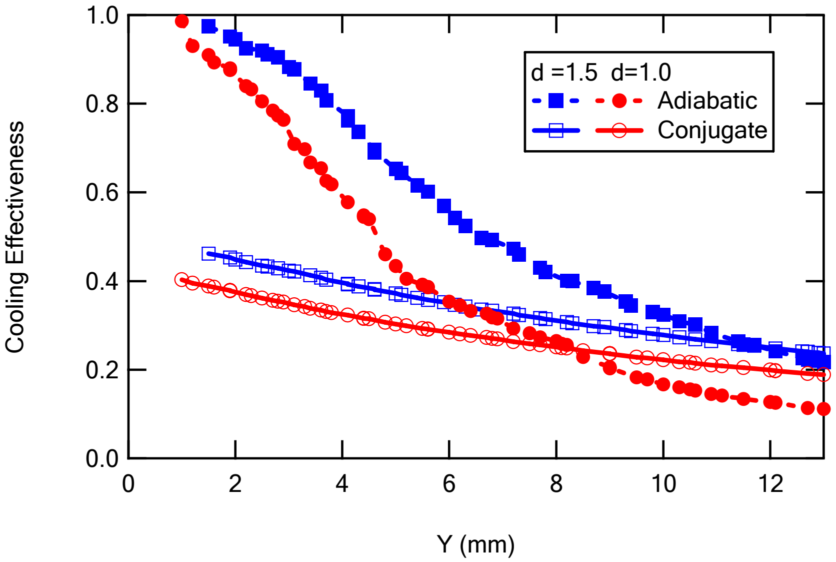

Figure 6.20 Centerline effectiveness at M=1.0 for adiabatic and conjugate case

In the conjugate heat transfer condition, the convective heat load to the hot coupon surface is given by:

$$q'' = h(T_{aw} - T_w) \tag{6-15}$$

where T_{aw} is the surface temperature at each location from the adiabatic prediction. Figure 6.21 illustrates the change in the heat transfer coefficient along the distance downstream of the film cooling hole for different hole-sizes. Generally, a cooling jet injected into a mainstream flow generated high levels of turbulence, which increased the local convective heat transfer coefficient. This trend dwindled with the further mixing of the mainstream. Therefore, the heat transfer coefficient at the location close to the jets was at a maximum value of 240 W/ ($m^2 \cdot K$). On account of the lower temperature of coolant directly downstream of the hole exit, the coolant had a lower temperature than the surface temperature, so heat was transferred from the surface to the coolant. Further downstream, coolant mixed with the hot gas, and the gas mixture near the surface was heated up to a higher temperature than the surface. Heat was then transferred from the gas to the wall. The positive heat transfer coefficient shown in Figure 6.21 indicates that heat flowed from the wall to the coolant stream. At $Y/d<7$, the values of the heat transfer coefficient for holes with small and large sizes were similar, while at the further distances, the values of h for large holes decayed more rapidly than for the smaller hole case.

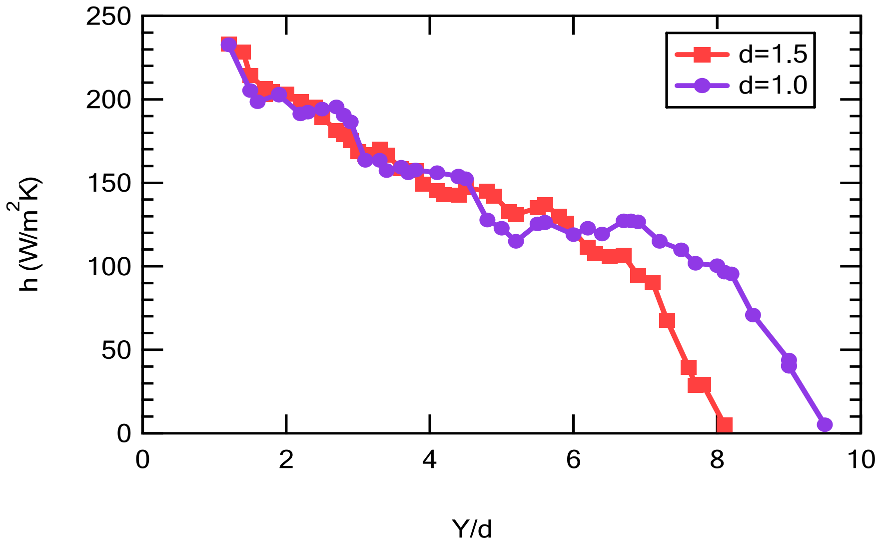

Figure 6.21 **Centerline conjugate heat transfer coefficient for cases 2 and 3 with M=1.0**

6.4.4.4 TBC effect (d=1.0 mm, s/d=4.5)

A TBC layer with a thickness of 0.25 mm was added to the coupon surface, and the thermal conductivity (k) of the TBC layer was set to 1.78 W/m·K for case 6 and 0.3 W/m·K for case 7. Predictions were performed to examine the effect of a TBC layer on the metal surface temperature. A comparison of predictions obtained for cases 2, 4, 6 and 7 is shown in Figure 6.22 and Figure 6.23. Note that with the addition of an insulating TBC layer (Case 6), the centerline and laterally-averaged surface temperature along the centerline was reduced 50 K, compared to the case without TBC. However, with the thermal conductivity decreasing from 1.78 W/(m^2 ·K) to 0.3 W/(m^2 ·K), metal surface temperature did not continue to increase but instead had an increase of 40 K, still less than the surface temperature from the case without TBC. This simulation result of first decreasing then increasing surface temperature with decreasing thermal conductivity coincided with Na's study (2007). When k=0, the temperature curve in Figure 22 crossed the curves from the other cases and elevated to a higher temperature than that of the other cases at location Y/d>5. Experiments to study the effect of TBC show that the measured surface temperature for the TBC coupon was higher than that of the bare metal coupon. The temperature map was measured after a few minutes in the deposition test, so that the TBC surface had already captured some fine particles. Since the thermal conductivity of ash is as low as 0.1 to 0.2 W/(m·K) (Robinson et al., 2001), the coupon thermal resistance was close to the adiabatic condition, possibly resulting in a surface temperature that was higher than that in the same experiment with a bare metal surface. The increase of surface temperature sped up the deposit formation and further deteriorated conductive heat transfer.

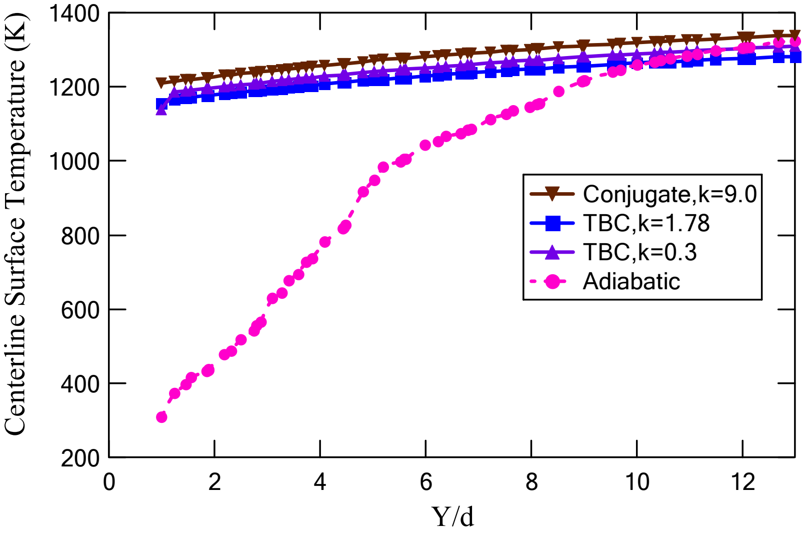

Figure 6.22 Centerline surface temperature for M=1.0 with a TBC layer and different values of thermal conductivity

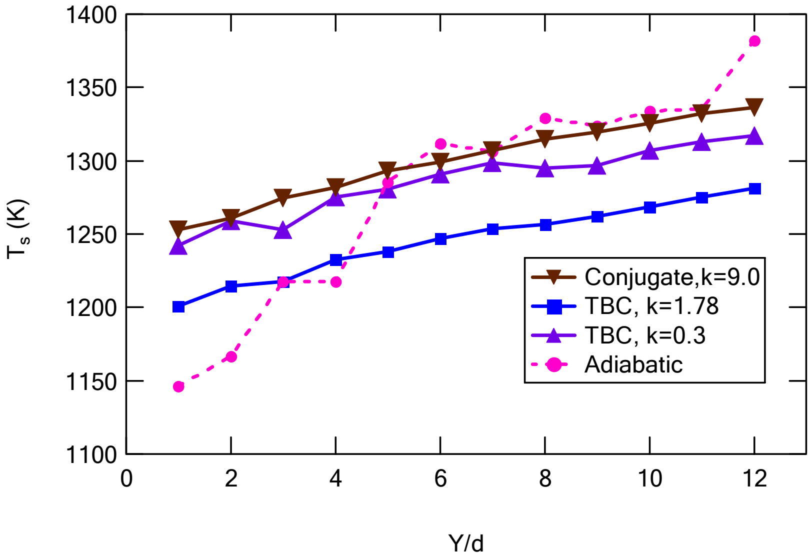

Figure 6.23 Laterally averaged surface temperature for M=1.0 with a TBC layer with different values of thermal conductivity

The corresponding surface temperature contours for the four cases with varying thermal conductivity are shown in Figure 6.24. The distinct coolant channels in the adiabatic case indicate that the freestream did not mix with the coolant stream very well in the region directly close to the coolant exit. Weak coolant channels appeared downstream of the cooling holes for the conjugate TBC cases, but not for the conjugate case without TBC. However, deposit patterns (Figure 5.9) obtained from experiments show the distinct furrows. Since the predicted surface temperature variation in the conjugate TBC simulations was low, and since distinct furrows of deposits were seen in the experiment, it appeared that the momentum of the coolant jets played a significant role in changing the flowfield in the layer near the surface and prevented particles from impacting on the surface.

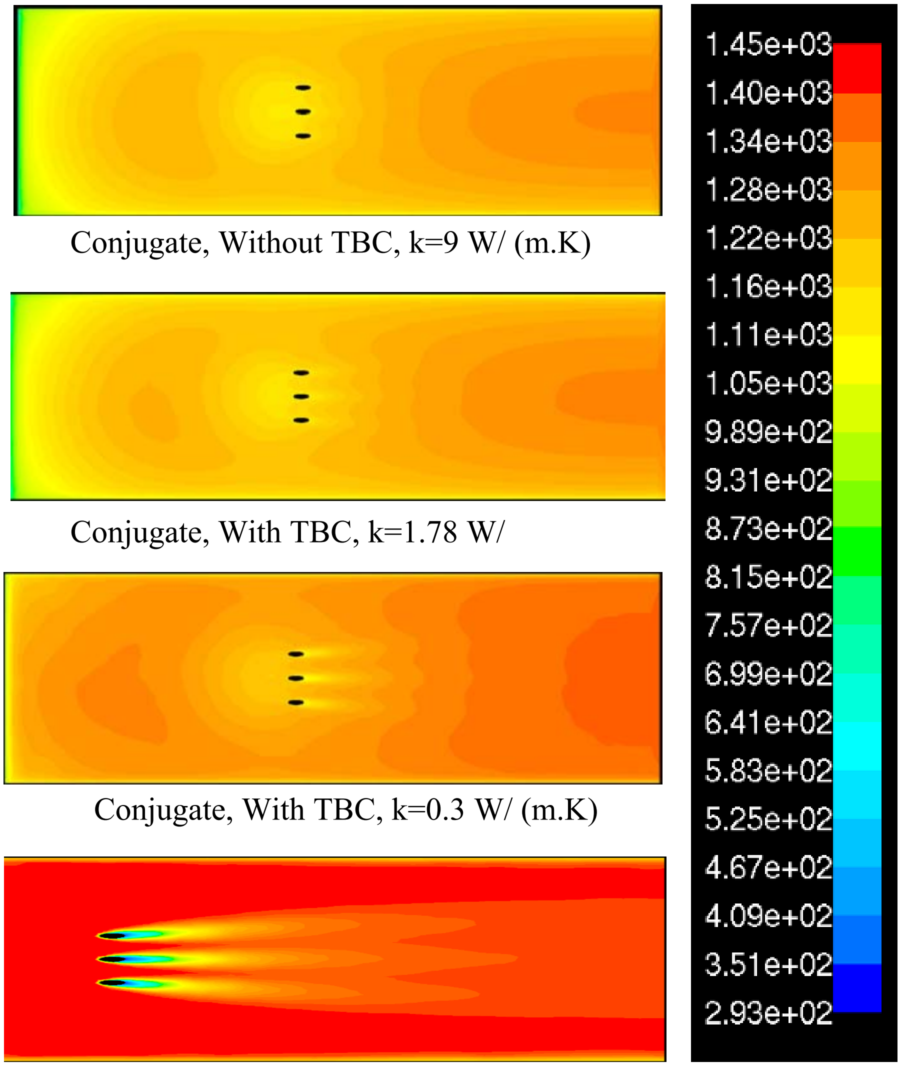

Conjugate, Without TBC, k=9 W/ (m.K)

Conjugate, With TBC, k=1.78 W/

Conjugate, With TBC, k=0.3 W/ (m.K)

Adiabatic

Figure 6.24 Surface temperature contour for M=1.0 with or without a TBC layer with different values of thermal conductivity

6.4.5 Summary of Modeling Results

To specify the effect of hole-size and hole spacing on the flow field and heat transfer quantatively, a 3-D numerical model was developed for three cases: (a) adiabatic, (b) conjugate heat transfer and (c) a TBC layer. A series of experiments was designed and performed to obtain the particle Young's Modulus (E_p) in a 2-D model, which determined the capture velocity of particles for the 3-D computation. The results show that large particles had a higher delivery rate than small particles, while small particles more readily stuck to the surface. For a given particle size, the capture efficiency increased with gas temperature.

The film cooling effectiveness for the case with large size holes outperformed the case with small size holes along the centerline and in the spanwsie direction. An optimum cooling effectivness appeared at a location downstream, close to the large holes, indicating jet lift-off.

The computation for the case of conjugate heat transfer indicated the significance of backside coolant impingement on the overall heat transfer, especially in the region far from the cooling holes. The computational results from the simulation of a TBC coupon were in good agreement with the corresponding measurements, in that the TBC enhanced the deposition and that the increased surface termperature sped up the subsequent deposition.

7. Conclusions and Recommendations

Several series of tests were performed in an accelerated deposition test facility by matching gas temperature, velocity, and net throughput of particulate out of the combustor with those typical of by a modern power turbine. Nominal combustor exit flow conditions were $\mathcal{M}$ = 0.25 and a gas temperature of 1183°C. These key factors include blowing ratio, hole-shape, hole spacing, particle size, TBC and trench configuration. In the experiments, the sample surface temperature was measured quantitatively by two-color pyrometry based on the RGB signals from a camera. Post-test samples were analyzed and qualitative and quantitative results were obtained. The experiments were modeled by using computational fluid dynamics (CFD) with appropriate boundary conditions. Predictions were made of capture efficiency, film cooling effectiveness, and heat transfer coefficient.

7.1 Conclusions from Experiments

Both cylindrical holes and shaped holes were investigated using uncoated and TBC coupons. The images taken after 4-hour deposition tests at blowing ratios ranging from 0.5 to 2.0 show that the deposits formed ridges between the cooling holes downstream of coolant injection, forming coolant ejection channels which deviated slightly from the streamwise direction, especially at low blowing ratios. The capture efficiency decreased 50% as blowing ratio changed from 0.5 to 2.0. Surface temperature maps after a few minutes in the deposition test confirmed that the ridges between cooling holes were hotter than the coupon surface in the coolant flow path. The difference in temperature between the deposit ridges and the surface in the coolant path increased with increasing deposition.

In the tests on a shaped-hole coupon, no significant deposits were formed downstream of these cooling holes. Images of deposits from these tests showed that the shaped holes have more spanwise coverage than the cylindrical holes. The capture efficiency for shaped holes was 25% lower than for cylindrical holes at M = 2.0. Some of the lack of deposition for the shaped holes may be due to the small spacing between the exits of the shaped holes in the coupon used for these tests. The enlarged coolant coverage caused by the clean coolant may protect more surface area from particle impact.

One-hour tests on TBC coupons with a spacing of 4.5d presented significant amounts of deposit over the sample surface. At the lowest blowing ratio studied (M = 0.5), the deposit formed around the film cooling holes, partially blocking the holes and resulting in higher surface temperatures. At M = 2.0, the deposition pattern downstream of the cooling holes on TBC coupons became more defined, with troughs in the cooling hole wake and ridges between cooling holes. Measured front-side surface temperatures after deposition exhibited non-uniform profiles that matched the ridges and troughs visible in the deposit pattern. The non-uniformity in temperature increased with deposit thickness and with blowing ratio. As the deposit layer on the surface grew, the deposit height and surface temperature increased, which enhanced capture for additional particles. The growth rate of deposits was shown to be non-linear with time, with high growth rates at the longest times. The high velocity coolant seems to play an important role in deposition variation across the surface by protecting the surface from high temperature gas and particle deposition in the coolant channels. This effect increases with increasing blowing ratio and coolant momentum.

The capture efficiencies measured for the TBC experiments were higher than for the bare metal coupons for the same gas temperatures and blowing ratios. The coupon surface temperature at steady state was higher for the TBC coupon tests, as expected, due to the thermal resistance of the coating and initial ash deposit layer. The increase surface temperature of the TBC coupons enhanced the particulate capture efficiency.

The deposition experiments on a TBC coupon with close hole spacing (2.25d,5 holes) showed a much more uniform low temperature region downstream of the cooling holes and much lower deposition than with the large hole spacing (4.5d,3 holes). The lower deposition was due to the fact that the cooling flow rate is 5/3 higher in the 5-hole test than in the 3-hole test. The enhanced cooling flow rate results in a lower surface temperature due to the coolant impingement on the backside of the coupon. Less deposit flaked off the TBC coupon during cool down than for the bare metal coupon tests, implying that deposits on the TBC coupon were less affected by thermal stresses during cool down, possibly due to the physical structure of the TBC.

Experiments to examine the effects of hole spacing using bare metal coupons showed that the average spanwise surface temperature for close hole spacing was only slightly lower than for the large hole spacing. Closer hole spacing decreased capture efficiency, but the major effect on particle deposition seemed to be blowing ratio (and hence surface temperature). The roughness analysis shows that Ra and Rt decreased monotonically with increasing blowing ratio for both values of hole spacing. The roughness for s/d = 3.375 was lower than that for s/d = 4.5, especially at high blowing ratio. Spanwise temperature profiles showed the highest peak-to-valley differences for blowing ratios of 1.0. Measured streamwise surface temperatures downstream of the middle hole did not always show the expected increase with distance from the hole, but were rather flat in some cases, indicating that additional heat transfer processes such as backside-impingement cooling are significant at the higher blowing ratios.

Two sets of particles (with mean diameters 4 μm and 13 μm) were tested to examine the effects of particle size on the deposition near film-cooling holes. The measured capture efficiency indicated that small particles were less inclined to deposit than larger particles, especially at low blowing ratios. However, the smaller particles were found to stick on the surface more tenaciously, and were more sensitive to surface temperature variations, resulting in the deposit ridge formation. The smaller particles exhibited a greater variation in deposition pattern as a function of hole spacing than seen with larger particles.

A trench with an optimal width value of 2.5 mm and depth value of 0.75 mm was used to test deposition effects. The impingement angle had a significant effect on deposition when the angle was varied from 45° to 15°. Measured spatial temperature distributions indicated that a shallow impingement angle mitigated the influence of mainstream gas flow penetrating the trench and changing film-cooling characteristics. At the shallow impingement angle, the upstream wall blocked the mainstream entrainment upstream holes and enabled the coolant to more readily spread laterally and enhance film cooling effectiveness.

Trench tests conducted at an impingement angle of 30° suggest although the increased cooling effectiveness reduced deposition downstream, the capture efficiency was not improved because the trench became a particulate collector. Deposits accumulated on the downstream side of the trench between cooling holes, eventually changing the geometry of the trench and clogging cooling holes. Measured surface temperature distributions demonstrated that the trench increased the coolant coverage and reduced the downstream metal surface temperature for $M \geq 1.0$. However, the trench also decreased the coolant momentum ratio and impaired the effectiveness of individual coolant jets, which at low blowing ratios, resulted in lower cooling performance than the case with no trench.

7.2 Modeling Conclusions

3-D numerical simulations of film cooling fluid injection through a row of different-sized cylindrical holes distributed at varying hole spacing were performed using FLUENT at blowing ratios from 0.5 to 2.0. Simulations used RANS and the k-ω turbulence model to compute the flow field and heat transfer to a metal coupon for three cases: (a) adiabatic, (b) conjugate heat transfer and (c) a TBC layer. The boundary conditions were set to be those measured in an experimental facility (the TADF). Comparisons of film cooling effectiveness and heat transfer coefficients were presented to illustrate the effects of hole-size, hole spacing, conjugate heat transfer and TBC layer on film cooling heat transfer.

A 2-D Lagrangian model was developed to determine a correlation for the particle Young's Modulus (E_p) for this system by comparing deposition capture efficiency from temperature-dependent experiments performed as part of this project. This correlation was then used in 3-D computations of ash particulate deposition for experiments with film cooling at different blowing ratios. User-defined subroutines were developed to describe particle sticking/rebounding and particle detachment on the impinged wall surface. Results from the 2-D deposition model indicated that the small particles had a greater tendency to stick to the surface in the TADF experiments. After the initial deposition, and as the surface of the deposit rose above the transition temperature, large particles dominated the excessive deposition due to the high delivery rate, which was in agreement with the experimental results.

Predictions with the 3-D deposition model agreed well with measured capture efficiencies for most of blowing ratios and different hole-sizes. Capture efficiency decreases with increased blowing ratio and increased hole-size (when blowing ratio is held constant).

Predictions from a 3-D film cooling model with different hole spacings (s/d=3.4 and 4.5) indicated that the averaged spanwise and centerline cooling effectiveness rose with the increase of blowing ratio. The cooling effectiveness at locations close to the exit of jets for wide hole spacing was slightly higher than for small hole spacing. Meanwhile, the small hole spacing performed better than wide hole spacing at downstream locations due to the interaction of neighboring jets. The larger hole (1.5 mm) provided better cooling than a small hole (1 mm) based on centerline and averaged spanwise film cooling effectiveness. A small peak in the cooling effectiveness curve appeared just downstream of the large holes, indicting jet lift off, especially at high blowing ratios.

Conjugate heat transfer calculations suggested that backside-impingement cooling in the TADF experiments improved the overall cooling effectiveness, especially in the region far downstream of the cooling holes. The centerline heat transfer coefficient was predicted to decrease with distance downstream of the holes. Combined with the measured frontside temperature map development with time, the predicted surface temperature map for the adiabatic case indicates that the clean coolant stream diluted the particle concentration in the coolant channels and dominated the initial deposit variation. Increasing temperature variation caused by deposit formation between flow channels was responsible for the subsequent generation of deposit ridges between coolant passages. The predicted temperature contours for the conjugate case showed little change in surface temperature in the flow channels. This low-temperature variation implies that ejected coolant changed the flow field in the region downstream cooling holes and diluted the particle concentration, resulting in the reduction of particles that impacted the surface in the initial deposition. Initial deposits formed between coolant channels. Subsequent deposition occurred on top of initial deposits, due to increasing deposit surface temperature, which led to the formation of distinct ridges between coolant paths.

The addition of a TBC layer effectively reduced the outer surface temperature initially. As a thin ash deposition layer formed with low thermal conductivity, the thermal resistance layer ultimately increased the outer surface temperature.

7.3 Recommendations

The project examined deposition of ash particulate from coal-derived syngas on sample coupons with differing configuration parameters. The conclusion is informative and insightful. Nevertheless, to understand fully the mechanism of ash deposition on gas turbine systems and provide the more useful data for designers, some of the recommendations for future investigation are listed below.

1. In the testing on metal coupon with TBC (**TBC** and **M4**), it would be nice to measure the metal surface interfacial temperature for the TBC coupon. Alternatively this could be computed accurately by analyzing the conductive heat transfer through the sample. This type of data would provide a comparison to assess the effect of the TBC layer and deposition layer on the metal surface temperature as a function of time.
2. The effect of impingement angle on particulate deposition should be further investigated. The global surface temperatures at the rear and front sides of the sample should be kept approximately the same when varying impingement angle in future tests.
3. A laser-based technique should be developed to measure deposition thickness *in situ*. This would help compute the local heat flux over the sample surface and assist in understanding the transient variation of surface heat transfer.
4. The facility should be modified to increase the temperature of the combustor exit to 1400°C for exploring turbine endwall geometries.
5. The Young's Modulus Number was tuned using experimental results as a function of temperature, which is one parameter in determining particle capture velocity. Particle size and flow field were also included in the calculation. The capture efficiency obtained in the numerical model is the result of all of these factors. Further research should be conducted to assess which process is dominant. Therefore, additional computations should be made to compare the

capture efficiencies at different blowing ratios, hole spacings, and particle sizes, while holding the average surface temperature constant.

6. In the deposition model, the eddy impaction deposition mechanism was ignored. A better model should be developed in future work to describe deposit build-up for small particles in the layer close to the surface due to eddy impaction. The effect of the deposition layer on the aerodynamic drag and on the film-cooling heat transfer was not treated. The deposition generates a fouled surface as a function of time. Numerical computation of a fouled surface would provide insight into the deposition development and variation of heat transfer with surface roughness and thermal conditions.

8. References

"Fluent 6.2 User Guide," Fluent Inc (2005).

Ajersch, P., J.-M. Zhou, S. Ketler, M. Salcudean and I. S. Gartshore, "Multiple Jets in a Crossflow: Detailed Measurements and Numerical Simulations," IGTI, Houston, TX, USA, ASME-95-GT-9 (1995).

Andreini, A., C. Carcasci, S. Gori and M. Surace, "Film Cooling System Numerical Design: Adiabatic and Conjugate Analysis," 2005 ASME Summer Heat Transfer Conference, HT 2005, San Francisco, CA, United States, 3 (2005).

Asok Kumar, N. and S. R. Kale, "Numerical Simulation of Steady State Heat Transfer in a Ceramic-Coated Gas Turbine Blade," *International Journal of Heat and Mass Transfer,* **45**(24), 4831-4845 (2002).

Baldauf, S., M. Scheurlen and A. Schulz, "Correlation of Film-Cooling Effectiveness from Thermographic Measurements at Engine-Like Conditions," *Journal of Turbomachinery,* **v124**(4), p686-698 (2002).

Balduaf, S., A. Schulz and S. Wittig, "High-Resolution Measurements of Local Heat Transfer Coefficients from Discrete Hole Film Cooling," *Journal of Turbomachinery,* **123**(4), 749-757 (2001).

Barlow, D. N. and Y. W. Kim, "Effect of Surface Roughness on Local Heat Transfer and Film Cooling Effectiveness," IGTI, Houston, Texas,US, 95-GT-14 (1995).

Bohn, D., J. Ren and K. Kusterer, "Conjugate Heat Transfer Analysis for Film Cooling Configurations with Different Hole Geometries," IGTI, Atlanta, GA, 2003-GT-38369 (2003).

Bons, J. P., R. P. Taylor and S. T. McClain, "The Many Faces of Turbine Surface Roughness," *Journal of Turbomachinery,* **v123**(4), p739 (2001).

Bons, J. P., J. Crosby, J. E. Wammack and B. I. Bentley, "High-Pressure Turbine Deposition in Land-Based Gas Turbines from Various Synfuels," *Journal of Engineering for Gas Turbines and Power,* **v129**(1), p135-143 (2007).

Brach, R. and P. Dunn, "A Mathematical Model of the Impact and Adhesion of Microspheres," *Aerosol Science and Technology,* **16**(1), 51-64 (1992).

Brittingham, R. A. and J. H. Leylek, "A Detailed Analysis of Film Cooling Physics: Part Iv - Compound-Angle Injection with Shaped Holes," *Journal of Turbomachinery,* **v122**(1), p133-145 (2000).

Brown, A. and C. L. Saluja, "Film Cooling from a Single Hole and a Row of Holes of Variable Pitch to Diameter Ratio," *International Journal of Heat and Mass Transfer,* **22**(4), 525-534 (1979).

Bunker, R. S., "Effect of Partial Coating Blockage on Film Cooling Effectiveness," IGTI, Germany, 2000-GT-0244 (2000).

Bunker, R. S., "Film Cooling Effectiveness Due to Discrete Holes within a Transverse Surface Slot," IGTI, Amsterdam, Netherlands, GT2002-30178 (2002).

Bunker, R. S., "A Review of Shaped Hole Turbine Film-Cooling Technology," *Journal of Heat Transfer,* **v127**(4), p441 (2005).

Cardwell, N. D., N. Sundaram and K. A. Thole, "Effects of Mid-Passage Gap, Endwall Misalignment and Roughness on Endwall Film-Cooling," IGTI, Reno-Tahoe, Nevada, USA, GT2005-68900 (2005).

Crosby, J. M., "Particle Size, Gas Temperature, and Impingement Cooling Effects on High Pressure Turbine Deposition in Land Base Gas Turbine from Various Synfuels," MS Thesis, Department of Mechanical Engineering, Brigham Young University (2007).

Crosby, J. M., W. G. Ai, S. Lewis, T. H. Fletcher and J. P. Bons, "Effects of Particle Size, Gas Temperature, and Metal Temperature on High Pressure Turbine Deposition in Land Based Gas Turbines from Various Synfuels," IGTI, Montreal, Canada, GT2007-27531 (2007).

Davies, C. N., "Deposition from Moving Aerosols," In Aerosol Science, Academic Press (1966).

Demling, P. and D. G. Bogard, "The Effects of Obstructions on Film Cooling Effectiveness on the Suction Side of a Gas Turbine Vane," IGTI, Barcelona, Spain, GT2006-90577 (2006).

Dorrington, J. R., D. G. Bogard and R. S. Bunker, "Film Effectiveness Performance for Coolant Holes Embedded in Various Shallow Trench and Crater Depressions," IGTI, Montreal, Canada, GT2007-27992 (2007).

Drost, U., A. Bolcs and A. Hoffs, "Utilization of the Transient Liquid Crystal Technique for Film Cooling Effectiveness," IGTI, Orlando, FL, USA, 97-GT-26 (1997).

Ekkad, S. V., D. Zapata and J. C. Han, "Film Effectiveness over a Flat Surface with Air and CO2 Injection Through," *Journal of Turbomachinery,* **v 119**(21), p 587-593 (1997).

El-Batsh, H. and H. Haselbacher, "Numerical Investigation of the Effect of Ash Particle Deposition on the Flow Field through Turbine Cascades," IGTI, Amsterdam, Netherlands, GT-2002-30600 (2002).

Friedlander, S. K. and H. F. Johnstone, "Deposition of Suspended Particles from Turbulent Gas Streams," *Industrial & Engineering Chemistry,* **v 49**, p1151-1157 (1957).

Ghenaiet, A., S. C. Tan and R. L. Elder, "Prediction of an Axial Turbomachine Performance Degradation Due to Sand Ingestion," Proceedings of the Institution of Mechanical Engineers, Part A: Journal of Power and Energy, v 219 (2005).

Goldstein, R. J., E. R. G. Eckert and F. Burggraf, "Effects of Hole Geometry and Density on Three-Dimensional Film Cooling," *International Journal of Heat and Mass Transfer,* **v 17**(3), p 595-607 (1974).

Goldstein, R. J., E. R. G. Eckert, H. D. Chiang and E. Elovic, "Effect of Surface Roughness on Film Cooling Performance," *Journal of Engineering for Gas Turbines and Power,,* **107**, 111-116 (1985).

Greenfield, C. and G. Quarini, "Particle Deposition in a Turbulent Boundary Layer, Including the Effect of Thermophoresis," Proceedings of ASME Fluids Engineering Division Summer Meeting, FEDSM'97. Part 17 (of 24), Vancouver, Can, 17 (1997).

Gritsch, M., A. Schulz and S. Wittig, "Adiabatic Wall Effectiveness Measurements of Film-Cooling Holes with Expanded," IGTI, Orlando, FL, USA, 97-GT-164 (1997).

Gritsch, M., A. Schulz and S. Wittig, "Heat Transfer Coefficient Measurements of Film-Cooling Holes with Expanded," Proceedings of the 1998 International Gas Turbine & Aeroengine Congress & Exhibition,ASME, 98-GT-28 (1998).

Haller, B. R. and J. J. Camus, "Aerodynamic Loss Penalty Produced by Film Cooling Transonic Turbine Blades," IGTI, 83-GT-77 (1983).

Harrison, K. L. and D. G. Bogard, "CFD Predictions of Film Cooling Adiabatic Effectivness for Cylindrical Holes Embedded in Narrow and Wide Transverse Trenches," IGTI, Montreal, Canada, GT2007-28005 (2007).

Harrison, K. L. and D. G. Bogard, "Comparison of Rans Turbulence Models for Prediction of Film Cooling Performance," IGTI, Berlin, Germany, GT2008-51423 (2008).

Hoda, A. and S. Acharya, "Predictions of a Film Coolant Jet in Crossflow with Different Turbulence Models," *Journal of Turbomachinery, Transactions of the ASME,* **122**(3), 558-569 (2000).

Hyams, D. G. and J. H. Leylek, "A Detailed Analysis of Film Cooling Physics: Part Iii - Streamwise Injection with Shaped Holes," *Journal of Turbomachinery,* **122**(1), 122-132 (2000).

Jensen, J. W., "The Development of an Accelerated Testing Facility for the Study of Deposits in Land-Based Gas Turbine Engines," MS Thesis, Department of Mechanical Engineering, Brigham Young University (2004).

Jensen, J. W., J. P. Bons, S. W. Squire and T. H. Fletcher, "Simulated Land-Based Turbine Deposits Generated in an Accelerated Deposition," *Journal of Turbomachinery,* **v 12**(3), p 462-470 (2005).

Jia, R., B. Sunden, P. Miron and B. Leger, "A Numerical and Experimental Investigation of the Slot Film-Cooling Jet with Various Angles," *Journal of Turbomachinery,* **127**(3), 635-645 (2005).

Kallio, G. A. and M. W. Reeks, "A Numerical-Simulation of Particle Deposition in Turbulent Boundary-Layers " *International Journal of Multiphase Flow,* **15**(3), p433-446 (1989).

Kim, J., M. G. Dunn, A. J. Baran, D. P. Wade and E. L. Tremba, "Deposition of Volcanic Materials in the Hot Sections of Two Gas Turbine Engines," *Journal of Engineering for Gas Turbines and Power,* **115**(3), p641-651 (1993).

Krishnan, V., J. S. Kapat, Y. H. Sohn and V. H. Desai, "Effect of Film Cooling on Low Temperature Hot Corrosion in a Coal Fired Gas Turbine," IGTI, Atlanta, GA, United States, GT-2003-38693 (2003).

L.Baxter, L. and K.R.Hencken, "The Dynamic Variationof Particle Capture Efficiency During Ash Deposition in Coal-Fired Combustors," Twenty-Third Symposium(International) on Combustion/The Combustion Insitute (1990).

Leonard, B. P., "Ultra-Sharp Nonoscillatory Convection Schemes for High-Speed Steady Multidimensional Flow.," S. Mokhtari, NASA Lewis Research Center, NASA Lewis Research Center (1990).

Li, A. and G. Ahmadi, "Dispersion and Deposition of Spherical Particles from Point Sources in a Turbulent Channel Flow," *Aerosol Science and Technology,*(16), 209-226 (1992).

Lin, Y., B. Song, B. Li and G. Liu, "Measured Film Cooling Effectiveness of Three Multihole Patterns," *Journal of Heat Transfer,* **128**(2), 192-197 (2006).

Liu, B. and J. Agarwal, "Experimental Observation of Aerosol Deposition in Turbulent Flow," *Aerosol Science,* **v 5**, pp. 145 (1974).

Lu, H., "Experimental and Modeling Investigations of Biomass Particle Combustion”," PhD Dissertation, Chemical Engineering Department, Brigham Young University (2006).

Lu, Y., H. Nasir and S. V. Ekkad, "Film Cooling from a Row of Holes Embedded in Transverse Slots," IGTI, Reno-Tahoe, Nevada, USA, GT2005-68598 (2005).

Lu, Y., A. Dhungel, S. V. Ekkad and R. S. Bunker, "Film Cooling Measurements for Cratered Cylindrical Inclined Holes," IGTI, Montreal, Canada, GT 2007-27386 (2007a).

Lu, Y., A. Dhungel, S. V. Ekkad and R. S. Bunker, "Effect of Trench Width and Depth on Film Cooling from Cylindrical Holes Embedded in Trenches," IGTI, Montreal, Canada, GT2007-27388 (2007b).

Lu, Y. and R. S. Bunker, "Trench Film Cooling-Effect of Trench Downstream Edge and Hole Spacing," IGTI, Berlin, Germany, GT2008-50606 (2008).

Makki, Y. H. and G. S. Jakubowski, "Experimental Study of Film Cooling from Diffused Trapezoidal Shaped Holes," AIAA/ASME 4th Joint Thermophysics and Heat Transfer Conference**:** 10p (1986).

Mehendale, A. B. and J. C. Han, "Influence of High Mainstream Turbulence on Leading Edge Film Cooling Heat Transfer," International Gas Turbine and Aeroengine Congress and Exposition, Brussels, Belg, Publ by ASME, New York, NY, USA**:** 9-10 (1990).

Mulik, P. R., R. A. Wenglarz, C. J. Spengler and G. A. Whitlow, "Coal-Derived Liquid Fuel Performance under Gas Turbine Conditions " *Energy Progress,* **5**(3), p136-142 (1985).

Na, S., B. Williams, R. A. Dennis, K. M. Bryden and T. I. P. Shih, "Internal and Film Cooling of a Flat Plate with Conjugate Heat Transfer," IGTI, Montreal, Canada, GT2007-27599 (2007).

Ragland, K. W., M. K. Misra and D. J. Aerts, "Ash Deposition in a Wood-Fired Gas Turbine," *Journal of engineering for gas turbines and power,* **117**, p509 (1995).

Renze, P., W. Schroder and M. Meinke, "Large_Eddy Simulation of Film Cooling Flow Ejected in a Shallow Cavity," IGTI, Berlin, Germany, GT2008-50120 (2008).

Robinson, A. L., S. G. Buckley and L. L. Baxter, "Experimental Measurements of the Thermal Conductivity of Ash Deposits: Part 1. Measurement Technique," *Energy & Fuels,* **15**(1), 66(9) (2001).

Rutledge, J. L., D. Robertson and D. G. Bogard, "Degradation of Film Cooling Performance on a Turbine Vane Suction Side Due to Surface Roughness," IGTI, Reno-Tahoe, Nevada, USA, GT2005-69045 (2005).

Safman, P. G., "The Lift on a Small Sphere in a Slow Shear Flow," *J. Fluid Mech.,*(22), 385-400 (1965).

Saumweber, C., A. Schulz and S. Wittig, "Free-Stream Turbulence Effects on Film Cooling with Shaped Holes," IGTI, Amsterdam, Netherlands, GT-2002-30170 (2002).

Schmidt, D. and L. Bogard, "Effect of Free-Stream Turbulence and Surface Roughness on Film Cooling," IGTI, Birmingham, UK, 96-GT-462 (1996).

Schmidt, D. L., B. Sen and D. G. Bogard, "Film Cooling with Compound Angle Holes: Adiabatic Effectiveness," IGTI, Hague, Netherlands, 94-GT-312 (1994).

Schmidt, D. L., B. Sen and D. G. Bogard, "Effects of Surface Roughness on Film Cooling," IGTI, Birmingham, UK, 96-GT-299 (1996).

Schwarz, S. G., R. J. Goldstein and E. R. G. Eckert, "The Influence of Curvature on Film Cooling Performance," *Journal of Turbomachinery* **113**(3), p472-478 (1991).

Sen, B., D. L. Schmidt and D. G. Bogard, "Film Cooling with Compound Angle Holes: Heat Transfer," IGTI, Hague, Netherlands, 94-GT-312 (1994).

Silieti, M., A. J. Kassab and E. Divo, "Film Cooling Effectiveness from a Single Scaled-up Fan-Shaped Hole a Cfd Simulation of Adiabatic and Conjugate Heat Transfer Models," IGTI, Reno-Tahoe, NV, United States, GT2005-68431 (2005).

Soltani, M. and G. Ahmadi, "On Particle Adhesion and Removal Mechanisms in Turbulent Flows," *Adhesion Science Technology,* **8**(7), 763-785 (1994).

Somawardhana, R. P. and D. G. Bogard, "Effects of Obstructions and Surface Roughness on Film Cooling Effectiveness with and without a Transverse Trench," IGTI, Montreal, Canada, GT2007-28003 (2007).

Suao and Aoki, "Trend and Key Technologies for Gas Turbine Combined Cycle Power Generation in a Globally Competitive Market and Environmental Regulations," International Joint Power Generation Conference, Miami, Florida, USA (2000).

Sundaram, N. and K. A. Thole, "Effects of Surface Deposition, Hole Blockage, and Tbc Spallation on Vane Endwall Film-Cooling," IGTI, Barcelona, Spain, GT2006-90379 (2006).

Sundaram, N., M. D. Barringer and K. A. Thole, "Effects of Deposits on Film Cooling of a Vane Endwall Along the Pressure Side," IGTI, GT2007-27131 (2007).

Svensson, K. I., A. J. Mackrory and D. R. Tree, "Calibration of an RGB, CCD Camera and Interpretation of Its Two-Color Images for Kl and Temperature," SAE 2005 World Congress & Exhibition, **2005-01-0648** (2005).

Syverud, E., O. Brekke and L. E. Bakken, "Axial Compressor Deterioration Caused by Saltwater Ingestion," *Journal of Turbomachinery,* **v129**(1), p119-126 (2007).

Walters, D. K. and J. H. Leylek, "Systematic Computational Methodology Applied to a Three-Dimensional Film-Cooling Flowfield," IGTI, Birmingham, UK, ASME 96-GT-351 (1996).

Walters, D. K. and J. H. Leylek, "A Detailed Analysis of Film-Cooling Physics: Part I - Streamwise Injection with Cylindrical Holes," *Journal of Turbomachinery,* **v122**(1), p102-112 (2000).

Wammack, J. E., "Evolution of Turbine Blade Deposits in an Accelerated Deposition Facility:Roughness and Thermal Analysis " MS Thesis, Department of Mechanical Engineering, Brigham Young University (2005).

Wammack, J. E., J. Crosby, D. Fletcher and J. P. Bons, "Evolution of Surface Deposits on a High Pressure Turbine Blade, Part I," IGTI, Barcelona, Spain, GT2006-91246 (2006).

Waye, S. K. and D. G. Bogard, "High-Resolution Film Cooling Effectiveness Comparison of Axial and Compound Angle Holes on the Suction Side of a Turbine Vane," *Journal of Turbomachinery,* **129**(2), 202-211 (2007).

Wenglarz, R. A. and R. G. Fox, Jr., "Physical Aspects of Deposition from Coal-Water Fuels under Gas Turbine Conditions," *Journal of Engineering for Gas Turbines and Power,* **v112**(1), p9-14 (1990a).

Wenglarz, R. A. and R. G. J. Fox, "Chemical Aspects of Deposition/Corrosion from Coal Water Fuels under Gas Turbine Conditions," *Journal of Engineering for Gas Turbines and Power,* **112**(January), 1-8 (1990b).

Wenglarz, R. A., "An Approach for Evaluation of Gas-Turbine Deposition," *Journal of Engineering for Gas Turbines and Power,* **v114**(2), p230-234 (1992).

Wenglarz, R. A. and I. G. Wright, "Alternate Fuels for Land-Based Turbines," Materials and Practices to Improve Resistance to Fuel Derived Enviromental Damage in Land- and Sea-Based Turbines**:** 4-45-4-64 (2003).

Whitlow, G. A., S. Y. Lee, P. R. Mulik, R. A. Wenglarz, T. P. Sherlock and A. Cohn, "High-Temperature Combustion of Residual Fuel Oil-Some Deposition Product Considerations " Proceedings of the 2nd Conference on Advanced Materials for Alternative-Fuel-Capable Heat Engines., Monterey, CA, USA (1982).

Yuen, C. H. N. and R. F. Martinez-Botas, "Film Cooling Characteristics of Rows of Round Holes at Various Streamwise Angles in a Crossflow: Part I. Effectiveness," *International Journal of Heat and Mass Transfer,* **48**(23-24), 4995-5016 (2005).

Zhu, H., D. Xu, T. Guo and S. Liu, "Effects of Film Cooling Hole Shape on Heat Transfer," *Heat Transfer - Asian Research,* **v 33**(n 2), p 73-80 (2004).

Appendix A. Thermal Resistance Measurement and Analysis

The initial plan of this project was to test deposited coupons in BYU's thermal resistance measurement apparatus shown in Figure A.1. The goal was to assess degradation of the insulation provided by the TBC when deposits penetrated the surface. Thermal resistance measurements were attempted using a flat-flame burner to introduce a stable surface heat flux to the test coupon. The backside surface temperature was measured with an embedded thermocouple while the temperature of the deposit surface was measured with an infrared camera. A heat flux sensor sandwiched between the test coupon and a backside water coolant jet allowed the thermal resistance of the coupon to be estimated. Comparing this to a pre-test measurement should permit the assessment of the change in thermal resistance due to the deposition process. Repeated attempts to validate this test apparatus were inconclusive. Therefore, efforts were made to characterize each part of the experiment. The heat flux sensors were calibrated using an aluminum rod with embedded thermocouples in the axial direction, as shown in Figure A.2. This system was analyzed with the 1-D heat conduction equation:

$$q = -k \, \Delta T/\Delta x \tag{A.1}$$

where q is the heat flux (W/m2), k is the thermal conductivity (W/m-K), ΔT is the difference in temperature across the sample (K), and Δx is the distance (m). The concept was to measure the heat flux (q) and the temperature at each surface (giving ΔT), and the only unknown was the thermal conductivity (k). The experiments with an aluminum rod showed that the heat flux sensors were within 10-20% of the measured values, as shown in Figure A.3 for aluminum 6061.

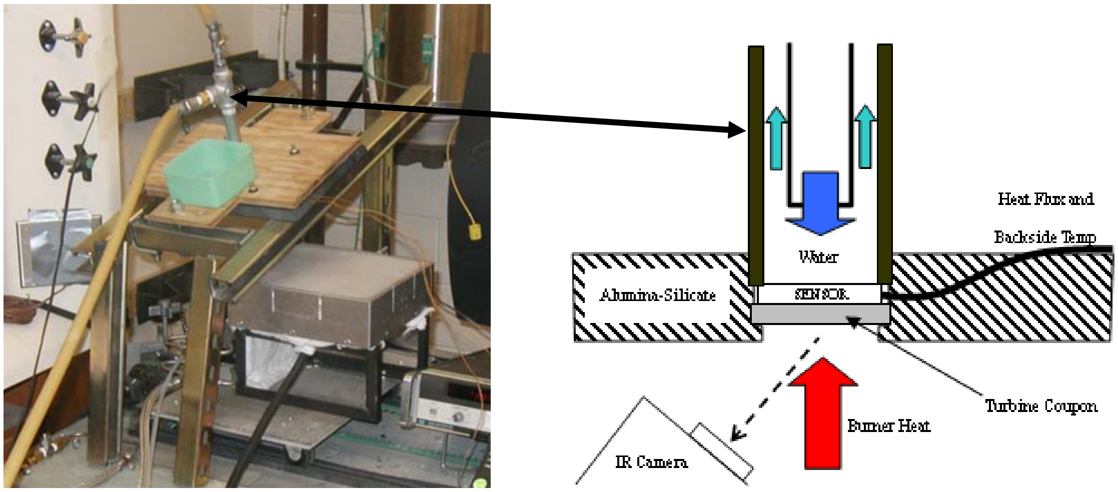

Figure A.1 Digital photograph and schematic of BYU's deposit thermal resistance measurement apparatus.

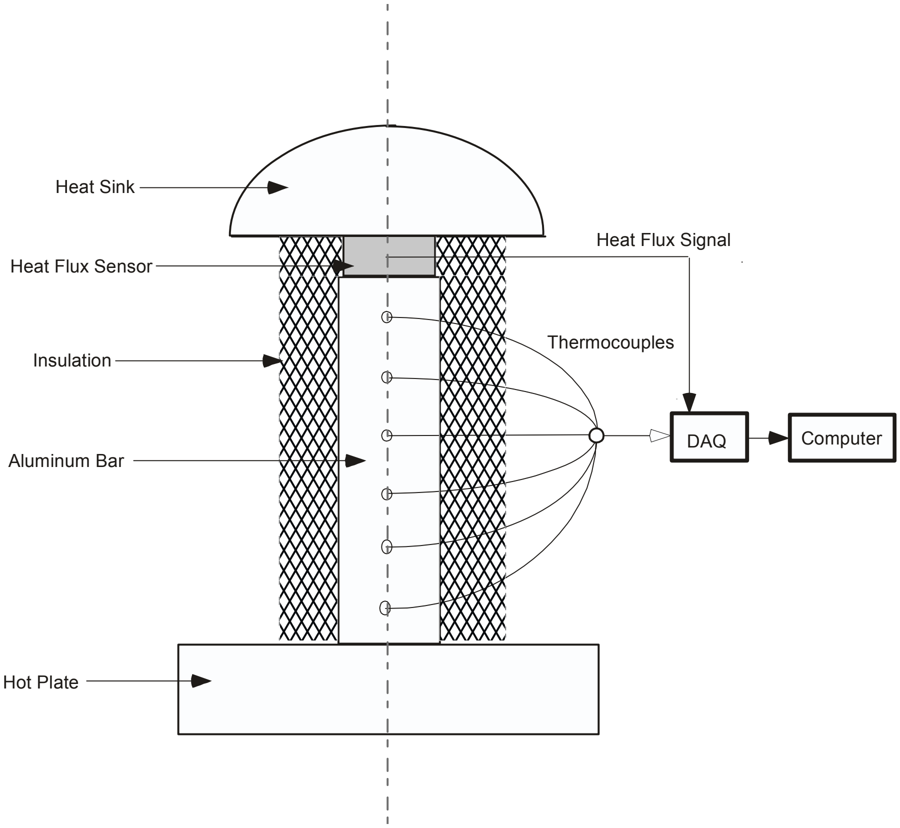

Figure A.2 Schematic calibration test for heat flux sensor using an aluminum 6061 rod embedded with thermocouples.

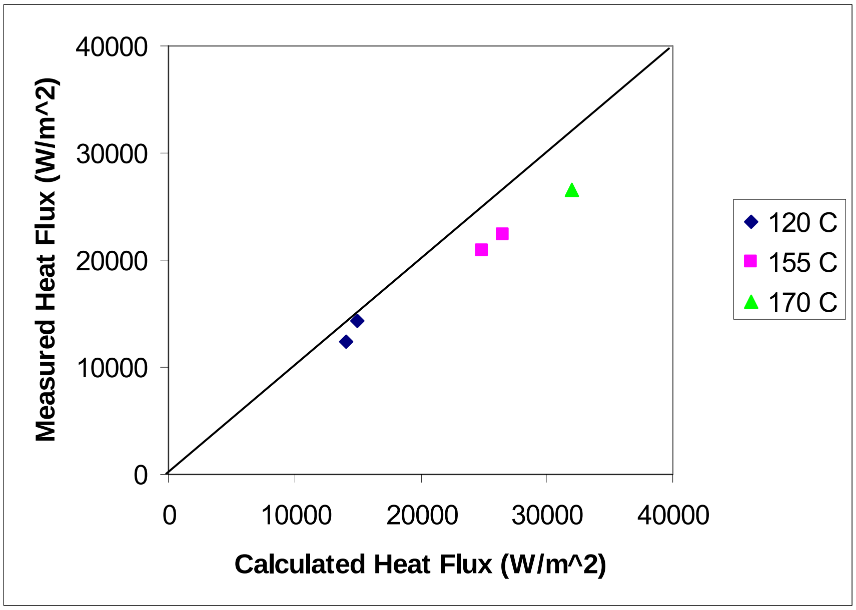

Figure A.3 **Calibration of heat flux sensor for aluminum 6061 rod embedded with thermocouples. The heat flux is measured with a heat flux sensor and calculated from the known thermal conductivity and measured temperature on each surface.**

A hot plate system was then used to see if this technique would work for a coupon in the shape of a disk. Thermocouples were used to measure the front and back surfaces of the coupon, and thermal paste was used in the interface between the heat flux sensor and the coupon to maximize thermal contact. An aluminum coupon was used in these experiments, as shown schematically in Figure A.4. An aluminum cylinder was placed on top of the heat flux sensor to act as a heat sink. These experiments did not yield satisfactory results; the heat flux measured by the sensor was about an order of magnitude different than the heat flux calculated from the temperature difference and thermal conductivity. The reason for this discrepancy is thought to be due to the low value of the temperatures and temperature differences in this experiment. Small inaccuracies in the measured temperatures led to large changes in the heat flux calculations in this low temperature system. In particular, the thermocouple located between the hot plate and the aluminum coupon did not seem to be accurate due to poor contact.

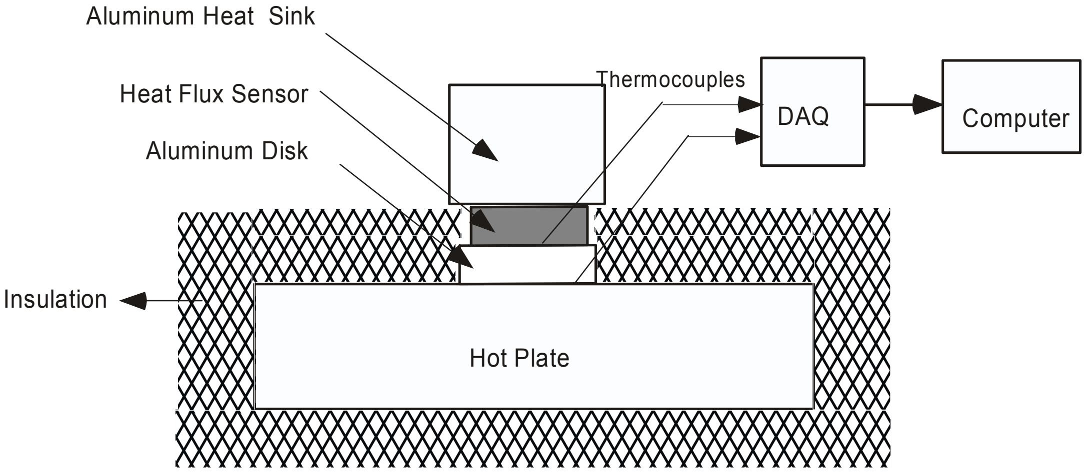

Figure A.4 **Schematic of apparatus to use hot plate to determine heat flux for a metal coupon.**

A second hot plate experiment was performed with the configuration shown in Figure A.5. An IR camera was used to measure the surface temperature of a stainless steel coupon that was situated on top of the heat flux sensor mounted on the hot plate. The emissivity of the stainless steel was set at 0.95 for the IR temperature measurement. At hot plate temperatures between 110 and 120°C, the thermal conductivity measured in this manner was only about 2.5 W/ (m^2.°C) instead of the known value of 15-16 W/ (m^2.°C), indicating that this technique was not successful. The failure again seemed to be due to the inaccurate temperature measurement.

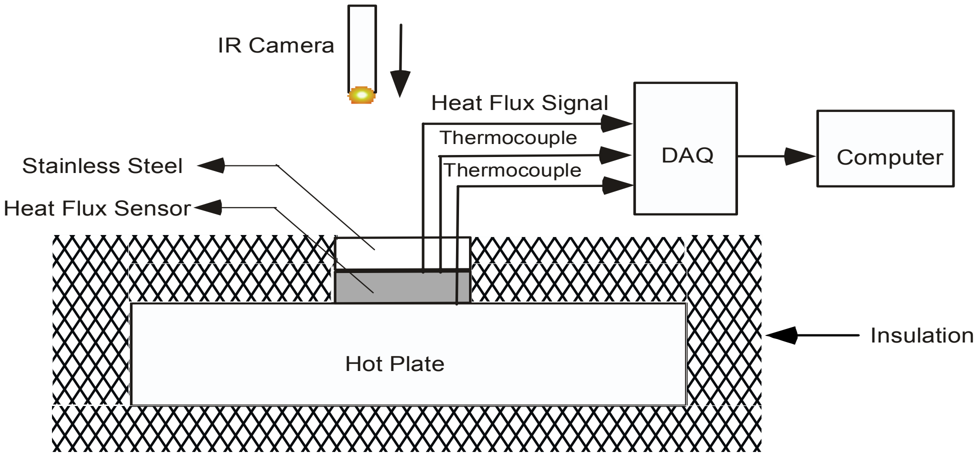

Figure A.5 Schematic of apparatus to use hot plate to determine heat flux for a metal coupon using an IR camera to measure the surface temperature.

Since the heat flux sensors seemed to be working, a system was developed to measure the thermal conductivity in a higher temperature environment; this was thought to minimize the effect of small errors in temperature measurement. The flat-flame burner was used to heat an aluminum disk, as shown in Figure A.6. An IR camera was used to measure the surface temperature of the coupon that faces the flame. The aluminum coupon was encased in a ceramic (aluminosilicate) plate, which provided insulation in the transverse direction. A ceramic plug was placed on the backside of the aluminum coupon for insulation as well. This test was run until a steady-state temperature was achieved. The IR camera used requires an emissivity of the surface. Figure A.7 shows values of the IR temperature measurement using two different values of the emissivity. The value of $\varepsilon = 0.29$ gave results that were physically realistic, i.e., the front surface temperature should always be hotter than the back surface temperature. A correlation of the measured front surface temperature (using the IR camera) and the backside temperature (using the thermocouple) is shown in Figure A.8. It is possible that this type of correlation could be useful in the particle deposition experiments, but another method was sought that could measure the actual changes in thermal conductivity as deposits grow on a coupon.

Finally, the IR camera was used to measure the surface temperature of an aluminum coupon suspended over the flat-flame burner. The heat flux sensor was attached to the back side of the coupon, as shown in Figure A.9. Experiments in this system were conducted with (a) insulation in back of the heat flux sensor, (b) stagnant air in back of the sensor, and (c) flowing water in back of the sensor. Unfortunately, in spite of best efforts, the thermal conductivities measured in this system were more than an order of magnitude lower than reported in the literature.

The results of this series of experiments to measure the thermal conductivity of a metal coupon using the IR camera with heat flux sensors and/or thermocouples have been very discouraging. This effort was discontinued.

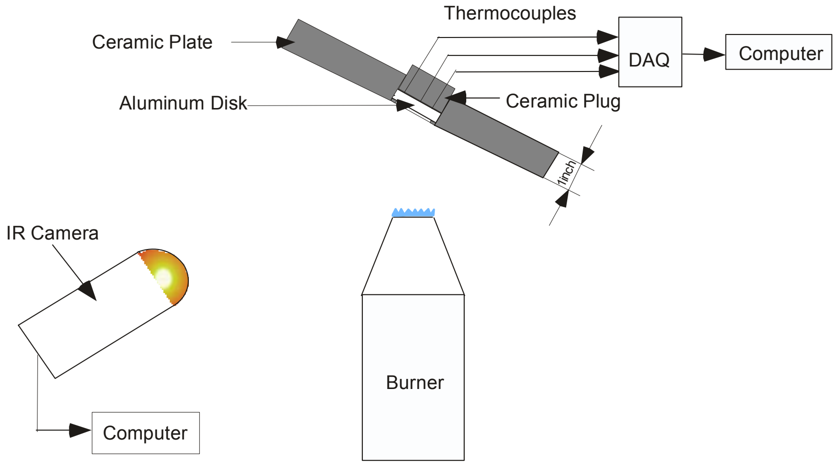

Figure A.6 Schematic of apparatus to heat up the aluminum coupon inside the alumina silicate with burner to determine the correlation between the temperature measured by IR camera and temperature measured by thermocouples.

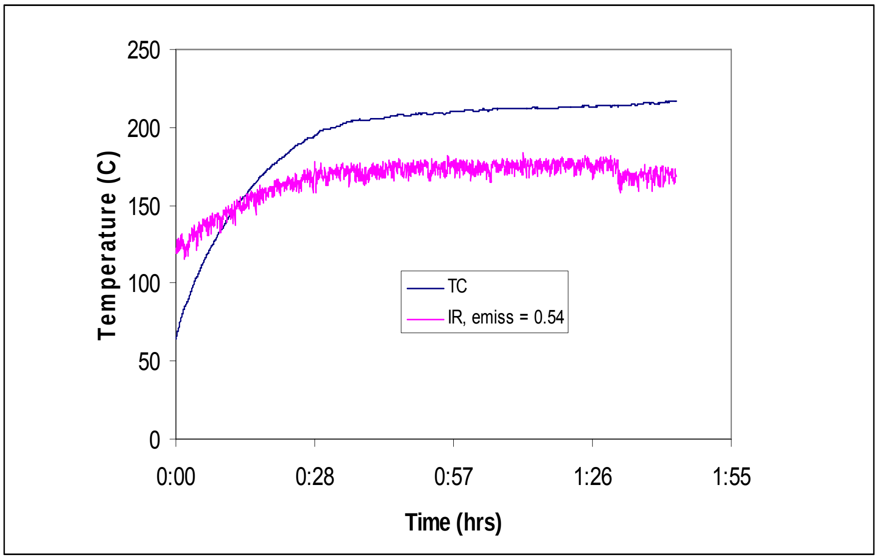

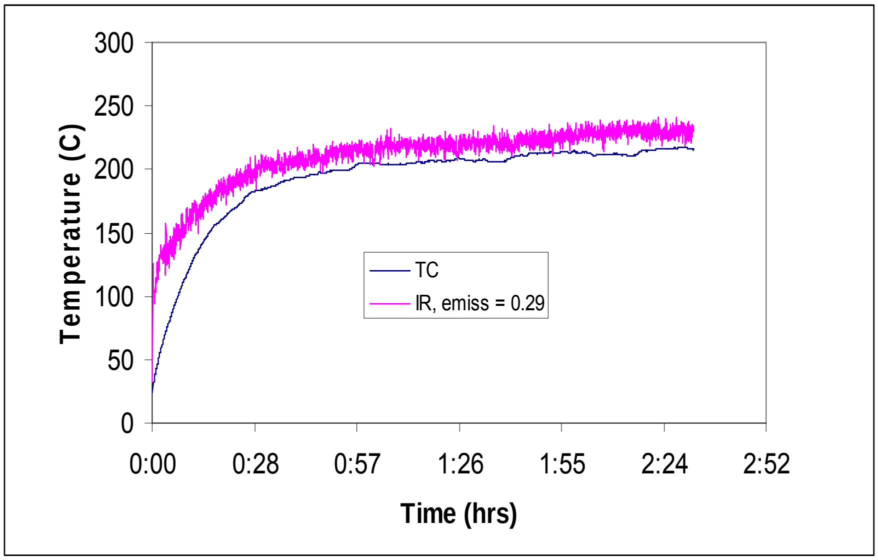

Figure A.7 Results of transient experiments using different values of ε.

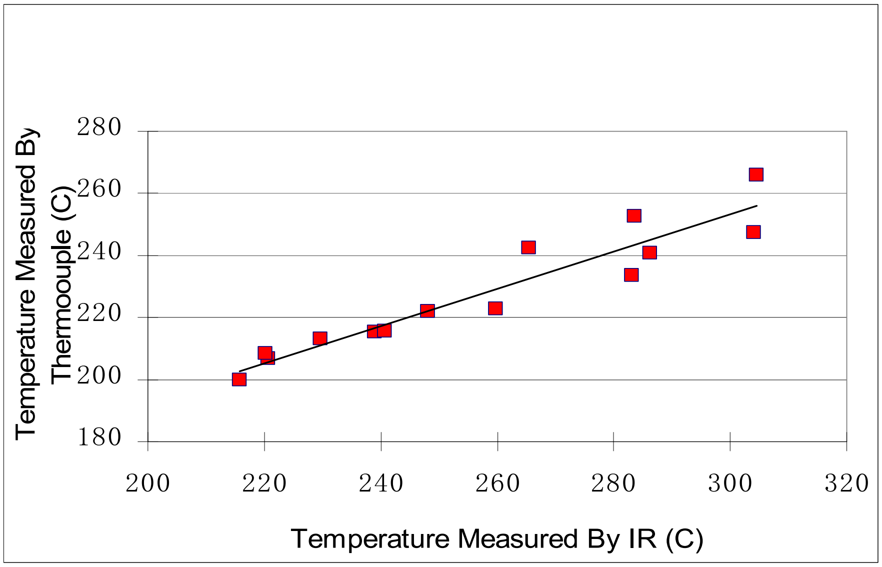

Figure A.8 Schematic of correlation between the temperature measured by IR camera and the temperature measured by thermocouple

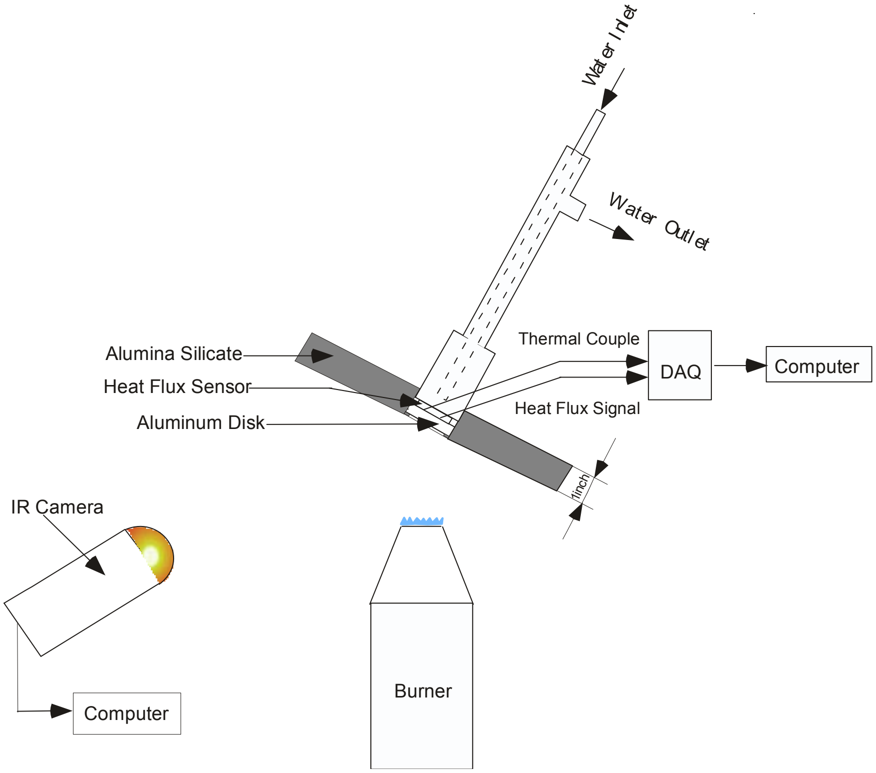

Figure A.9 Schematic of flat-flame burner system, with backside cooling, to measure thermal conductivities of an aluminum coupon.

It is recommended that a technique be used to determine temperatures optically that is independent of emissivity. Perhaps a 2-color pyrometry technique could be used using the RGB system described in this dissertation. This idea was strongly considered while the original coupon was in the accelerated deposition facility (i.e., *in situ*) by cutting a whole through the radiation shield for optical access. If the surface temperature is measured optically on one side and with thermocouples welded to the back side, the temperature difference across the coupon is known.